



Max-Planck-Institut für Metallforschung
Stuttgart

**Microstructural Characterization of Yttria-
Stabilized Zirconia Thermal Barrier Coatings
Grown on Sapphire Substrates**

Boryana Rashkova

Dissertation
an der
Universität Stuttgart

Bericht Nr. 145
November 2003

Microstructural Characterization of Yttria-Stabilized Zirconia Thermal Barrier Coatings Grown on Sapphire Substrates

Vor der Fakultät Chemie der Universität Stuttgart
zur Erlangung der Würde eines

Doktors der Naturwissenschaften (Dr. rer. nat.)

genehmigte Abhandlung

vorgelegt von Dipl.-Ing.

BORYANA RASHKOVA

aus Sofia / Bulgarien

Hauptberichter: Prof. Dr. M. Rühle

Mitberichter: Prof. Dr. F. Aldinger

Tag der Prüfung: 15.12.2003

MAX-PLANCK-INSTITUT FÜR METALLFORSCHUNG STUTT GART

2003

На Моите Родители

Table of Contents

Abstract	1
Zusammenfassung	3
Chapter 1: Introduction	6
1.1. The TBC System	6
1.2. Purpose of the Thesis	9
1.3. Organization of the Thesis	10
Chapter 2: Background	12
2.1. Crystal structure of YSZ and Alumina	12
2.1.1 Zirconia and Yttria–Stabilized Zirconia	12
2.1.2 α -Alumina	14
2.2. Thermodynamics of the ZrO_2 - Y_2O_3 System	16
2.3. Microstructure of YSZ grown by EB-PVD	18
2.3.1 Columnar growth	19
2.3.2 Crystallographic texture	21
2.2.3 Microstructure of the interface	24
2.4. Microstructure of YSZ grown by precursor methods	25
2.4.1 YSZ Growth on Sapphire Substrates	25
2.4.2 YSZ Growth on Single Crystal ZrO_2	29
Chapter 3: Processing of the model systems and samples preparation	30
3.1 Precursor derived islands	30
3.2. EB-PVD	30
3.3. Sample preparation	33
3.3.1 Metallographic Preparation	33
3.3.2 TEM Preparation	34
Chapter 4: Experimental methods	36
4.1. Conventional TEM	37
4.2. High resolution TEM	40
4.3. Analytical TEM	41

Chapter 5: Results	44
5.1. YSZ Deposited by EB-PVD on Stationary Sapphire Substrates	44
5.2. YSZ Deposited by EB-PVD on Rotated Sapphire Substrates	48
5.3. YSZ Deposited on Sapphire Substrates by Precursor Method	53
5.4. YSZ Deposited by EB-PVD on Rotated Seeded-Sapphire Substrates	54
Chapter 6: Discussion	94
6.1. Morphology and texture	94
6.2. Orientation relationship at the interface	96
6.3. Interface microstructure	101
6.4. YSZ growth on seeding layers	102
Chapter 7: Conclusion	114
References	116
Acknowledgements	124
Curriculum vitae	126

List of Abbreviations

AEM	= Analytical Electron Microscopy
AFM	= Atomic Force Microscopy
BC	= Bond Coat
BF	= Bright Field
CBED	= Convergent Beam Electron Diffraction
CTEM	= Conventional Transmission Electron Microscopy
DF	= Dark Field
DP	= Diffraction Pattern
EB-PVD	= Electron Beam Physical Vapor Deposition
EDXS	= Energy Dispersive X-Ray Spectroscopy
EELS	= Electron-Energy-Loss Spectroscopy
HRTEM	= High Resolution Transmission Electron Microscopy
SAD	= Selected Area Diffraction
SEM	= Scanning Electron Microscopy
STEM	= Scanning Transmission Electron Microscope
TEM	= Transmission Electron Microscopy
TBC	= Thermal Barrier Coating
TGO	= Thermally Grown Oxide
XRD	= X-Ray Diffraction
YSZ	= Yttria Stabilized Zirconia

Abstract

The present work systematically addresses, for the first time, the characterization of interfaces between thermal barrier coatings (TBCs) and the underlying thermally grown aluminum oxide (TGO) using a model system comprising yttria-stabilized zirconia (YSZ) deposited by electron-beam physical vapor deposition (EB-PVD) on basal plane sapphire. The results provide new insight into the initial stages of TBC growth and especially on the development of texture and the influence of crystallographic orientation relationships at the YSZ/sapphire interface.

The YSZ films investigated were deposited at moderate-to-low rates on stationary and rotated substrates, to assess the effects of changing the vapor incidence pattern on the microstructures of interface and coating. A second model system comprising YSZ *seeds* prepared by solution precursor methods on similar sapphire substrates was used to investigate the potential for modifying texture and column microstructure by *templating* the growth. The texture and the morphology of the coating were characterized by X-ray diffraction (XRD) and Scanning Electron Microscopy (SEM). Extensive analysis by Transmission Electron Microscopy (TEM) was undertaken to investigate the microstructure as well as the orientation relationships between film and substrate directly at the interface. High-Resolution TEM (HRTEM) allowed examination of the atomic arrangements and defects at the interface.

TBCs deposited on stationary substrates resulted in a dense columnar microstructure with a roof-top morphology and strong $\langle 100 \rangle$ out-of-plane fiber texture. This is at variance with YSZ films grown under similar (stationary) conditions on polycrystalline alumina thermally grown on bond-coat alloys. It was shown that the $\langle 100 \rangle$ texture is templated by the substrate and, because most grains are equally competitive, gives rise to columns with persistent small diameters. Moreover, although the substrate promotes a strong out-of-plane epitaxy, it is rather non-selective with respect to the in-plane orientation, resulting in the observed fiber texture. A periodic variation in the vapor incidence pattern upon rotation yields a less dense, porous microstructure with a larger column diameter than those coatings on stationary substrates. Moreover, in addition to the $\langle 100 \rangle$ out-of-plane texture the coatings also exhibit a preferred in-plane orientation with the other $\langle 100 \rangle$ axes in-plane, parallel and perpendicular to the rotation axis. Porosity, morphology and texture are strongly correlated to the geometrical effect of rotation. TEM revealed again a common out-of-plane axis in the grains near the interface with multiple in-plane orientations but much less random than on the stationary substrates. Near the interface 83% of the grains exhibit one of the three possible

variants of the $[10\bar{1}0]_s \parallel [001]_{\text{YSZ}}$ orientation relationship, each rotated 120° from one another around the $[001]_{\text{YSZ}}$ axis. The other 17% of the grains have intermediate orientations between these variants.

The above coatings represent special cases of the mechanism of evolutionary selection, in which columns do not evolve from a spatially random array of nuclei on the substrate, but rather from an initial population with a strong out-of-plane orientation. In the absence of rotation most of the grains are equally competitive and, after a short initial period where stray grains are eliminated, most of the columns propagate with little variation in the diameter and crystallographic orientation. Upon rotation, only the orientation that allows all facets of the column tip to receive equal amount of flux may survive the evolutionary selection mechanism. Hence, a much smaller fraction of columns is selected, and their diameter increases until a steady state condition corresponding to the bi-axially textured film is developed. Because growth under rotation occurs at a slower rate, the grain structure at the interface also evolves during deposition, promoting those orientations that reduce the interfacial energy with the substrate. This results in the development of preferred interfacial variants *after the nucleation stage*, with a mechanism largely independent from the evolutionary selection process occurring at the growth front. The HRTEM investigations confirm the origin of the epitaxy right at the interface and also the absence of any inter-phases.

TBCs deposited on seeded, rotating sapphire substrates show textures much less developed with some influence of the orientation of the seeds but with no evidence of epitaxial growth of the vapor deposited material on the seeds. The results reveal that the surface roughening resulting from the incorporation of seeds has a strong effect in delaying the evolution of the texture in spite of the presence of “favorable” sites. The texture in this case evolves in the more conventional manner, with rotation playing a predominant role over surface templating effects.

Zusammenfassung

Die vorliegende Arbeit charakterisierte erstmals systematisch die Mikrostruktur an der Grenzfläche zwischen Wärmedämmschichten (*Thermal Barrier Coatings TBC*) und dem darunter thermisch aufwachsenden Aluminiumoxid (*Thermally Growth Oxyde TGO*) am Bsp. des Modellsystems Yttria-stabilisiertes Zirkoniumoxid (YSZ) abgeschieden durch Elektronenstrahlverdampfen (*Electron Beam Physical Vapor Deposition EB-PVD*) auf der Basalebene (0001) von Saphireinkristallen. Die Ergebnisse bieten einen neuen Einblick in das Anfangsstadium des TBC-Wachstums, insbesondere der Texturentwicklung und des Einflusses der kristallographischen Orientierungsbeziehung an der YSZ/Saphir-Grenzfläche.

Die untersuchten YSZ-Filme wurden bei moderaten bis niedrigen Raten auf stationären und rotierenden Substraten abgeschieden, um in Abhängigkeit des Materialflusses die Mikrostruktur der Grenzfläche an der Beschichtung zu studieren. Ein zweites Modellsystem, wofür sich auf dem Substrat YSZ-Keime befinden (hergestellt durch Precursor-Methoden auf Saphireinkristallen), erlaubt durch das Wachstum in Zeitschritten die Untersuchung der Veränderung der Textur und der Säulenmikrostruktur.

Die Charakterisierung der Textur und der Morphologie erfolgte durch Röntgendiffraktometrie (XRD) und Rasterelektronenmikroskopie (SEM). Im Transmissionselektronenmikroskop (TEM) erfolgten ausführliche Untersuchungen, um die Mikrostruktur sowie die Orientierungsbeziehung zwischen Film und Substrat direkt an der Grenzfläche zu untersuchen. Hochauflösende TEM (HRTEM) gestattet die Untersuchung der atomaren Struktur und der Defekte an der Grenzfläche.

TBC, abgeschieden auf stationären Substraten, zeigten eine dichte, säulenartige Mikrostruktur mit einer dachförmigen Morphologie und ausgeprägter $\langle 100 \rangle$ Fasertextur. Dies widerspricht Ergebnissen zu YSZ-Filmen, die unter vergleichbaren (stationären) Bedingungen auf polykristallinen Aluminiumoxid von *Bond Coat* Legierungen thermisch gewachsen sind. Es wurde gezeigt, dass die $\langle 100 \rangle$ Fasertextur durch die Kristalloberfläche der Substratoberfläche bedingt ist, weil die meisten Körner vergleichbar konkurrierend sind. Die Säulen des TBC wachsen mit einem gleichmäßigen schmalen Durchmesser auf. Außerdem fördert das Substrat ein ausgeprägtes out-of-plane Kristallwachstum, d.h. es ist nicht selektiv im Vergleich zur in-plane Orientierung, woraus die beobachtete Fasertextur resultiert.

Eine periodische Veränderung im Materialfluss während der Rotation führt zu einer weniger dichten, porösen Mikrostruktur mit großen Durchmessern der Säulen des TBC, verglichen zu dem unter stationären Bedingungen beschichteten Substraten. Außerdem zeigte das TBC

zusätzlich zu der beobachteten $\langle 100 \rangle$ out-of-plane Fasertextur eine parallel und rechtwinklig zur Rotationsachse bevorzugte in-plane Kristallorientierung mit einer $\langle 100 \rangle$ -Achse in der Kristallebene. Porosität, Morphologie und Textur sind stark von der Rotationsgeometrie während des Elektronenstrahlverdampfens abhängig. TEM bestätigte nochmals die out-of-plane-Achse in den zur Grenzfläche benachbarten Körnern, wobei mehrere in-plane Kristallorientierungen mit einer geringen Anzahl als bei den stationären Substraten statistisch verteilt sind. An der Grenzfläche weisen 83% der Körner eine der drei möglichen Varianten der $[10\bar{1}0]_s || [001]_{YSZ}$ auf, jede gegenüber der anderen um 120° um die $[001]_{YSZ}$ Kristallorientierung gedreht. Der verbleibende Anteil der Körner von 17% hatte zwischen diesen Varianten liegende Kristallorientierungen.

Das zuvor beschriebene TBC stellt einen speziellen Fall der Auswahl des Wachstumsmechanismus dar, in welchen die Säulen des TBC nicht ausgehend von einer statistischen Verteilung der Kristallorientierung der Keime auf dem Substrat aufwachsen, sondern von einer anfänglichen Verteilung mit einer ausgeprägten out-of-plane Kristallorientierung. Durch die Rotationsgeometrie sind die meisten Körner im Wachstumsmechanismus miteinander konkurrierend, wobei nach einer kurzen Anfangsperiode in der abweichende Körner ausscheiden, sich Säulen des TBC mit einer geringen Variation des Durchmessers und der kristallographischen Orientierung sich ausbilden. Während des Rotierens verbleibt der Wachstumsmechanismus, wo die Kristallorientierung aller Facetten an der Säulenspitze des TBC unter einen gleichmäßigen Materialfluss wächst. Deshalb wird nur ein geringerer Anteil der Säulen ausgewählt, und der Durchmesser steigt bis ein Gleichgewichtszustand an. Der Gleichgewichtszustand entspricht dem entwickelten zwei-axialen texturierten YSZ-Film. Da während der Rotation die Materialflussrate gering ist, veränderte sich während des Abscheidens die Kornstruktur an der Grenzfläche, wobei Kristallorientierungen die zur Reduktion der Oberflächenenergie mit dem Substrat führen bevorzugt werden. Diese Ergebnisse zum bevorzugten Wachstum an ausgewählten Kristallorientierungen nach der Keimbildungsphase, mit einem Mechanismus weitgehend unabhängig von der Wachstumsauswahl finden an der wachsenden YSZ Oberfläche statt. HRTEM Untersuchungen bestätigten das anfängliche epitaktische Wachstum an der Grenzfläche und das nicht vorhanden sein einer weiteren Grenzflächenphase.

TBC, das auf rotierenden, zuvor mit aufgewachsene Keimen Saphir-Einkristallen abgeschieden wurde, zeigte eine weit geringere Texturierung, wie es die Verteilung der Kristallorientierung der Keime vermuten lässt. Die Ergebnisse zeigten, dass die aus Aufbringen der Keime folgende Oberflächenrauigkeit eine Texturentwicklung an den

bevorzugten Kristallorientierungen stark verzögert. Die Texturierung geschah in diesem Fall auf einen mehr konventionellen Weg, wo die aus der Rotationsgeometrie folgende Oberflächenabschirmung einen wichtigen Einfluss hatte.

1. Introduction

1.1 The Thermal Barrier Coating System

Insulating ceramic coatings known as Thermal Barrier Coatings (TBCs) have been developed for use on turbine engine components in order to increase the operation temperature and efficiency of the engine. The use of TBCs can increase the turbine airfoil temperature by about 100°C which is equal to a 3-to-4 time increase of service life [96Jon, 97TKZ, and 01PLS]. The coating, combined with backside air-cooling of airfoils, protect the metallic “hot-section” components of turbine in aircraft gas engines from oxidation and creep damage, thereby improving the durability of the components.

A typical TBC system, shown schematically in Figure 1, consists of a substrate (e.g. nickel-based superalloy), an alumina forming bond coat (e.g. MCrAlY, where M = Ni, Co) and the thermally insulation, top coat, typically made of yttria-stabilized zirconia (YSZ).

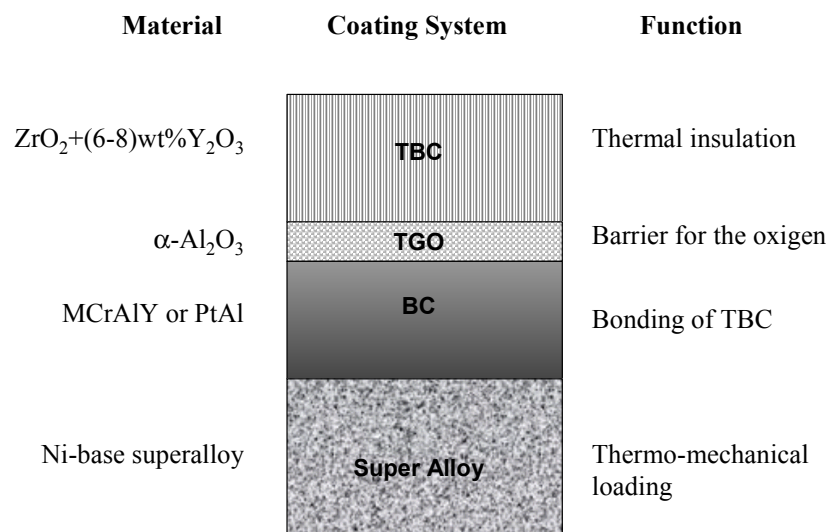


Fig. 1.1 Schematic cross-section of a typical TBC System: material selection and function

Each of these layers perform different task. The hot-section component is typically a Ni-based single crystal super alloy whose chemistry and microstructure has been optimized for high temperature creep resistance. The role of the bond coat, 100±50µm thick, is to provide additional corrosion and oxidation protection to the bulk component. The bond coat alloy is

designed similar to that of the super alloy but has a greater content of aluminum. The bond coat is essentially a reservoir of Al to support the formation of thermally grown oxide (TGO) at the TBC/BC interface. Because the top coat can not inhibit the oxygen transport through the layer, the TGO, primary $\alpha\text{-Al}_2\text{O}_3$, acts as a diffusion barrier for oxygen. This oxide is self passivating, and once formed it provides the required protection to the metallic substrate from the high-temperature oxidation. The preferred oxide is $\alpha\text{-Al}_2\text{O}_3$ because of its thermodynamically stability, low oxygen diffusivity, and superior adherence. It is important that metastable modifications of Al_2O_3 are not formed since they are not effective oxygen diffusion barriers.

The primary function of the ceramic top coat (referred to simply as a TBC) is to act as a thermal insulator and to reduce the heat transfer to the metallic substrate. The thermal barrier top coat, $100\pm 150\mu\text{m}$ thick, must satisfy the following two most important requirements: low thermal conductivity and a high coefficient of thermal expansion. This allows the coating to support a high level of insulation under a low level of thermal mismatch stress produced during coating and service thermal cycling. These requirements/criteria have been met by zirconia (ZrO_2), partially or completely stabilized with proper additions of Y_2O_3 , MgO or CaO . Ytria-stabilized zirconia, containing 6-8wt% Y_2O_3 , has been found empirically to be most spall resistant composition in thermal cycling conditions and therefore is commonly used as the thermal insulation layer in present TBC systems [89Mev, 96Jon, and 96LSB].

Presently, two main processes exist for making TBC. Those techniques are plasma spraying (PS) and electron beam physical vapor deposition (EB-PVD), respectively. Each method produces its own largely distinctive microstructure in the resultant TBC. Standard PS coatings possess a laminar structure with characteristic defects such as pores, cracks and separations at splat boundaries. The splat boundaries are preferably orientated parallel to the substrate surface. This microstructure represented an effective obstacle for thermal flux and possesses a very low thermal conductivity (0.8-1.1 W/mK) [01HLC]. The PS coatings are widely applied primarily for land-based engines. The bonding mechanism of these coatings is largely mechanical. Conversely, EB-PVD ceramic coating possesses a columnar structure, voids, and particular interspaces which are perpendicularly aligned to the substrate surface, therefore less effective in hindering thermal heat transfer (1.5-1.9 W/mK) [01HLC]. Apart from that, the EB-PVD technology leads to microstructure in which the grains are strongly (chemically) bonded to the underlying component surface. The segmented structure prevents the build-up of any residual stress and accommodates the thermal expansion mismatch strains with the underlying metallic component as the system is cycled between ambient temperature and the

operating temperature ($\sim 1100^{\circ}\text{C}$). In addition to excellent strain tolerance, the EB-PVD technology leads to aerodynamically smooth surfaces of the turbine blades, thus eliminating the need for final polishing or conditioning of the cooling holes [99BML, 01PLS, and 02NLJ]. Currently, the effectiveness of the TBC systems is limited by their mechanical reliability, and microstructural changes under the thermal cycling conditions. The major problem with TBCs is essentially the risk of poor adhesion of the coating on the component. The spallation of the TGO, upon reaching a critical thickness, has been considered as the most critical factor that limits the performance of the TBCs. The crack propagation is generally driven by the release of the residual stresses arises primarily from the thermal expansion mismatch between the ceramic and the metal, and oxide growth stresses [84Mil, 94LES, 94SBS, 96LSB, 97FSL, 01EMH, and 01PLS]. Additional factors, including the composition of both the alloy substrate and the BC, may affect the instability at the TGO/BC interface. Three areas of focus in the formation of an “ideal”, adherent oxide scale encompass: migration of Al and other elements in the metal substrate; segregation of elements to the metal-oxide scale interface and the grain boundaries [97PWL]. Failure of a TBC system may also occur within the thermal barrier itself. The mechanisms of primary concern are near-interface separation, phase transformation, sintering, hot corrosion, erosion and damage from foreign objects.

In both PS and EB-PVD systems, TBC adhesion and durability depends upon the characteristics of the interface to which they are bound. Therefore the TGO/BC roughening can also induce failure within the TBC itself. The response of the TBC to the evolution of undulations in the underlying TGO/BC depends on resilience of the TBC and the strength of the TGO/TBC interface. If the TBC is stiff and the interface weak, the geometric incompatibility of the flat TBC and undulated TGO produce separations in the TGO/TBC interface. If the interface is strong and TBC compliant, the interface remains intact and separation occurs within the TBC itself near the interface [01ToC]. It is unclear how these separations occur, but the microstructure of the near-interface will play a critical role in this mode of failure.

Despite of intensive research in this field, little attention has so far been paid to the microstructure of the TGO/TBC interface, especially characterized by TEM. There are only a few references [94UMH, 97FSL, and 00ScS] available concerning the microstructure of the near-interface TGO/TBC region. The authors observed the formation of a mix zone containing grains from $\alpha\text{-Al}_2\text{O}_3$ and YSZ. However, the mechanisms which lead to the formation of this mix zone and its influence on the adhesion and durability of the components is not complete understood.

On the other hand, the *Lang et al.* [90LML, 94CaL] show that $ZrO_2-Al_2O_3$ system displays non reactive interactions and the physical bonding at the interface is related to crystallographic features.

As the microstructure of the top coat influences the TBC performance, the questions naturally arises is whether the microstructure is affected by the type and crystallographic nature of the oxide on which the YSZ coating is deposited.

1.2 Purpose of the Thesis

Since the properties of the interface particularly the adhesion between the BC and TBC itself are critical for the spallation of TBC, a basic understanding of interface properties requires knowledge of the interface microstructure

It is proposed that fundamental study of the interface microstructure between sapphire and YSZ deposited by EB-PVD which is a model for the BC/TBC interface when the BC is oxidized is need to improve the TBC performance and durability.

The goal of this thesis is to provide a new insight into interface microstructure and characterization of the initial layer of YSZ growth by EB-PVD. It is focused on the morphology, texture development and crystallographic orientation relationship at the interface between substrate and deposited film. The investigated of these issues, interface microstructure need to be studied also at the atomic level.

The advantages of liquid precursor method like composition control and uniformity of the composition may use for producing preferably oriented grains, which can effectively seed the oriented growth of thicker films. The aim is to use the precursor thin film as templates to produce highly textured and well oriented EB-PVD deposited YSZ films.

In order to study the effect of processing parameters like rotation of the substrates (periodically changing the material flux) or influence different substrates like bare sapphire/seeded sapphire, on the interface microstructure and columnar growth, a model system were created at the UCSB Materials Department in the group of Prof. C. Levi. Model systems consist of single crystal sapphire, which is α -alumina (TGO) in conventional TBC systems and YSZ TBC deposited by EB-PVD. This makes possible the study of interface microstructure without the influence of oxidation of the BC and growth of TGO, as well as phase transformation in TGO and segregation of impurity.

To investigate the effect of controlled grain orientation on YSZ TBC growth, model system with sapphire and spin-coated YSZ precursor were prepared. The precursor YSZ grains were evolved by proper annealing treatments, and then, on the top, coated with YSZ TBC.

The goals have been achieved through systematic investigations of the microstructure of YSZ grown under different growth conditions. The microstructure has been investigated in details by TEM technique which enables the study of interface down to the atomic level.

1.3 Organization of the Thesis

Chapter 1 gives a general introduction to the thesis and details of the TBC system. Chapter 2 summarizes the crystal structures and main physical properties for the materials in the model systems, and thermodynamics of the ZrO_2 - Y_2O_3 system and it is based on the existing literature on the subject. The information in this chapter provides a background to the current knowledge of the microstructure of YSZ TBCs by EB-PVD concerning columnar growth, crystallographic texture and porosity. A brief review is given of the microstructure development of YSZ grown on different substrates, and under different processing conditions. This background is focused on the interface microstructure between YSZ and sapphire and the influence of the deposition methods on it.

Chapter 3 deals with the processing of the model systems that are studied in the present work. It is based on the growth of TBCs using a dedicated EB-PVD coater at UCSB. This chapter also outlines the sample preparation techniques, a key issue for microscopy studies carried out. In Chapter 4, introduces the basic principles of the techniques such as conventional and high resolution transmission electron microscopy, which are required for microstructural characterization.

The experimental results of the systematic investigation from the current research are summarized in Chapter 5. This chapter addresses the characterization of the morphology, crystallographic texture and orientation relationship in interfacial region between film and substrate. The studies were carried out for the YSZ TBC deposited on stationary and rotated sapphire substrates. The results are compared with the YSZ TBC deposited on seeded sapphire substrates under rotation conditions.

Chapter 6 deals with the discussion of the results, and presents conclusions made from the experimental observations. Primarily, it correlates the morphology of the growth top surface to the texture type of the YSZ film. It is focused on the development of the interface microstructure and especially on the orientation relationship between film and substrate. The

discussion links the observed results for YSZ deposited on stationary and on the rotated substrates to the influence of the sapphire substrates and the effect of the rotation.

2. Background

The background information provided in this chapter begins with an introduction of the characteristic of the materials that form the YSZ/sapphire interface investigated in the present thesis, with emphasis on their crystal structure. The current knowledge of the microstructure of YSZ TBCs grown by EB-PVD concerning columnar growth, crystallographic texture and the microstructure of the interface are reviewed. It is proposed that a better understanding of the interface properties between TBC and underlying TGO is needed to improve TBC performance and durability. The chapter concludes with a review of the understanding of thin films growth, which is focused on the development of epitaxial zirconia films form from an aqueous precursor.

2.1 Crystal Structure and Physical Properties of ZrO_2 and Al_2O_3

2.1.1 Zirconia and yttria-stabilized zirconia

Pure ZrO_2 (zirconia, zirconium dioxide) is a typical polymorphic material which may exist in three different crystallographic modifications (Fig. 2.1).

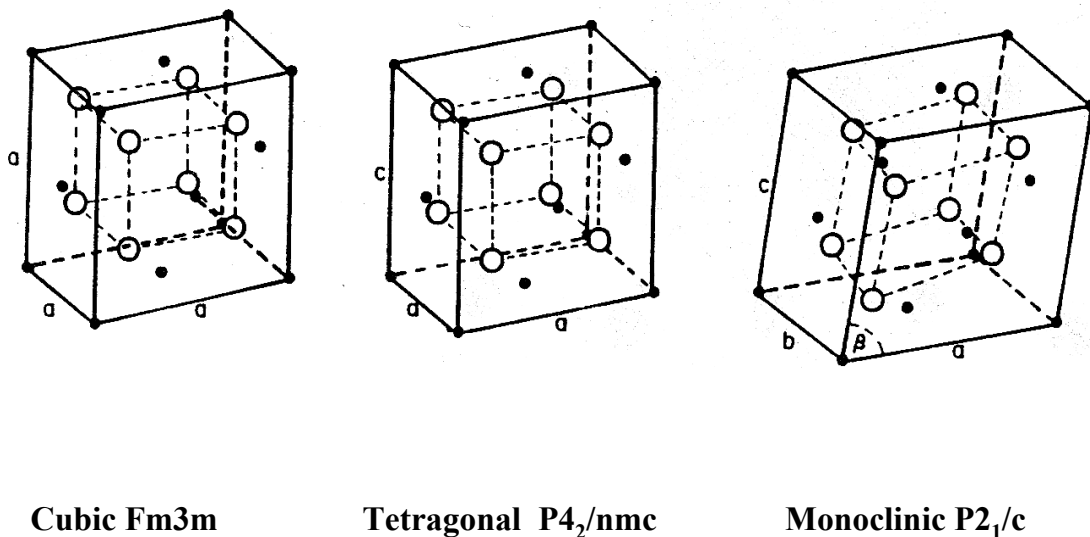


Fig. 2.1: Schematic representation of the three polymorphs forms of ZrO_2 [81Heu]

The cubic phase [Fm3m] is stable from the melting point 2680°C down to 2370°C. It crystallizes in fluorite crystal structure, in which ideally each Zr atom is coordinated by eight equidistant oxygen atoms [62SmC, 94YSK, and 96MBM]. The tetragonal phase [P4₂/nmc] is stable between 2370°C and 1130°C. The tetragonal structure is derived from the fluorite-type structure by the shift of the oxygen ions from their ideal fluorite sites along one of the cubic axes [62Teu, 79MCF, 81KFK, 94YSK, and 98HHK]. The axis along which this movement takes place is elongated to give a tetragonal distortion. The space group is formally P4₂/nmc (primitive) but, as is common, the structure is described on a face-centered tetragonal cell to emphasize its connection with the fluorite. The lattice parameters *c* and *a* are then nearly equal; and the tetragonal distortion is given directly by *c/a*. A schematic picture of the structural relationship between tetragonal cell and pseudo-fluorite cell is given in Figure 2.2.

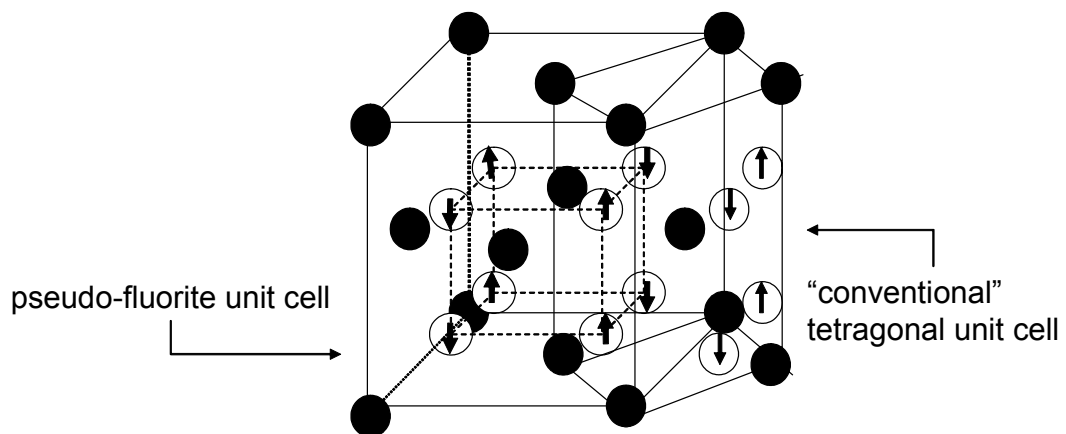


Fig. 2.2 Crystal structure of tetragonal ZrO₂ and relationship between the tetragonal and pseudo-fluorite unit cells. The solid circles are cations. The open circles are the anions with the displacement from their ideal fluorite positions.

The monoclinic phase [P2₁/c] is stable at all temperatures below 1170°C as represented by the naturally occurring mineral baddeleyite. This structure is described as a distortion of the cubic fluorite structure [59McT and 73BBG].

Industrially and scientifically, ZrO₂ is a very important refractory oxide, because of its high-melting point (*T_M* ~2700°C) and its chemical durability. Several important physical properties of t-ZrO₂ and YSZ are listed in Table 2.1.

Table 2.1: Physical properties of t-ZrO₂ and YSZ

Material Properties	t-ZrO ₂		3 mol% YSZ		References
	<i>a</i>	<i>c</i>	<i>a</i>	<i>c</i>	
Lattice Parameters Å	5.1505	5.1797	5.1023	5.1745	[86Sch, 88HHR]
Thermal Expansion Coefficient x 10 ⁻⁶ /C°	8.7	13.6	10.1	11.6	[64Sha, 86Sch]
Thermal Conductivity at 100°C-1300°C Wm ⁻¹ K ⁻¹	1.6-2.1		1.6-1.81		[86Bev, 96DBP]
Elastic Modulus GPa	200		218		[64Sha, 96RuR]

The low value of thermal conductivity is largely due to the scattering of phonons by the lattice imperfections such as oxygen vacancies, grain boundaries or atoms of different masses. For both pure ZrO₂ and YSZ with low concentrations of Y₂O₃, the value of thermal conductivity is typical of a crystalline solid, with the dominant phonon-phonon scattering mechanism. The reduction in thermal conductivity with Y₂O₃ addition is explained by the shorter mean free path owing to local modifications of the lattice structure and introduction of vacancies. These vacancies act as scattering centers for phonons, thereby directly increasing phonon dispersion in the lattice. With increased dispersion, there is a high probability that phonon-phonon interactions will occur whereby the mean free path will be further reduced [98KIG, 01ScP, and 02NLJ].

Addition of dopants has influence on the conductivity of ZrO₂. The electrical conductivity increases with the temperature. The anionic defects lead to high ionic conduction at high temperature (500°C to 1200°C). The ionic conduction occurs due to the migration of O²⁻ ions through vacant ion sites when Zr⁴⁺ ions are partially replaced by dopant ions having a valence less than 4+. The oxygen vacancies are required for charge compensation when Y³⁺ ions substitute for Zr⁴⁺ cations in yttrium-doped ZrO₂ [83PJD].

2.1.2 α -Alumina

A number of transitional Al₂O₃ structures can form initially with increasing temperatures, but all metastable structures are transformed irreversibly to α - Al₂O₃. At ambient pressure α - alumina is the only one thermodynamically stable phase of Al₂O₃ and it is generally used for

structural and electrical application. Sapphire ($\alpha\text{-Al}_2\text{O}_3$, $\alpha\text{-alumina}$) crystallized in corundum structure (space group $R\bar{3}c$) and its crystallography is described by *Kronberg* [57Kro]. Two types of unit cell can be considered: the morphological unit cell defined by mineralogists and the structural unit cell defined by X-ray crystallographers [57Kro and 85LeL]. The crystal structure is often described as having oxygen anions in a hexagonal close-packed (hcp) arrangement with and aluminum cations occupying two-thirds of the interstitial octahedral sites.

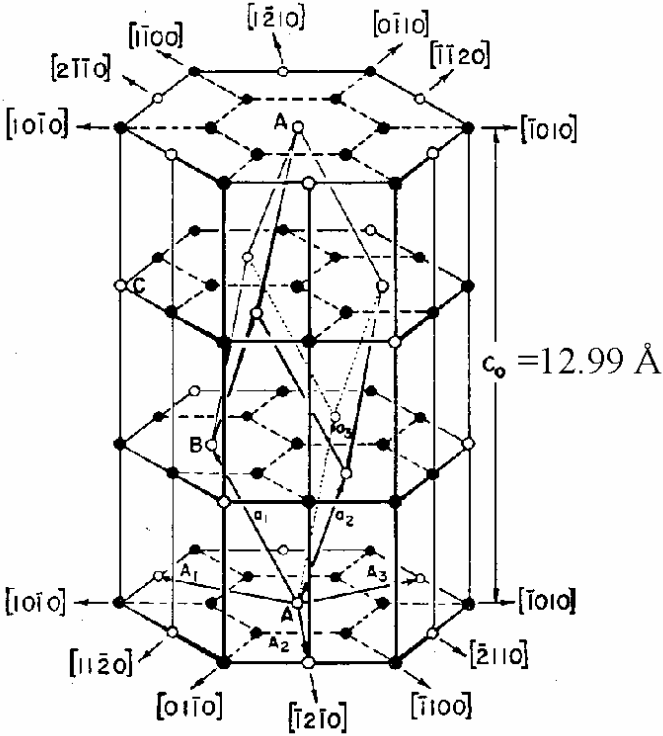


Fig. 2.3 The cation sublattice in sapphire after *Kronberg* [57Kro]

Because of a strong chemical bond strength between the Al ions and O ions (as expected from the value of heat of formation -400 Kcal/mol) alumina has outstanding physical stability, reflected in a high melting point (2050°C), the highest hardness among oxides (85 R45N), and high mechanical strength. Table 2.2 shows the lattice parameter and some thermo-physical properties of $\alpha\text{-Al}_2\text{O}_3$.

Table 2.2 Thermo-physical properties of α -Al₂O₃

Material Properties	α -Al ₂ O ₃		References
	<i>a</i>	<i>c</i>	
Lattice Parameters Å	4.7589	12.991	[85 LeL]
Thermal Expansion Coefficient x 10 ⁻⁶ /C°	7.5	8.02	[02 SRW]
Thermal Conductivity at 100°C-1300°C Wm ⁻¹ K ⁻¹	2.8-1.3		[86 Bev]
Elastic Modulus GPa	393		[81 SDS]

2.2 Thermodynamics of the ZrO₂ – Y₂O₃ system

Undoped ZrO₂ exhibits the following phase transformations [91 DJH, 95 YMT, and 96YKY]:



The monoclinic to tetragonal phase change (at elevated temperature) with the accompanying volume change (7.5%) precludes the use of pure zirconia.

Doping with aliovalent oxides (CaO, MgO or Y₂O₃) stabilizes the high-temperature cubic and tetragonal phases to room temperature leading to both an increase in the oxygen vacancy concentration and an enhancement of the oxygen-ion conductivity. Many features (ionic conductivity, thermal conductivity, fracture toughness, strengths) strongly depends on the existing phases and structural changes. Therefore the phase diagram depicted in the temperature-composition (concentration of dopant as YO_{1.5}) and the structural change are of importance for the technological applications.

The subsolidus equilibria in the ZrO₂ – rich portion have been investigated by many authors [51DBO, 74SPC, 75Sco, 84RMV, 84RCH, 88HCL, and 88Stu]. The review of the phase equilibrium and thermodynamic properties of the Y₂O₃-ZrO₂ system is given by [91DJH, 96YKY, and 03FaA]. However, there is no general agreement among the proposed phase

diagrams. This is associated with the sluggish diffusion kinetics at temperatures below 1200°C, the formation of metastable phases, the difficulties in conducting experiments at high temperature, etc.

The ZrO_2 – rich portion of the equilibrium phase diagram $\text{ZrO}_2 - \text{Y}_2\text{O}_3$ is important for the usage and fabrication of the TBCs. YSZ-based TBCs containing $7 \pm 1 \text{ wt\% Y}_2\text{O}_3$ were found by NASA to be optimal for the thermal-cycling durability of PS TBCs [85Ste]. In principle, these materials should operate in the temperature range of 1000°-1500°C. The success of this composition is critical to the presence of the t' phase in TBCs, whether they are deposited by plasma spray (PS) [81MSG] or by EB-PVD [93LAD]. The t' phase is essentially metastable single phase with tetragonal structure, supersaturated with yttrium. The t' phase is described by [81MSG and 89LAD] as a “non-transformable t' - ZrO_2 ”. The non-transformability relates to its resistance to undergo the martensitic $t \rightarrow m$ transformation upon cooling. This transformation is undesirable especially by thermal cycling conditions because of its destructive effect associated with the 4% volume expansion. The condition for boundary line of such metastable transformation is thermodynamically defined by *Yashima et al.* [96YKY] as the temperature and composition where Gibbs energies of cubic and tetragonal phases are equal (T^0 line). The calculated T^0 (t/m) line along with an enlarged portion of equilibrium phase diagram is presented in Figure 2.4 [03FaA]. The non-transformability of t' phase requires minimum yttrium content which is given by the intersection of the T^0 (t/m) curve with the lowest operating temperature. The maximum Y content in t' phase, which can be obtained in the practice, is given by the intersection of the T^0 (c/t) line with the ambient temperature. The t' phase is formed in PS TBCs when molten splats, having solid field in the cubic phase field, transformed diffusionless into the metastable t' phase upon rapid cooling below the T^0 (c/t). In case of EB-PVD TBC, since the condensation occurs at substrate temperatures below the T^0 (c/t), the t' phase is formed directly from the vapor [93LAD and 94UMH]. Thus, the T^0 lines define the upper and lower boundaries of the metastable t' phase that can be produced under conditions of diffusion-limited crystallization (PS or EB-PVD growth of TBCs). The thermal cycling between $\sim 1500^\circ\text{C}$ and 25°C does not result in the disruptive $t \rightarrow m$ transformation since the phase does not cross the T^0 (t/m) curve upon cooling.

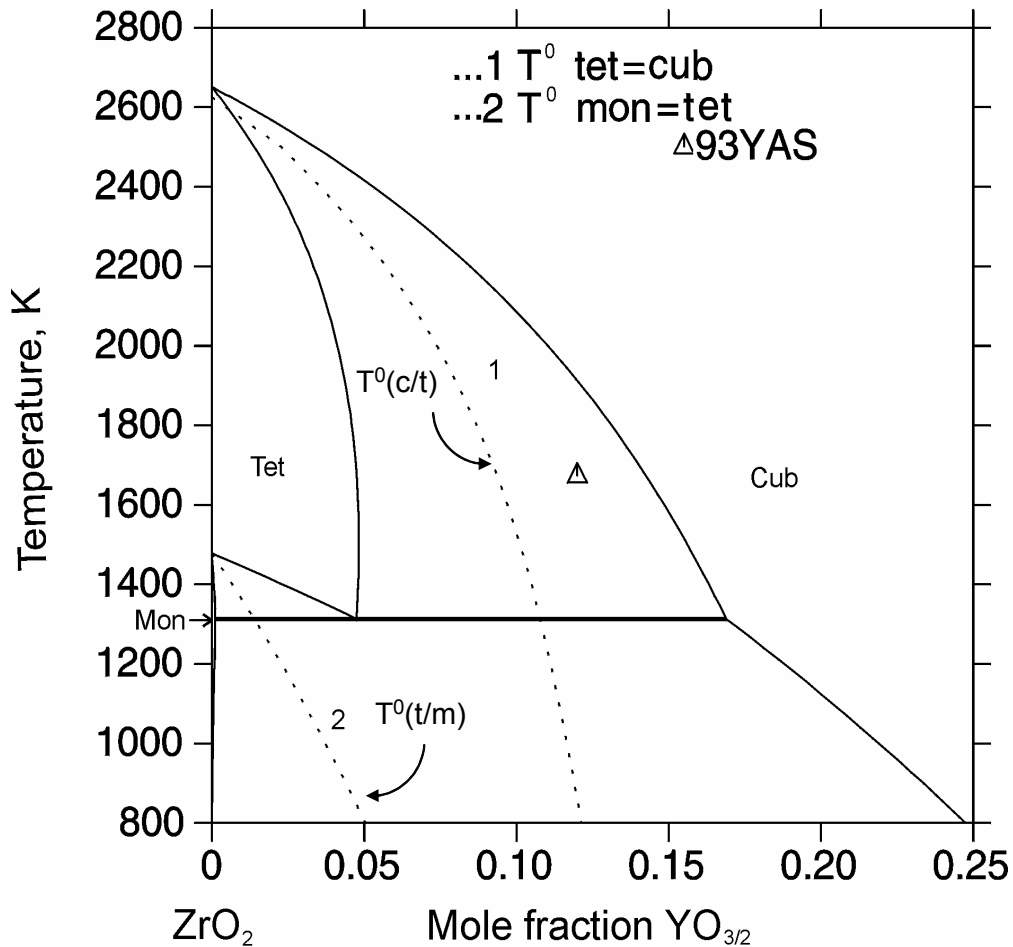


Fig. 2.4 ZrO_2 -rich side of the Y_2O_3 - ZrO_2 phase diagram, adapted from *Fabrichnaya and Aldinger* [03FaA]. The $T^0(c/t)$ curve defines the temperature as a function of composition for which the cubic (c) and tetragonal (t) phases have the same Gibbs free energy. Likewise the $T^0(t/m)$ represents the same for the t (tetragonal) and m (monoclinic) phases. These lines mark the upper and lower boundaries of stability, respectively, of metastable t' phase that can be produced under conditions of diffusion-limited crystallization (PS and EB-PVD YSZ growth of TBCs)

2.3 Microstructure of YSZ grown by EB-PVD

The most technologically advanced YSZ TBCs are deposited by electron-beam physical vapor deposition (EB-PVD). The coating possesses a columnar microstructure where high aspect ratio column grains span the full thickness of the film. The columns are isolated from each

other by voids (inter-columnar porosity) elongated perpendicular to the ceramic/metal interface. Since these pores are oriented predominantly parallel to the thermal gradient, they contribute only marginally to the thermal resistivity. However, these inter-columnar gaps in the microstructure permit a low in-plane elastic modulus, which has been proposed to be the source of their excellent strain tolerance [85Str and 98JRB]. In addition, these coating contain closed, intra-columnar pores at smaller length scale which lower the thermal conductivity to around 1-1.2 W/mK of the PS coating, compared to 2-2.5 W/mK in the bulk [01HLC].

2.3.1 Columnar growth

The processing parameters of the PVD affect the microstructure and the properties of the YSZ coating. *Movchan and Demchisin* [69MoD] first studied the processing/structure/property relationship in evaporated thick films. In this study, it was demonstrated that the effect of substrate temperature during deposition has an influence on the microstructure. The common structure model predicts three structural forms of zones as a function of T/T_M , where T is the substrate temperature and T_M is the melting point of the coating-material. The three characteristic zones with boundary temperatures $T_1 = 0.3T_M$ and $T_2 = 0.5T_M$ are shown in Figure 2.5. Each zone has its own microstructure and properties.

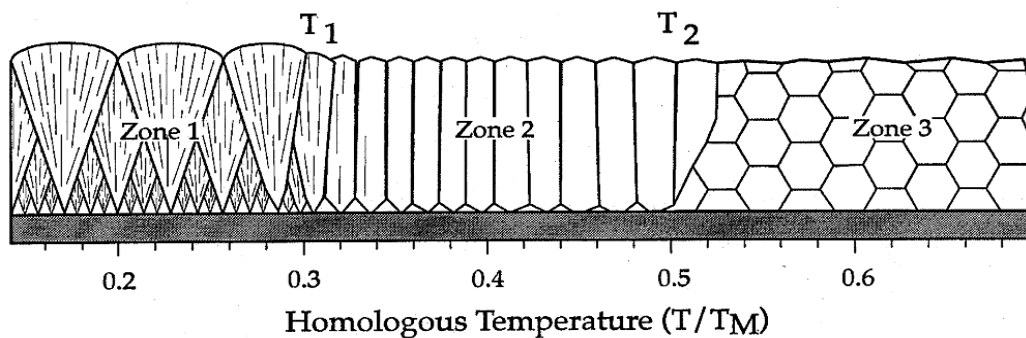


Fig. 2.5 Structure map [01Ter, adapted from 69MoD] dividing microstructure of PVD coating into 3 distinct zones based on the deposition substrate temperature normalized by the melting point of the evaporant. The temperature of the T_1 and T_2 zone boundaries in metallic films corresponds to the activation of surface diffusion ($T/T_M \sim 0.3$) and bulk diffusion ($T/T_M \sim 0.5$), respectively.

Zone 1 ($T/T_M < 0.3$) consists of characteristic tapered grains separated by each other by voided regions resulting from insufficient surface diffusion of adatoms and the effect of shadowing. Zone 2 ($0.3 < T/T_M < 0.5$) consists of parallel columnar grains with well defined grain boundary zones, resulting from surface diffusion-dominated condensation. The width of the columnar crystallites increases with the temperature. In Zone 3 ($0.5 < T/T_M$) the bulk diffusion is dominant, therefore the grains are no longer columnar, they are equiaxed.

The parametric study of direct evaporated zirconia films has been studied and distinctive transition temperatures of the microstructural zone were found as $T_1 = 648\text{K}$ ($T_1/T_M = 0.22$) and $T_2 = 1273\text{K}$ ($T_2/T_M = 0.45-0.5$).

Sanders [74San] suggested a structural map with classification based on dominant physical processes such as a shadowing (a simple geometric interaction between the roughness of the growing surface and the angular directions of the arriving coating atoms), surface diffusion, bulk diffusion, and desorption. Thus various of the basic process can be expected to dominate over different ranges of T/T_M and to manifest themselves as differences in the resulting coating structures. The three lower ranges are similar to these presented in the model of *Movchan and Demchisin* [69MoD]. In range 1 ($T/T_M < 0.1$) shadowing dominates; in range 2 ($0.1 < T/T_M < 0.3$) surface diffusion dominates; in range 3 ($0.3 < T/T_M < 1$) bulk diffusion is significant. The higher T/T_M ranges refer to liquid condensation.

Thornton [77Tho] added as an additional parameter to the substrate temperature the effect of inert gas pressure and proposed the diagram shown in Figure 2.6.

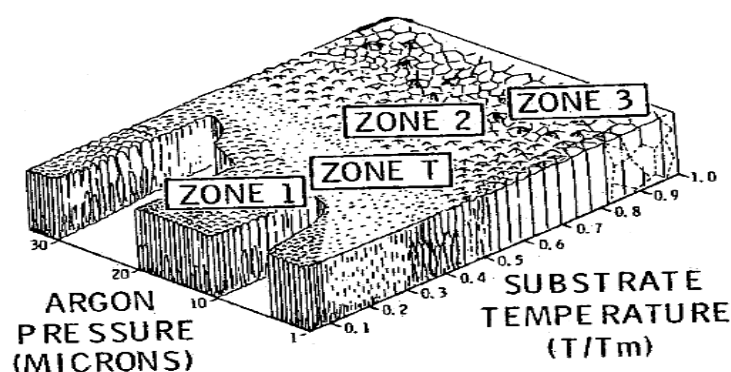


Fig. 2.6 Model proposed by *Thornton* [77Tho] for high rate thick film growth.

The pronounced Zone 1 structure was promoted by substrate roughness, high argon pressure, and an oblique component to the deposition flux. As mentioned earlier, the Zone 1 structure occurs when surface diffusion is insufficient to overcome the effects of shadowing. A transition zone (Zone T), which consists of poorly defined fibrous grains without voided boundaries, was identified between Zone 1 and 2. Coatings with such structure grow on smooth substrates at low T/T_M such that the atom diffusion largely overcomes the roughness of the substrate and the initial nucleation. Columnar grains in Zone 2 tended to have highly faceted surfaces. They are separated by dense intercrystalline boundaries. The growth is described by surface diffusion growth model. It occurs for $T/T_M > 0.3$ Zone 3 is characterized by bulk diffusion process such as recrystallization and grain growth. For $T/T_M > 0.5$ grain shape may be equiaxed or columnar, depending on structure and stress distribution formed during initial deposition.

2.3.2 Crystallographic texture

Simultaneously with the growth of columnar grains occurs the evolution of the crystallographic texture. A several mechanisms are distinguished to cause the texture in films growth by PVD: epitaxy on a single crystal substrate, preferred orientation of nuclei on amorphous substrate, recrystallization orientation, etc. In case of growth orientation, the resulting crystallographic texture has been explained by *Van der Drift* [67Van] with a mechanism termed “*evolutionary selection*” which states that the crystals with the highest component of the growth rate in the direction perpendicular to the incident vapor are selected, crowding out the unfavorably oriented grains. This yields films in which even an initially randomly oriented array of grains becomes increasingly oriented with increasing the film thickness (Fig. 2.7). A thick film for which growth is characterized by evolutionary selection would be dominated by grains extending through the entire film thickness with nearly the same “fast growth” axis giving the film a strong fiber texture.

The texture of PVD films is often sensitive to pattern of vapor incidence as reported by *Bauer* and *Van der Drift* [64Bau and 67Van]. The pattern of vapor incidence is characterized by the angle α between the substrate normal and average direction of vapor incidence. The two simplest patterns of vapor incidence arise when a stationary substrate is oriented normal ($\alpha = 0^\circ$) or oblique ($\alpha \neq 0^\circ$) to the vapor flux.

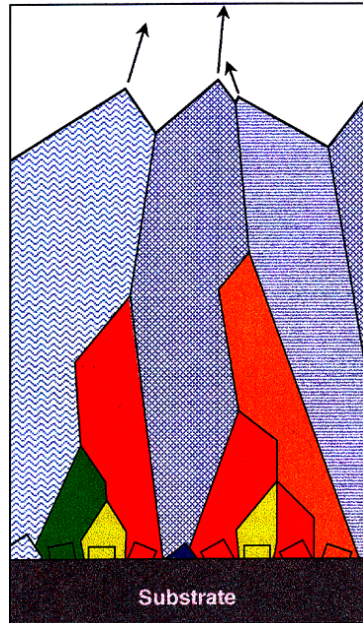


Fig. 2.7 Columnar growth by evolutionary selection begins with an initial array of randomly oriented nuclei. Nuclei oriented such that their preferred growth direction is oriented parallel to the incident vapor flux grow fastest, crowding out the unfavorably oriented neighbors. As a consequence, the crystallographic texture increases in sharpness with increasing film thickness. Figure adapted from *Van der Drift and Terry* [67Van and 01Ter]

The texture of PVD films is also influenced by several deposition parameters, including substrate temperature (T_s), deposition rate, deposition on a stationary or rotating substrate, and in some cases by activation of the vapor by plasma sources. There are many disagreements in the earlier literature regarding the texture orientation of TBCs as a function of deposition condition as T_s , α or rotating of the sample. Recent investigation of the microstructure and texture of YSZ TBC by [94SBS and 00ScS] reveal for coating deposited on stationary substrates a fiber texture with mainly $\langle 113 \rangle$ and $\langle 111 \rangle$ fiber axis depending on the vapor incidence angle and temperature. The results agree with published data in [99TLL and 01Ter] where for different substrate temperatures and vapor incidence angles of 0° and 45° mainly $\langle 111 \rangle$ and $\langle 101 \rangle$ axis as preferred growth direction were reported. The change in the texture with increasing temperature under normal incidence on the stationary substrate is linked to changes in the mechanism of crystal growth. The pattern of vapor incidence has a stronger influence on texture than substrate temperature.

In addition to the out-of-plane orientation, TBCs deposited on rotated or obliquely oriented stationary substrates [93SFP and 01Ter] contain an in-plane orientation. It is shown, for

deposition on stationary substrate, that a increase of the angle of vapor incidence to 45° favors biaxially aligned columnar growth in the $\langle 110 \rangle$ direction. The formation of biaxially texture can be explained via evolutionary selection of fastest growth direction. Crystallites that have a higher growth rate than others became dominant because of the shadowing process which is effective during the columnar growth of PVD films [01Ter]. Thus, types of columns with an unfavorable in-plane orientation are screened out causing the emergence of an in-plane orientation.

The preferred out-of-plane orientation for TBCs deposited on substrates rotated about axis orthogonal to the vapor has been reported by several groups and general is found to be $\langle 100 \rangle$ [93LAD, 94UMH, 94SBS, 96SOB, 00ScS, and 01SLC] but also $\langle 111 \rangle$, $\langle 110 \rangle$, and $\langle 113 \rangle$, depending on the deposition parameters. Mainly chamber pressure, biased substrates and substrate temperature were determined to be responsible for the individual texture development. All these studies were based only on standard diffraction experiments, by that providing only limited information on complete grain orientation. Pole figures study by [93LAD, 96SOB, 00ScS, and 01Ter] for rotated samples, indicated exclusively a four-fold symmetry with a $\{100\}$ plane parallel to the substrate.

Biaxially aligned zirconia films, other then TBC, have also been grown by a different vapor deposition processes under normal vapor incidence (ion beam bombardment) [96MRS and 97MRY]. Here again the mechanism responsible for in-plane orientation is an evolutionary selected process. Grains oriented with specific channeling direction follow the direction of the bombarding ion beam resputtered less than other oriented grains, which causes the (100) orientation to emerge from the initial random distribution.

Experiments and mathematical models by *Terry* [01Ter] strengthen the argument that biaxial alignment of columns occurs via the down-selection of initially randomly oriented grains to those whose orientation satisfies the criteria that equal amounts of flux impinge on all faces of the column tip and thus sensitive to the pattern of vapor incidence. The model which is derived describes the amount deposited per revolution, h , on each of the four facets of a $\langle 100 \rangle$ oriented, isolated column tip as a function of in-plane rotation, ϕ , and column tilt in the plane of vapor incidence, β (as indicated in Fig. 2.8).

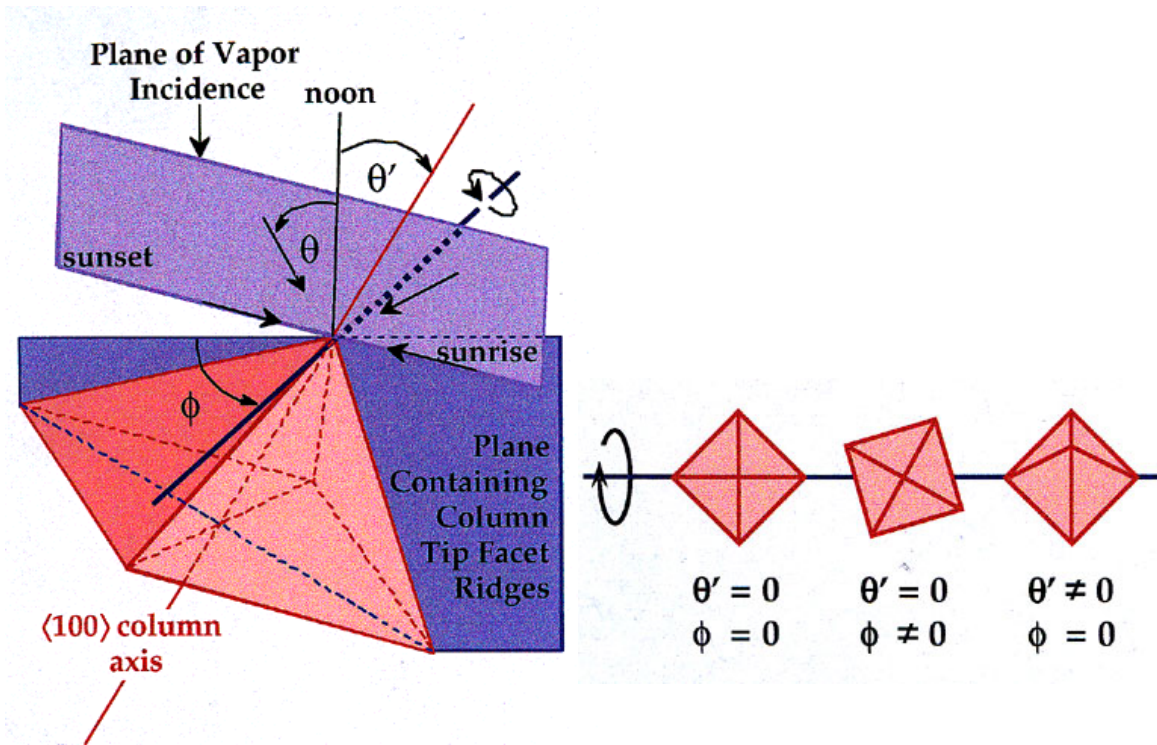


Fig. 2.8 Tip morphology relative to rotation axis for a column which is aligned (left), rotated along surface normal (middle), and rotated in the plane of vapor incidence (right). Figure adapted from Terry [01Ter]

The ratio between maximal and minimal amount of deposition reaches unity only for $\beta = \phi = 0^\circ$ (and by symmetry for $\phi = 90^\circ, 180^\circ,$ and 270°). Columns with different orientations have a facet flux ratio less than unity, resulting in unstable growth of the column tip. Growth of these columns is eventually extinguished as they impinge upon the sides of more favorably oriented ($\phi \sim 0^\circ$) neighbor grains. As a consequence of this evolutionary selection, thick TBCs grown on rotated substrates have an in-plane alignment in which diagonals of the column tips are oriented parallel to the axis of substrate rotation. The survival of these column leads to an additional evolution of the in-plane orientation ending in a preferred orientation of the $\langle 100 \rangle$ direction of the crystallites relative to the rotation axis.

In general, $\langle 100 \rangle$ texture is only observed on rotated substrate. However, a recent report [01HCL] indicates that the crystallographic orientation of the substrate can influence TBC texture to such extent, that a $\langle 100 \rangle$ fiber texture has been obtained even during stationary deposition on polished, single crystal substrate.

2.3.3 Microstructure of the Interface

The durability of the YSZ coatings on the metallic substrate depends upon the adhesion of the ceramic to the bond coat, as well as the stability of the ceramic coating itself. In order to

improve the adhesion oxidation processing is generally performed after the coating process by forming protective oxide scales of predominant α -alumina.

Early investigations of the interface microstructure between the TGO and the columnar YSZ grain structure [94UMH, 97FSL, 99SYT, and 00ScS] indicate the presence of fine-grained randomly oriented zirconia grains. The interface between these grains and columnar grains is noncontinuous and irregular. The grains of zirconia in the TBC close to the substrate show no tendency to epitaxy to the substrate and have no texture. The presence of a thin dense zone containing nanosized crystals is explained by *Strangman* [85Str] with the evaporation conditions. At the very beginning of coating's growth, deposition is performed under substoichiometric depositions caused by a reduced oxygen supply within the deposition chamber. These conditions were assumed to be responsible for the formation of this zone and for the good bonding of EB-PVD TBCs to the TGO. In [00ScS] the fine-grained zone is observed in cases under fully oxygen flow. Although the detailed mechanism of formation of this zone is not yet fully understood, microstructural observations by *Schulz et al.* and *Terry* [00ScS and 01Ter] reveal that a large number of nuclei must be present. The fine-grained nucleation mode at the beginning is presumed to be due to a high supersaturation. This is because the temperature of the vapor arriving at the substrate is $\sim 3500^\circ\text{C}$, while the substrate temperature is $\sim 1000^\circ\text{C}$. The mobility of the condensing adatoms is ruled mainly by their energy or whether they are charged. Additionally, condensation and crystallization energy are not effective in the early stages of growth and hence the heating rate is relatively low. This may hinder the immediate formation of lattice orientation with higher growth rates and/or low energetic places for the adatoms. To explain the thickness varying of the fine-grained zone for the rotating samples, the authors proposed a geometrical model. It takes into account the position of the sample with regard to the vapor source prior to the first complete rotation.

2.4 Microstructure of YSZ grown by precursor methods

2.4.1 YSZ grown on sapphire substrates

During the last decade the liquid precursor technique has been used for the growth of epitaxial thin films. The epitaxy phenomena associated with the solution precursor method is different from phenomena known for vapor phase epitaxy, since the epitaxial development results from crystal growth during post-coating heat treatments of the substrates.

Three different solid-state epitaxy mechanisms have been identified by *Cain and Lang* [94CaL]. One involves the consumption of other polycrystalline grains by grains at the

film/substrate interface that crystallize during decomposition with the same orientation as the substrate. This mechanism is known to occur when the structure of the film and substrate are similar. A second mechanism involves a reaction of the polycrystalline film with the substrate to produce an oriented grains of a third phase that grow together to form a single-crystal thin film. A third mechanism is expected whenever the structures of the film and substrate are dissimilar and the two materials do not react to form a third phase. In this mechanism, grains within the polycrystalline film undergo normal grain growth until they form a columnar microstructure. As reviewed by *Thompson et al.* and *Lang* [90TFS, 90Tho, and 93Lan] the subsequent grain growth in thin films with columnar structure occurs via abnormal grain growth. The columnar grains with a lower interfacial energy due to a special orientation grow at the expense of the usually static matrix of normal grains. For single crystal substrates, the in-plane orientation of abnormal grains is generally dictated by the substrate. When the crystal structure (lattice parameter) of the film and substrate are sufficiently different, one out-of-plane orientation may have different crystallographic related in-plane variants with identical interfacial energies. Concurrent with the abnormal growth of oriented grains an instability may occur causing the polycrystalline film to break into isolated islands that also lowers the free energy by uncovering the substrate [90MLM and 93Lan].

The abnormal grain growth and concurrent morphological instability were found by *Miller* and *Lang* [91MLa and 94CaL] for the growth of cubic $Zr(Y)O_2$ 25nm thick films deposited onto basal and prismatic planes of sapphire. The authors found that all abnormal grains had the same $[100]_{YSZ} \parallel [0001]_S$ out-of-plane orientation for the C-plane and $[100]_{YSZ} \parallel [\bar{1}2\bar{1}0]_S$ for the A-plane relative to the sapphire substrate but different in-plane orientation. For the C-plane, three nonredundant, in-plane ZrO_2 orientations were observed (Fig. 2.9). The 3 in-plane variants, viz., $[010]_{YSZ} \parallel [\bar{1}2\bar{1}0]_S$ are related to one another by a 120° rotation about $[0001]_S$. For the A-plane, four different in-plane rotational orientations were observed for the $[100]_{YSZ}$ relative to the $[0001]_S$; 1) 0° : $[100]_{YSZ} \parallel [0001]_S$; 2) $\pm 32^\circ$: $[100]_{YSZ} \parallel [1\bar{1}01]_S$; 3) 19° : $[0\bar{1}3]_{YSZ} \parallel [10\bar{1}0]_S$.

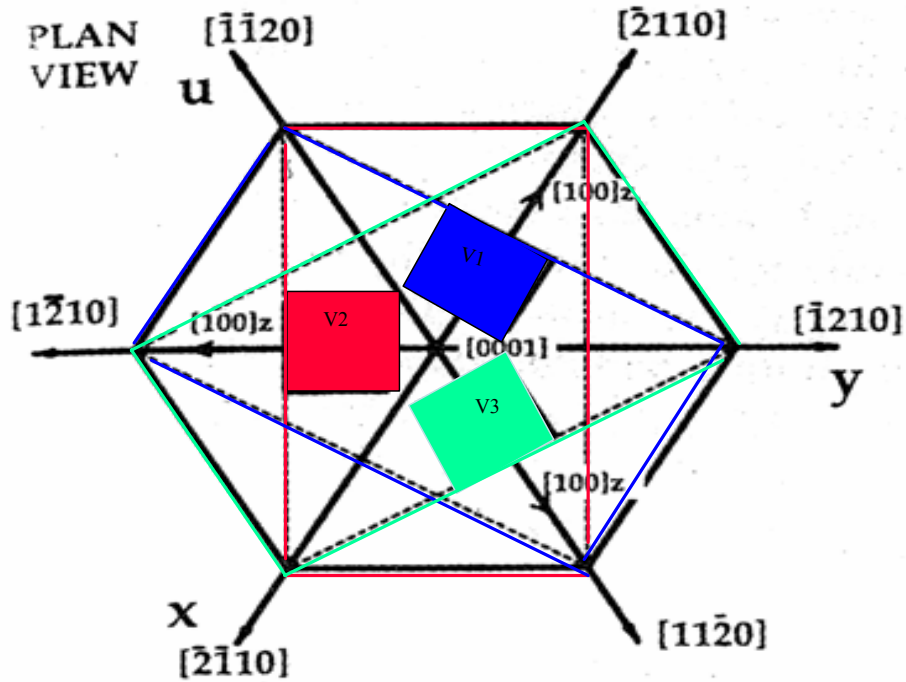


Fig. 2.9 Schematic of in-plane orientation relations of c-ZrO₂ epitaxial grains on C-plane sapphire substrate. Figure adapted from *Cain and Lang* [94CaL].

The epitaxial development of undoped zirconia films deposited on (11 $\bar{2}$ 0) oriented sapphire substrate was examined by *Mary et al.* [98MGT]. It is demonstrated that after high temperature treatment, all zirconia islands were single crystals exhibiting exact in-plane orientation: $\{100\}_{Zr} \parallel (11\bar{2}0)_s$ or $\{111\}_{Zr} \parallel (11\bar{2}0)_s$. It is concluded that islanding and epitaxy phenomena arise from competitive grain growth in which misfit strain energy plays a selective role.

As mentioned earlier, concurrent with the abnormal grain growth, morphological instability (breakup of the film) by treatment at higher temperature is commonly observed for many different polycrystalline film/substrate systems. The breakup process favors those grains that have a low substrate interfacial energy and so produces a film of highly oriented but isolated grains. An understanding of this instability phenomenon was developed first by *Srolovitz and Safran* [86SrS]. They calculated the growth of pin holes in thin films and suggested that a pin hole in a polycrystalline thin film could result from the deepening of the grain boundary groove at a three grain junction during grain growth. *Agrawal and Raj* [89AgR] found that thin films of polycrystalline zirconia, deposited on a sapphire substrate become gradually discontinuous when annealed at high temperature. The mechanism for the break up of the film

is identified as a nucleation and growth of cavities formed between the zirconia grain boundaries at the substrate interface. The criterion for autonucleation of cavities is defined in terms of the influence of the wetting angle (depends on the interfacial energy). When the contact angle between the film and substrate is large compared to the grain boundary dihedral angle in the film the cavities can nucleate spontaneously and growth by surface diffusion.

The zirconia/sapphire interface energy is anisotropic. The grain orientation in the as deposited films was textured. After long term annealing, the preferred orientation changes, implying that the energy of zirconia/sapphire interface is sensitive to the orientation and it is also temperature dependent. *Miller et al.* [90LML] reported experimental evidence for $Zr(Y)O_2$ thin films on unoriented sapphire substrates, showing that, indeed, small holes develop at three grain junctions when larger grains consume smaller grains by either grain boundary motion or grain coarsening and then “spheroidize” to minimize their surface energy. They also presented thermodynamic calculations showing that the breakup process lowers the free energy of the system when the grain size to film thickness ratio exceeds a critical value, which depends on the dihedral angle (a measure of the grain boundary to surface energy ratio) and the solid-state wetting angle of grains with the substrate. Summary of the thermodynamic calculation with an equilibrium configuration diagram is shown in Figure 2.10, where the ratio D/t is plotted as a function of the wetting angle for a specific value of the whole dihedral angle.

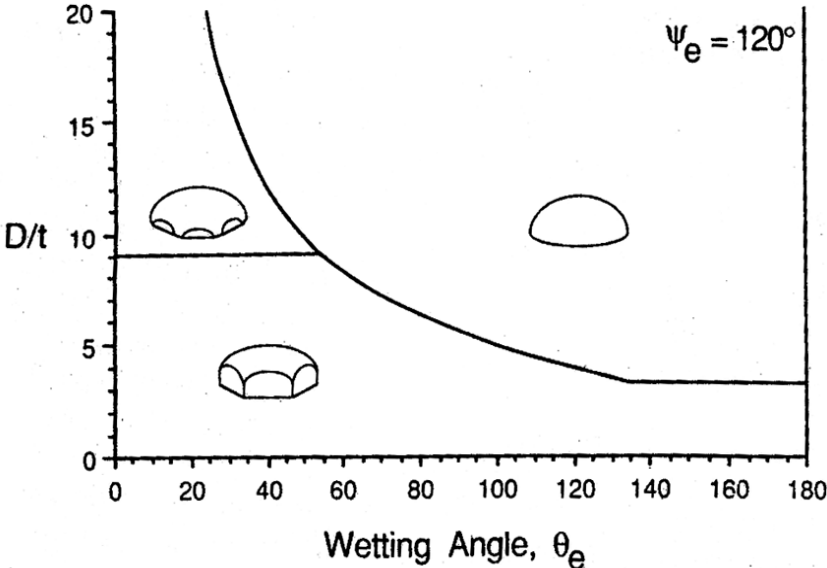


Fig. 2.10 Equilibrium configuration diagram for polycrystalline thin films with columnar microstructures. Boundaries represent the conditions (D/t and solid-state wetting angle) where different configurations have the same free energy. (D is the average grain size, and t is the film thickness) after *Lange* [93Lan].

2.4.2 YSZ growth on single crystal ZrO_2

When the crystal structure of the film and substrate are sufficiently similar epitaxial grain growth can initiate at the substrate-film interface before the columnar grain microstructure is established with only one out-of-plane orientation and one in-plane variant (i.e., a true epitaxial thin film) [93Lan]. Details on the mechanism leading to the formation on the single crystalline thin film from the initial polycrystalline thin film are given by *Miller et al.* [93MCC]. Heteroepitaxial single crystal thin films of ZrO_2 (25 mol% Y_2O_3) have been deposited on single crystal, (100) oriented ZrO_2 (9.5 mol% Y_2O_3) substrates. Film compositions crystallizing with the cubic structure had a mismatch up to 1.59%. The epitaxial film grows from a very thin epitaxial layer, produced at temperatures less than $600^\circ C$ ($0.3T_M$), by consuming a very fine grained porous polycrystalline thin film. Porosity accumulates at the growing interface, producing a dense epitaxial layer in its wake. Strain energy, produced during epitaxy, due to lattice mismatch, can not be relaxed by forming an interfacial dislocation network until the film exceeds a critical thickness [75Mat].

3. Model Systems Processing and Sample Preparation

3.1 Precursor Derived Islands

Liquid methods, which include sol-gel, metal-organic deposition and aqueous salt deposition processes, offer a great potential for forming oxide thin films. In these processing methods, precursor chemicals are dissolved in an appropriate solvent, deposited as a thin film by dipping or spinning, then decomposed by heat or chemical reaction to form an amorphous oxide, and heated to crystallize and densify into an oxide thin film of desired composition and thickness. The initial film is not fully dense until heated to higher temperatures owing to the evolution of volatile components during decomposition. Among the advantages of liquid precursor methods are the ease of compositional control, the uniformity of composition, and the low cost of equipment. The capability of growing epitaxial oxide thin films is a desirable extension of the liquid precursor processes, and the possibility of such growth has been demonstrated in the zirconia-yttria system too [93 MCC].

A liquid precursor was used in this work to form YSZ thin films on C-plane polished sapphire single crystals [Frank & Schulte GmbH, Germany]. The samples were prepared at UCSB Materials Department by J. Cho. The following steps were adopted: The sapphire substrates were washed with an acid in a concentrated bath of 9.5M NH_4OH /1.0M NaOH solution and thermally annealed at 1300°C for 1h in air to remove any residual stresses induced during polishing. An aqueous solution containing zirconium acetate and yttrium nitrate was prepared such that the decomposed $\text{Zr}(\text{Y})\text{O}_2$ solid-solution contained 7wt% Y_2O_3 . The solution was then spin coated on the sapphire substrates at a rate of 5000rpm for 30 seconds to produce the gel-like film. The samples were transferred into a tube furnace and pyrolyzed at 1000°C for 2h, followed by further annealing at 1100°C and 1600°C for 1h. During annealing a break-up of the film occurs resulting in separate grains (islands). These islands are single crystals and will intend to act as seeds for the vapor growth, which followed during electron beam-physical vapor deposition.

3.2 Electron-Beam Physical Vapor Deposition (EB-PVD)

Physical vapor deposition processes is a common technique for depositing thin coating by generating a vapor of a source material in a vacuum environment. The vapor condenses on the substrate surface followed by film nucleation and growth of a thin film. During EB-PVD

processing a high energy electron beam is focused (scanned) onto the ceramic ingot target, which melts the ceramic locally and produces YSZ vapor. The vapor deposits as a coating on the substrate surface, which is held in rotatable fixtures above the vapor source [96 Jon]. The samples investigated in this work were prepared by J. Cho using this equipment at UCSB. Figure 3.1.gives a schematic representation of electron beam physical vapor deposition (EB-PVD) coating process as depicted by *Terry* [99 TLL and 01Ter] The system consists of a cubic high-vacuum chamber, 60cm on the side, with a 10kV, 270° electron-beam gun [AIRCO/Temescal SFIH-270-1] with a 7cm³ water-cooled copper crucible to hold the target evaporant. The gun was driven by a 14kW power supply [AIRCO/Temescal CV-14]. The deposition rate is monitored using a shuttered quartz-crystal sensor [Leybold-Inficon CrystalSix]. Intermittent sampling of the vapor flux prolongs the life of the quartz-crystals under high rate conditions. The sensor signal is fed into a closed-loop controller for the electron-gun [Leybold-Inficon IC/5]. Rapid filament degradation at higher pressures imposed a maximum allowable chamber pressure of 5x10⁻⁴ torr for operation of 270° gun. This limited the deposition rate for stoichiometric YSZ film to ~3.5µm/min (referred to a stationary substrate under normal incidence). This rate is significantly lower than current industrial practice but close to the range used to develop the structure map discussed in [69 MoD].

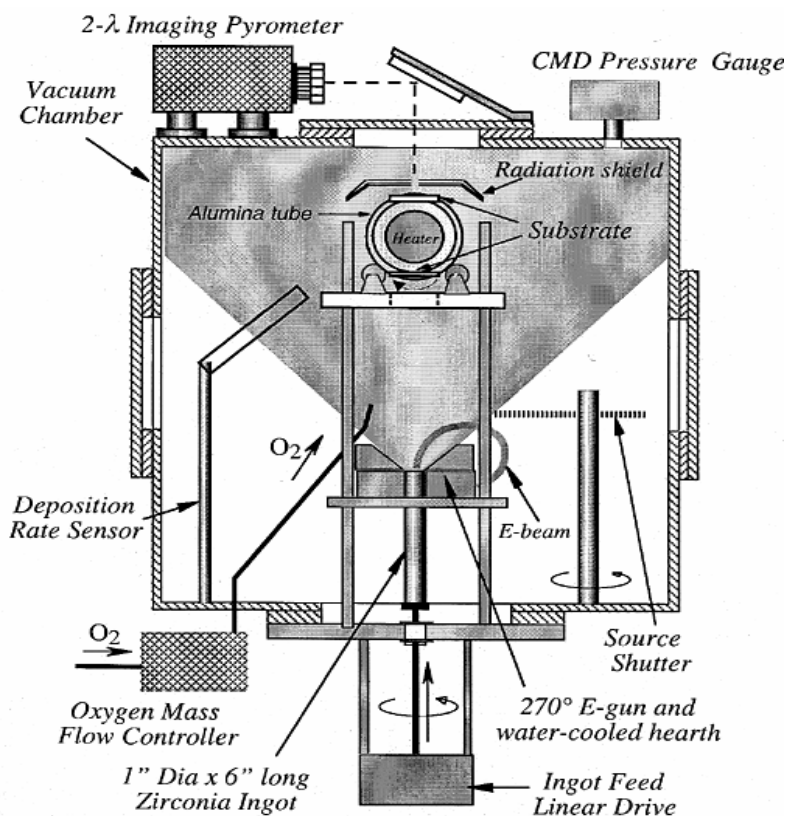


Fig. 3.1 Schematic representation of UCSB EB-PVD TBC coater configured for deposition on stationary and rotating substrates. Figure referred to [01Ter]

Other electron-beam gun [Consarc Inc.(Rancocas, NJ)] was used to deposit a second production run (series/issues): samples SS#16 and SS#11 (see Table 3.1), described later in Chapter 5. This allowed a TBC deposition at higher rate. The new system is composed of a 40kV, 20kW electron-beam gun, power supply, and beam guidance system. In addition to having the power required to produce higher evaporation rates, this gun design can also tolerate the high work chamber pressure, which limited the capability of the 270° gun. Total chamber pressure was regulated via feedback-controlled variable conductance exhaust valve. Pressure was measured with capacitance manometer diaphragm gauge [MKS 127A] for the runs of experiments using the Temescal Gun. For experimental runs using the Consarc Gun, the pressure was measured with a Bayard-Alpert ion gauge and thermocouple gauge.

The ceramic ingots used for TBC deposition were 25x75mm with nominal composition of ZrO_2 -7wt% Y_2O_3 (Trans-Tech, Adamston, MD), Major impurities reported are (in weight percent) 1.35 HfO_2 , 0.08 TiO_2 , 0.02 SiO_2 with ≤ 0.01 each of CaO , MgO , Al_2O_3 , Fe_2O_3 , Na_2O , U and Th. The ingot density is $3.77Mg/m^3$, equivalent to a porosity content of ~38%.

The substrates were polished [0001] sapphire single crystal with dimensions of 20x15x1mm [Frank & Schulte GmbH, Germany]. The sapphire substrates were mounted on the stage and resistively heated to the deposition temperature of 1000°C using a 20V AC power. For TBC deposition on rotating substrates, a special substrate stage was built. The stage consisted of a stationary cartridge heater with a 100mm long hot zone inserted into an alumina carrier tube with diameter of 38mm. Substrates were affixed over two windows machined 180° apart in the center of the tube, allowing the substrates to be heated radiatively as they experience a range of vapor incidence that varies from $\alpha = -90^\circ$ to $+90^\circ$ through the course of a single rotation. The holder was closed on one end and rotated at 8rpm along an axis perpendicular to the incident vapor flux. For stationary deposition in the UCSB coater, the temperature was monitored using a thermocouple, spot-welded to the substrate, and controlled within $\pm 10^\circ C$ of the desired value of 1000°C. For the case of TBC deposition on rotated substrates, the substrate temperature was measured by pyrometry non-contact method [Surface Imaging Pyrometer, Stratronics, Inc., Laguna Hills, CA]. For both the cases, temperature calibration the sapphire samples were coated with thin Cr/Ni double layer to provide good heat conduction to sapphire from a heating element. The samples were then annealed at 1050°C for two hours with Ar flow. The deposition parameters for different samples are summarized in a Table 3.1.

Table 3.1 TBC growth conditions. The substrate temperature for all cases is 1000°C

Samples	Substrate	Thickness of YSZ (μm)	Deposition Time (min)	Deposition Rate ($\mu\text{m}/\text{min}$)	Substrate Rotation (rpm)	Chamber Pressure (mtorr)
SC#1	C-sapphire	19	68	0.3	8	0.41
SC#3	C-sapphire	19	20	1.0	0	0.30
SC#5	C-sapphire	40	170	0.24	8	0.30
SS#16	seeds 1600°/1h on C-sapphire	22	19	1.2	8	6.0
SS#11	seeds 1100°/1h on C-sapphire	22	19	1.2	8	6.0
SS#14	seeds 1400°/15h on C-sapphire	14	48	0.3	8	0.42

3.3 Samples preparation

3.3.1 Metallographic Preparation

The preparation of hard, brittle ceramics is a demanding and time consuming process.

For SEM sample preparation, a series of steps were defined and followed by U. Täffner, MPI Stuttgart to prepare the cross section embedded samples.

The first step was to prepare a sandwich by gluing two dies of alumina onto both sides i.e. the top of the YSZ layer and the bottom of the alumina substrate, respectively. This provided a mechanical stability of the samples required for the subsequent processes. Then the samples were glued onto metal holder, which was used for regular polishing. The polishing of the samples was done on a hard synthetic cloth with a 3 μm diamond suspension by utilizing a

half-automatically machine [RotoPol-31/RotoForce-4, Struers]. Samples were then ground on a resin bonded diamond disc (20 μ m), followed by vibration polishing on a short napped, fiber cloth with a 10:1 solution of alumina (0.05 μ m) and (10%) NaOH. The last polishing was chosen to remove the pull-outs of the TBC layer discussed above and to avoid further pull-outs. The goal of the preparation was to achieve a uniform polished surface for quantitative measurements.

3.3.2 TEM Preparation

The requirements on the quality of the TEM specimens increase with the development of microscopy resolution. The specimens have to be very thin, which means transparent to the electrons and at the same time with high mechanical stability. Modifications on compositions or atomic structure during preparation have to be prevented.

Prior to TEM analysis in this work, specimens for plane-view and cross-sectional observations were prepared by common procedures described by *Strecker et al.* [93SSM and 86SNR] Figure 3.2 and Figure 3.3 represent a short summary of the specimen preparation techniques.

For the preparation of plane view sample: a small disc with diameter (about 3mm) corresponding to that of the electron microscope specimen holder was cut out (Fig. 3.2a) using an ultrasonic disc cutter (Gatan Ultrasonic Disc Cutter). After mechanical thinning the disc was ground from the substrate side down to 100 μ m, and then dimpled from substrate side down to 30-50 μ m (Fig. 3.2b). The minimum thickness depends on the brittleness of material. Finally, with low angle ion milling (Gatan, PIPS) a small hole was formed in the center of the sample (Fig. 3.2c). Specimen regions that are transparent to the electrons are usually found close to the edge of the hole.

The preparation of the cross-sectional samples enabled investigations of thin films on substrates and interface microstructure. A disk TBC-sample (Fig. 3.3a) with width about 2mm and height of about 10mm was cut and mechanically ground from the side of substrate down to 200 μ m. The thin slice was embedded into a polycrystalline alumina tube with diameter around 2mm and slit with a width of 150 to 200 μ m, fitting to the thickness of the slice. Then the tube was fixed in a cylinder which has an outer diameter of 3mm which corresponds to the diameter of the specimen holder of the microscope. The whole set-up (Fig. 3.3b) was glued together with a high viscosity epoxy (M-Bond AE 10/15) and heated to a temperature of 100°C for 1 to 2 hours. After hardening of the epoxy, the holder was cut into discs with thickness of ~500 μ m using a diamond wire (wire thickness about 170 μ m). The thickness of

the disc (Fig. 3.3c) was reduced to 100-200 μ m by grinding. Subsequently, the samples were dimpled (Gatan Dimpler Grinder, Modell 656, Gatan Inc. Pleasanton, CA, USA) from both sides using diamond paste with grain sizes of 6 μ m, 3 μ m and 1 μ m, respectively. The depth of the dimple was adjusted so that an optimum thickness was achieved (~30 μ m) at the center of the disc [93 SSM]. Ion beam thinning (Fig. 3.3d) with energy of ions (accelerating voltage) vary between 3.5 and 3.8kV and at a angle of 6° (Gatan Precision Ion Polishing System-PIPS, Gatan Inc. Pleasanton, CA, USA) was used for sample perforation.

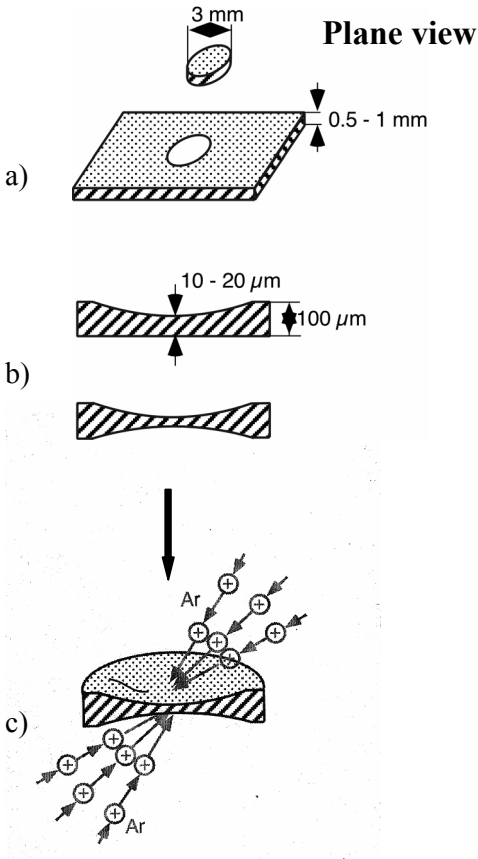


Fig. 3.2 TEM plane view sample preparation

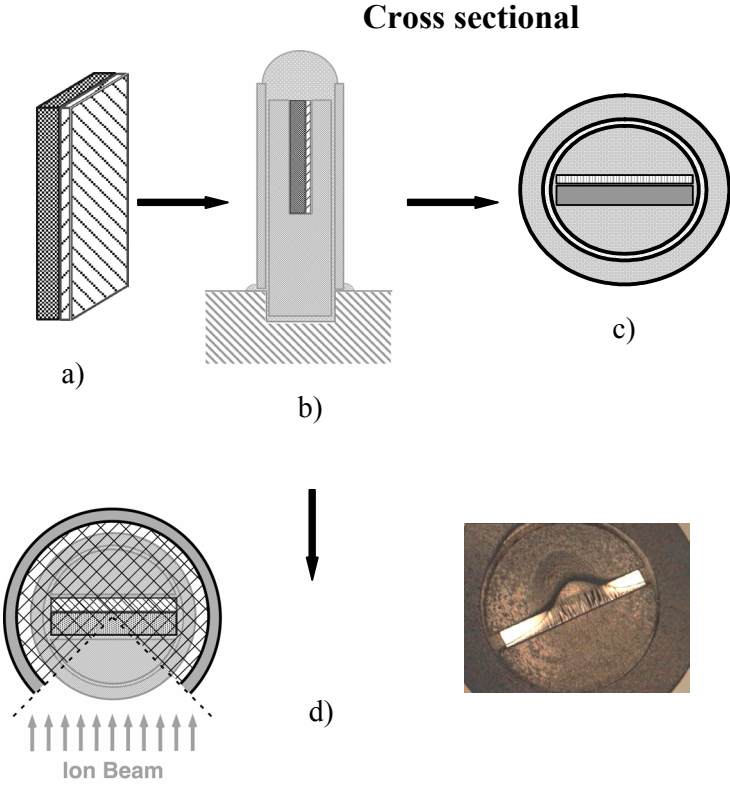


Fig. 3.3 TEM cross-sectional sample preparation

4. Experimental Methods for Materials Characterization

The required microstructural characterization on a wide range of length scale require the use of Scanning Electron Microscopy (SEM), Conventional Transmission Electron Microscopy (CTEM), Analytical Electron Microscopy (AEM), High-Resolution Transmission Electron Microscopy (HRTEM) and X-ray Diffractometry (XRD).

In this work CTEM (JEOL 2000 FX and Zeiss EM 912) were used to characterize the interface microstructure and orientation relationship between film and substrate in the interfacial region. HRTEM (JEM-ARM 1250) was most useful for studying atomic arrangements and for identifying possible defects at the interface.

The following chapter provides a brief outline of the basic principles of these techniques. Extended introductions to the Electron Microscopy Methods can be found in the bibliography: *Rühle and Wilkens* [96CaH], *Williams and Carter* [96WiC], and *Fultz and Howe* [01FuH].

Transmission Electron Microscopy

Elastic and inelastic scattering of electrons is the fundamental processes to all electron microscope technics. The interactions of the electrons with the specimen are used to create images, diffraction patterns or yields chemical information about the material. The electron scattering can be either elastic or inelastic. These terms describe scattering events which result in no loss of energy and some loss of energy, respectively. Figure 4.1 summarizes those signals generated when the electrons interact with a thin-specimen which are typically used in different types of electron microscopes.

Elastic scattering of electrons occurs at relatively low angles. These electrons give information about the microstructure with its defects and they are used in CTEM and HRTEM. AEM, based on inelastic interaction, provides chemical information about the samples using Electron Energy Loss Spectroscopy (EELS) and X- Ray Energy Dispersive Spectrometry (XEDS).

Other forms of scattering (large angle scattering) include backscattered and secondary scattered electrons. These are used for Scanning Electron Microscope (SEM) and give surface sensitive information such as topography and compositions.

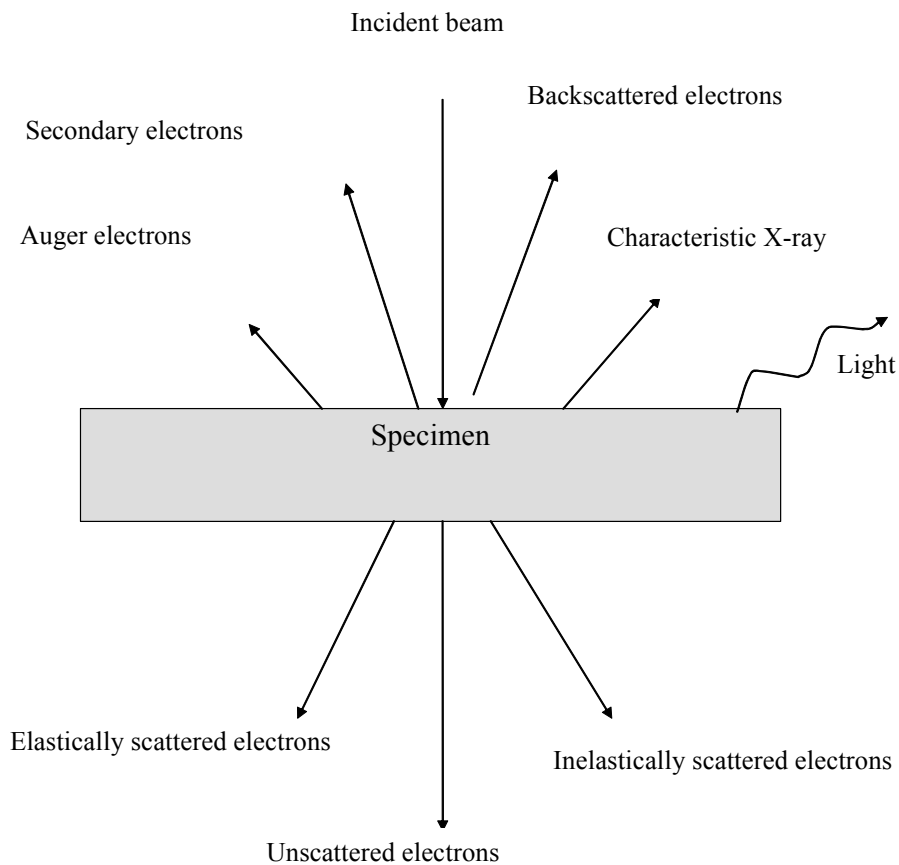


Fig. 4.1 Schematically summary of signals generated when a high-energy beam of electrons interacts with a thin specimen. Figure adapted from *Williams and Carter* [96 WiC].

4.1 Conventional TEM

A transmission electron microscope can be, similar to a light microscope, divided into three components according to their function: illumination system, the objective lens, and the imaging system. The role of the illumination (condenser) systems is to transfer the electrons from the source to the specimen. There are two different ways to use the illumination system: forming a parallel or a convergent beam. The first mode is used for TEM imaging and selected area diffraction (SAD), while the second one is used for imaging in a Scanning Transmission Electron Microscope (STEM), for microanalysis and microdiffraction.

The objective lens is the most important part of the TEM, since it produces the first image of the sample in its image plane and the diffraction pattern in its back focal plane. The resolution of the final image depends sensitively on the aberration of the objective lens and on the high voltage. Image or diffraction pattern can be selected with help of the intermediate lens, which

images either the back focal plane or the image plane of the objective lens. Further magnification on the screen is performed by subsequent projector lenses.

Figure 4.2 represents a ray diagram introducing the two basic operations of TEM imaging system: projecting the image and diffraction pattern onto the screen.

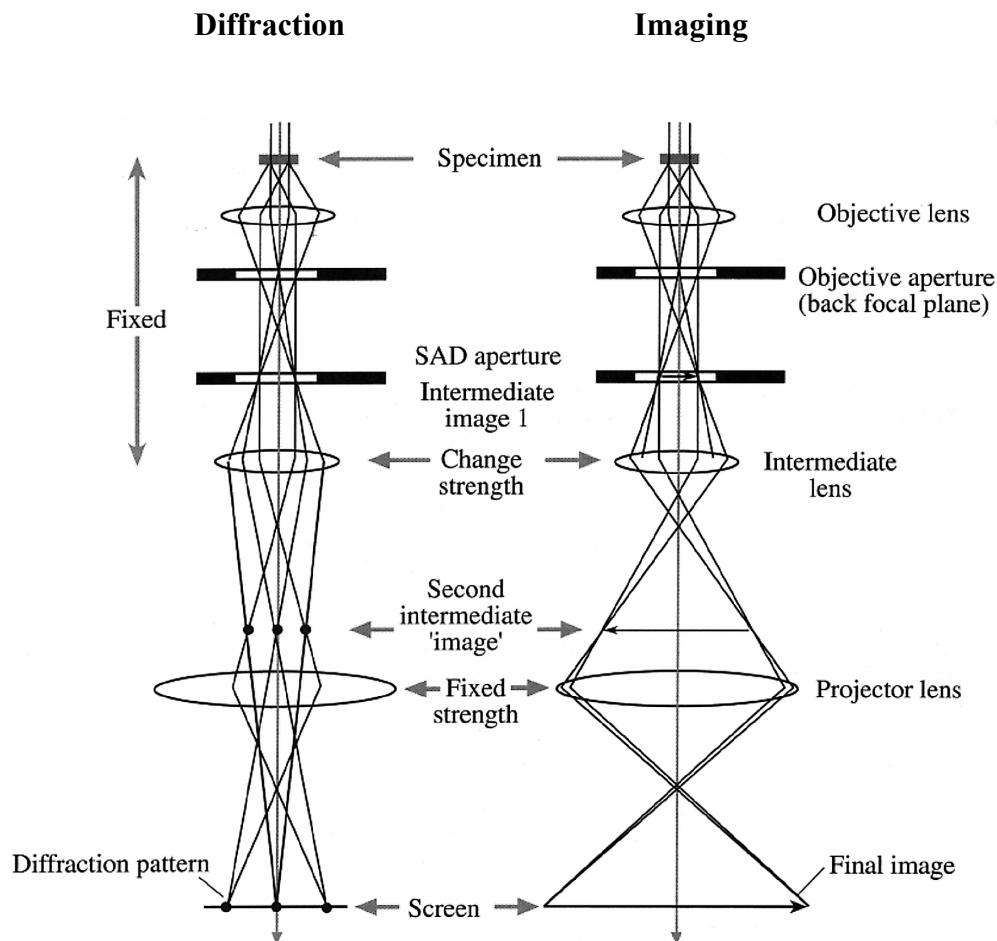


Fig. 4.2 Ray diagram presenting the two basic operation mode of TEM imaging: a) projecting the diffraction pattern on the viewing screen and b) projecting the image onto the screen. Diagram adapted from *Williams and Carter* [96 WiC].

Appropriate diaphragms have to be introduced in different planes of the TEM. Selected Area Diffraction (SAD) is used to choose a specific object region for obtaining a diffraction pattern with parallel illumination of the electron beam. SAD patterns can be formed by placing an intermediate aperture into the image plane of the objective lens.

TEM images can be formed, either using the central spot of the diffraction pattern, which contains the direct electrons, or using some of the scattered electrons. By positioning an

objective aperture in the back focal plane it is possible to choose the electrons that have been diffracted at the same angles. This defines two imaging modes illustrated in Figures 4.3a and 4.3b.

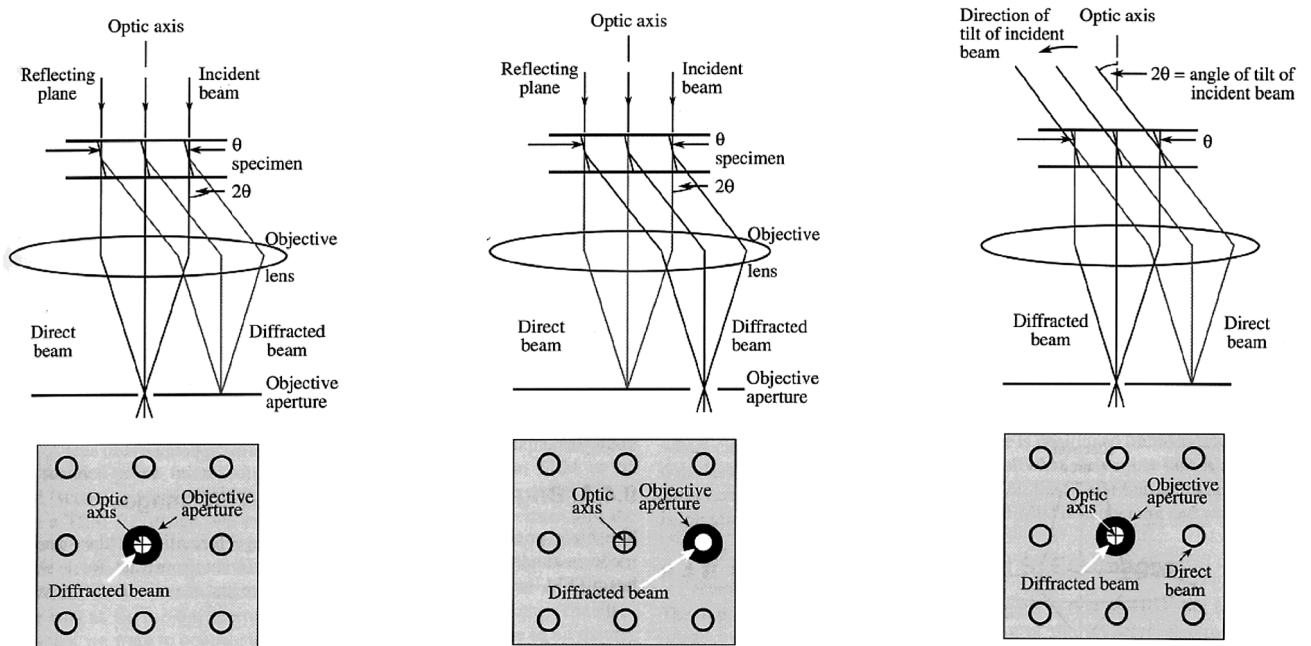


Fig. 4.3 Ray diagrams showing the formation of a) a BF image formed from the direct beam, b) a DF image formed with a specific off-axis scattered beam by displacing the objective aperture and c) a DF image where the incident beam is tilted so that the scattered beam remains on axis. Figure adapted from *Williams and Carter* [96 WiC]

A bright-field image (BF) is formed when only the direct beam is used for image formation. The objective aperture blocks all other beams to pass to the imaging system. A dark-field image (DF) is formed when the aperture is positioned to pass only some scattered electrons. The off-axis electrons are less accurately bent due to spherical aberrations of the objective lens which leads to a reduced image quality. To avoid this, the incident beam has to be tilted above the objective lens to keep the beam, which is used for imaging, close and parallel to the optic axis, as shown in Figure 4.3c.

The choice of the position and size of the aperture defines which electrons (directed or scattered electrons) contribute to the image. Thus BF and DF represent two forms for creating diffraction contrast in the image. Contribution to the image from diffraction contrast is primarily used for crystalline samples, where the scattering occurs for specific Bragg angles. Bragg diffraction is controlled by the crystal structure and orientation of the sample.

4.2 High Resolution TEM

Contrast in HRTEM images occurs due to the interference of electron waves scattered through a thin specimen. The patterns are formed from the differences of the phases between diffracted and forward-scattered electron waves (phase contrast). Therefore it is required to use an objective aperture large enough to include both the transmitted beam and at least one diffracted beam. High-resolution images are affected by focus, chromatic and spherical aberration of the objective lens, orientation, thickness and atom composition of the specimen. A quantitative interpretation of high-resolution images requires a quantitative comparison of experimental image with simulation images. The simulated images are generated in the following way: Firstly, a model of the atomistic structure is assumed, and then the HRTEM images are simulated by applying multi-slice method *Stadelmann* [87Sta] for the assumed film thickness. Then the influence of the lens aberration is included. By specific image processing techniques the experimental micrographs and the simulated images have to be compared. Usually, there is a good agreement of the images. The closest model of the specimen has to be modified. An iterative process results in the most likely model.

Since incident electron wave pass through a specimen with thickness less than 10nm the interaction with crystal potential change only the phase, but not the incident wave amplitude (phase object approximation = POA). Therefore the specimen transmission function in this case can be described as:

$$f(x,y) = \exp(-i\sigma\xi_p(x,y)), \quad (4.1)$$

where $\xi_p(x,y)$ is the two-dimensional projected potential and σ is the constant, giving an expression for the elastic interaction by incident electrons scattering from atoms in the sample. The final image is a convolution of the exit wave function at the bottom of the sample and the function describing the imaging system. This convolution can be transformed into a pure multiplication of the corresponding Fourier transform functions

$$Q(u,v) = F(\Psi(x,y)) \quad (4.2)$$

in the diffraction space. The influence of spherical aberration and defocusing can be described by multiplication of Fourier transformed wave function with the contrast transfer function (CTF).

$$\text{CTF}(u) = 2A(u) \sin\chi(u), \quad (4.3)$$

where $A(u)$ is the aperture function considering the effect of objective aperture in the microscope and $\chi(u)$ is the phase-distortion function. Two major terms contribute to $\chi(u)$:

$$\chi(u) = \pi\Delta f\lambda u^2 + \frac{1}{2} \pi C_s \lambda^3 u^4 \quad (4.4)$$

This function depends in a complex way on the spatial frequency u , the values of C_s (spherical aberration), λ (accelerating voltage), and Δf (defocus).

The CTF shows maximum values, when the phase distortion function is an odd valued multiple of $\pm\pi/2$. Zero contrast occurs when $\chi(u)$ is a multiple of $\pm\pi$. The presence of zero values in the CTF means that for this specific frequency u there is no signal in the image. The optimum value for the transfer function can be achieved by balancing the effect of spherical aberration against particular negative value of defocus. This value is known as the “*Scherzer defocus*”

$$\Delta f_{\text{sch}} \sim (C_s \lambda)^{1/2} \quad (4.5)$$

At this focus all the beam are transferred through the optical system with identical phase. The resolution of the microscope is also limited by the spatial coherence of the source and by the chromatic effects. This effect of instability in the lens current and in the high voltage can be included by multiplying the transfer function by envelope damp function.

4.3 Analytical Electron Microscopy

Analytical Electron Microscopy gives complementary information with high spatial resolution about the chemical and electronic structure of specimen. The analytical studies are based on the inelastic scattering of the electron beam, in which the incident electrons loose energy as they interact with inner shell electrons of the specimen. The corresponding ionization process is shown in Figure 4.4.

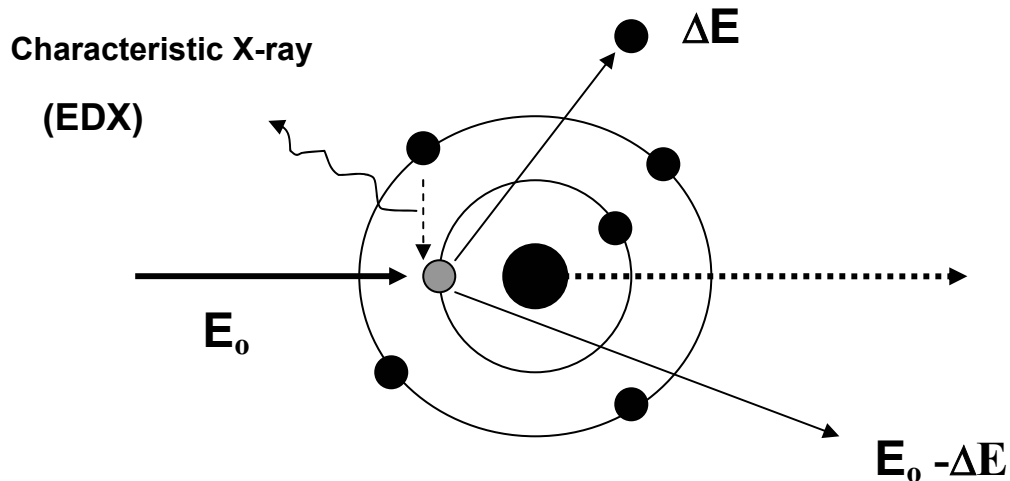


Fig. 4.4 Schematic representation of inelastic scattering of incident beam at electrons of inner shells. The beam electron loses energy. The characteristic X-ray and the energy losses which occur are used for analytical electron microscopy.

During the ionization process, a high-energy electron interacts with the inner-shell electron of an atom. To eject the tightly bonded electron, the transferred energy must be exact as the binding energy of the specific electron in the shell of atom. After the ionization the atom is left in an ionized and highly energetic state leaving a hole in the inner shell. The excited atom can return to its ground state by filling the hole with an electron from outer shells. This transition results in either the emission of characteristic X-rays or Auger electrons. From the intensity and wave length $\lambda_{(nm)} = 1.24/E_{(keV)}$ of the characteristic X-ray, one can obtain qualitative and quantitative information about the elements which are present in the sample.

The X-ray spectrometer used in an AEM is an X-ray energy-dispersive spectrometer (XEDS). The analysis of the characteristic X-ray is possible for $Z > 9$, whereas electron energy loss spectrometry (EELS) is most powerful for the light elements $Z < 9$.

In EELS measurements, the intensity of the inelastically scattered beam is measured directly as a function of energy loss ΔE . Owing to the inner-shell ionization the intensity increases steeply at a specific energy loss ΔE which corresponds to the energy difference between inner shell and the unoccupied state into which the electron has been excited. ΔE is characteristic for each atom species in the specimen. The intensity under the ionization edge can be used for quantitative elemental analyses for all elements in the sample. Details of the edge (fine structure) provide information about chemical (bonding) and structural (atomic arrangement) effects.

The spatial resolution of AEM has been established by experiments and Monte Carlo calculation. In bulk material the volume of interaction between high-energy electron beam and the specimen possesses a shape of a pear (Fig. 4.5). The width of the neck of the pear is determined by the shape of the beam, while the length of the neck depends on the energy of the electrons as well as on the thickness of the specimen. The diameter of the pear can exceed several microns (μm). Therefore studies with high spatial resolution can only be performed in thin foils. Those studies are accomplished in a CTEM and STEM with detectors for X-ray and EELS.

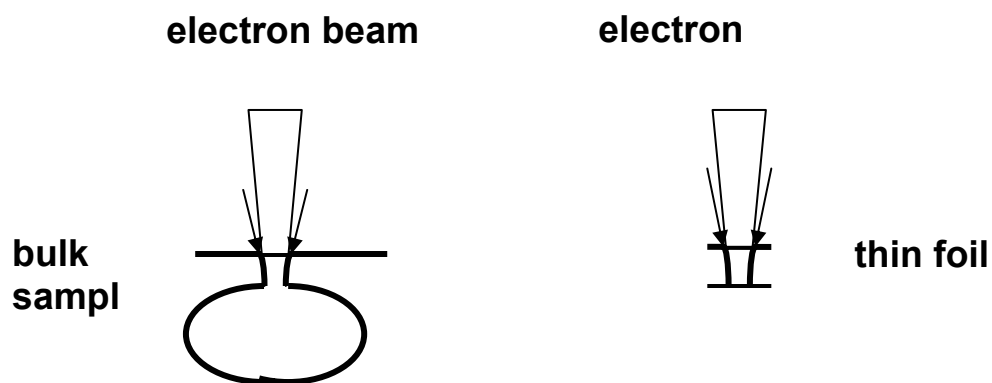


Fig. 4.5 Schematic diagram of the interaction volume as a function of incident beam diameter and the beam spreading caused by elastic scattering-of the beam within the sample. The beam spreading is affected by the beam energy, foil thickness and density of the specimen. Figure adapted from *Rühle and Wilkens* [96 CaH]

5. Results

This chapter presents the results of the systematic investigation on the microstructure of the TBC model systems with a focus on the interface microstructure between film and substrate. The studies were carried out for YSZ TBC deposited under (i) stationary and (ii) rotated conditions on (iii) bare and on (iv) seeded C-plane-sapphire substrates. Table 5.1 summarizes the studied model systems. The details of the deposition methods and conditions are described in Chapter 3.

Table 5.1: Summary of characterized model systems and abbreviation for the samples

SUBSTRATE	FILM	DEPOSITION CONDITIONS	SAMPLE
C-plane Sapphire	YSZ TBC	EB-PVD on Stationary Substrates	S-YSZ _S
C-plane Sapphire	YSZ TBC	EB-PVD on Rotating Substrates	S-YSZ _R
C-plane Sapphire	YSZ seeds	Precursor method	S-YSZ _P
Seeded Sapphire	YSZ TBC	EB-PVD on Rotating Substrates	SS-YSZ _R

The texture and morphology of the coatings were characterized by X-ray diffraction (XRD) and scanning electron microscopy (SEM). Transmission electron microscopy (TEM) observations were carried out to investigate the interface between the coating and sapphire substrate. SAD and BF/DF were used to determine the orientation relationship between substrate and film, Analytical TEM revealed the composition at the interface and HRTEM allowed observations of the interface microstructure at the atomic scale.

5.1 YSZ Grown on Stationary Substrates

The morphology of the film surface, under constant flux and vapour incidence (without substrate rotation during deposition) is shown in Figure 5.1. Most column tips of this coating have an elongated roof-top morphology with two flat faces. In addition, a smaller population of columns with triangular tips is randomly distributed across the surface.

Texture analysis of this coating (S-YSZ_S sample) is summarized in Figure 5.2. The θ - 2θ -scan contains predominantly the 200 peak, but also small fractions of the 002, 111 and 113/311 peaks. In ratio of the 200/002 peaks reveals that for most of the columns the c-axis of the t-YSZ lies parallel to the substrate surface. The 202 pole figure measurement of the texture is

given in Figure 5.2b. The data show that the YSZ coating has a $\langle 100 \rangle$ fibre texture with even highly random in-plane orientation. The triangular shape of the islands in Figure 5.1 suggests that the underlying grains are minor fraction of grains with $\langle 111 \rangle$ texture [01Ter].

SEM observations made on a fracture surface (Fig. 5.3a and 5.3b) reveal the columnar structure of the coating which has a thickness of $\sim 20\mu\text{m}$. The columnar grains grow perpendicular to the substrate surface and extend through the entire ceramic coating of thickness (t) with almost constant diameter (d). The columns are straight and densely packed. The column boundaries are relative difficult to distinguish owing the lack of well developed inter-columnar porosity. More information concerning the geometrical dimensions of the columns is available from cross-sectional TEM micrographs (Fig. 5.4). The TEM studies showed that this film consists of individual narrow and straight columns. The diameter of the columns ranges from ~ 50 to 100nm and is almost constant from bottom to top (Fig. 5.4)

Stress contours are visible in the sapphire at the interface (Fig. 5.4b). Each contour is located almost below every column (dark semicircles shown by arrow). They could be explained either by the difference in the thermal expansion coefficients between YSZ and sapphire (see Section 2.1) or by misfit dislocations caused by lattice-constant mismatch between the two materials.

From the two micrographs in Figure 5.4, it can also be seen that fine inter-columnar pores are formed during the growth process. They are aligned parallel to the growth direction and start to appear on average at a height of 300nm . The vertical distribution of pores along the columns is irregular and there is a wide dispersion in the distance between the pores, compared with the rotating samples (see below). The average spacing is around 30nm (Fig. 5.5a). Some of these pores are faceted. At higher magnification (Fig. 5.5b) it can be seen that the pores are mostly octahedral in shape and have diameters of around 10nm .

Although most of the columns grow in a direction perpendicular to the sapphire substrate, there are some grains which are slightly tilted off-axis. Two examples are marked by dashed line in Figure 5.6. The dark line-like contour of the micrograph corresponds to bend contours which indicate particular columns orientation where certain lattice planes are in Bragg condition. The sample was been tilted in such a way that the incident beam direction is slightly tilted out of the basal plane of the sapphire. The fact that the dark contour goes continuously and almost at the same height through all grains reflect the 100 texture of the film according to the X-ray results.

To determine the orientation relationship SAD patterns were recorded from an interfacial region which contains sapphire substrate as well as the YSZ film (Fig. 5.7a). Diffraction

patterns from sapphire and YSZ are present. The diffraction pattern is a superposition of the [100] zone axis of YSZ film and the $[10\bar{1}0]$ zone axis of the sapphire. A complete indexing of this diffraction pattern is shown in Figure 5.7b. The red and black circles in the schematic diagram represent reflections from YSZ grains and the sapphire substrate, respectively. The overlap of the diffraction patterns reveals that for the selected column an epitaxial relationship exists to the substrate with $(0001)_s \parallel (100)_{YSZ}$ and $[10\bar{1}0]_s \parallel [001]_{YSZ}$. The lateral streaks in planes parallel to the interface contain reflexes generated by grains which belong to the (100) out-of-plane orientation, but which are randomly oriented in the (0001) plane of the sapphire i.e. which are randomly rotated around the normal of the surface plane. The corresponding bright-field pattern including the SAD aperture is shown in Figure 5.7c. The position of the SAD aperture at the place where the DPs were recorded is also schematically illustrated on Figure 5.7d. The columns show different contrast which can be explained by the different orientation of the grains. A large portion of the grains appears dark which reveals that they undergo strong Bragg diffraction presumably due to their specific orientation relationship to the sapphire. The fact that the grains at the interface possess a $(0001)_s \parallel (100)_{YSZ}$ preferred orientation and some grains even a specific orientation $[10\bar{1}0]_s \parallel [001]_{YSZ}$ is observed for the first time in case of the EB-PVD TBC deposition.

In Figure 5.8a is shown a diffraction pattern which has been recorded with a large SAD aperture from a region $\sim 1\mu\text{m}$ away from the interface (see Fig. 5.7d). A schematic diagram of Figure 5.8a is shown in Figure 5.8b. The pattern resulting only from the YSZ layer contains three features: (i) as in Figure 5.7 a diffraction pattern from YSZ in [100] zone axis; (ii) stronger intensities of the 100 systematic row reflections produced by those grains with a $\langle 100 \rangle$ texture component; (iii) lateral streaks in planes parallel to the interface resulting from grains, which belong to the (100) out-of-plane orientation, but which are randomly rotated around the normal of the surface plane.

A diffraction patterns, taken at even larger distance to the interface parallel to the [100] zone axis of YSZ (Fig. 5.7d), show predominantly reflections generated by the grains with $\langle 100 \rangle$ texture (Fig. 5.9a). Some of the spots are radially split which is probably induced a small rotation of the crystals around the [100] zone axis.

Dark-field imaging was used to determine the grains which are well orientated with respect to the substrate. Figure 5.10 shows a representative bright-field image and the corresponding dark-field image which were taken with the reflections marked on Figure 5.7a. The incident beam is parallel to the $[10\bar{1}0]$ zone axis of sapphire. Using the reflections parallel to the interface plane, those columns which appear bright possess a specific in-plane orientation

relationship to the sapphire, namely: $[10\bar{1}0]_s \parallel [001]_{\text{YSZ}}$. There are some columns at the interface which appears to be not extended through whole coating length. This is an effect of a bending of the columns in the plane of the sample (vertical direction in the micrograph).

Figure 5.11 presents an example of another series of diffraction patterns recorded in different regions of a stationary sample: directly at the interface and at a distance of 1 to $2\mu\text{m}$ from the interface respectively. The position of the SAD aperture from the places where the diffraction patterns were recorded is similar to that which is schematically shown in Figure 5.7d. This particular set of diffraction patterns was recorded when the incident beam was parallel to the $[2\bar{1}\bar{1}0]$ zone axis of sapphire. To record these pattern, the TEM sample was oriented in a way that the beam was parallel to the $[10\bar{1}0]$ zone axis of sapphire, which is perpendicular to the $[0001]$ zone axis. Since the $[0001]$ zone axis is perpendicular to the interface plane (0001) plane, the diffraction pattern from the $[10\bar{1}0]$ zone axis of sapphire contains the reflections from the interface. This guaranteed that the sample was tilted about -30° around the $[0001]$ zone axis of the sapphire in direction along the interface. The diffraction pattern from the interfacial region (Fig. 5.11a) presents both reflections from the sapphire and from the YSZ. Also here, as in Figure 5.7a the overlap of the DPs reveals that these particular grains possess an epitaxial relationship to the substrate for out-of-plane and in-plane orientation. The DPs recorded with the same size SAD aperture from regions at a distance of about $\sim 1\mu\text{m}$, then $\sim 2\mu\text{m}$, and $\sim 3\mu\text{m}$ from the interface (Fig. 5.11b-d) show almost the same features as the DPs observed without tilting the sample. The diffraction pattern recorded from a region $\sim 1\mu\text{m}$ from the interface shows that the selected grains are oriented parallel to the $[100]$ zone axis of YSZ (in-plane orientation) with additional reflections from those grains which are randomly rotated around the $[100]$ zone axis of YSZ. With increasing distance from the substrate the specimen became very thin and bends elastically, i.e. the lattice planes physically rotate. The effect of this rotation can be seen in the circles split of the reflection. Only the reflections corresponding to the $\langle 100 \rangle$ texture component remain dominant.

For both cases with and without tilting the sample a preferred out-of-plane orientation exists, where some of the columns possess in addition an in-plane orientation.

The HRTEM micrograph presented in Figure 5.12 shows for the first time image of the interfacial region between YSZ TBC and sapphire substrate on the atomic level. The image is recorded from the same region as this one presented in Figure 5.10. The incident beam is parallel to the $[10\bar{1}0]_s$. The $(001)_{\text{YSZ}}$ and $\{1210\}_s$ lattice fringes, parallel to the interface are clearly resolved. However, the near-interface region shows inhomogeneous contrast. This indicates that the interface is rough and contains many steps which may be a result of the

surface preparation prior to the YSZ deposition. Third phases (reaction layer) are not observed as in agreement with the prediction from the actual phase diagram [03FaA].

5.2 YSZ Grown on Rotating Substrates

SEM image presented in Figure 5.13a shows the surface morphology of YSZ deposited on rotating sapphire substrates by EB-PVD (S-YSZ_R sample). The axis of substrate rotation is parallel to the horizontal direction in the micrographs (J. Cho, private communication). Figure 5.13b shows details of the morphology of the column tip. The column top of YSZ TBC consists of four triangular faces arranged regularly in a pyramidal shape. Neighbouring faces on a column tip are separated by sharp ridges which are oriented parallel and orthogonal to the axis of rotation. The faces contain steps which are oriented parallel to the base of the pyramid. Open gaps (inter-columnar pores) are visible between the columnar grains.

The texture of the coating was analyzed by XRD. Representative diffraction diagrams are shown in Figure 5.14a and Figure 5.14b. The θ - 2θ scan indicates a strong out-of-plane texture with [100] axis. Figure 5.14b represents the 202 pole figure, containing a four-fold symmetry which indicates preferred in-plane orientation wherein one of the $\langle 100 \rangle$ directions is parallel to the rotation axis.

The YSZ coating grown on rotated sapphire substrate was fractured perpendicular to the interface. SEM micrographs are shown in Figure 5.15a and Figure 5.15b, respectively. The total thickness of the coating was about 20 μm . The grains are highly columnar with prismatic shape and oriented along the growth direction. The columns seem to be less densely packed than those processed under stationary conditions (c.f. Fig. 5.3). Larger separations exist between columns. Higher resolution images (Fig. 5.15b) reveal a porous structure. The polished cross-sectional micrograph from the near-tip region of the sample (Fig. 5.16) reveals the inter-columnar gaps (as shown in Fig. 5.13) and presence of closed inter-columnar porosity. The mechanism of gap formation suggested by *Terry and Levi* [01Ter] is an interaction between the surface roughness and the vapor. The rotation of the substrate emphasizes shadowing effects. The pattern of vapor incidence and the topography of rotated sample are analogous to the manner in which valleys on earth are lit by the sun. The lowest points of the valleys are shadowed by the surrounding peaks during the sunrise and sunset periods of vapor incidence which initiates gap formation. The shadowing responsible for the inter-columnar gaps is enhanced by the curved profile of the columnar tips (see Fig. 5.16) which makes it more difficult for the vapor flux to reach the bottom between column tips.

Closed porosity can also be formed directly from shadowing. The features involved in forming closed porosity must have a symmetric geometry with respect to the pattern of vapor incidence and must be small enough such that generated pores are closed again with each revolution. These pores are generated by shadowing at small length scales when crystallographic features on the column tips interact with the line-of-sight vapor. For the YSZ deposited on sapphire single crystals where the columnar grains during the initial stage are very small (~50nm), the profile of neighboring tips generates closed porosity. In this situation, as is suggested by *Terry* [01Ter], neighboring columns are separated by an array of periodically spaced voids rather than open gabs (see Fig. 5.24. below).

The orientation relationship of YSZ grains with respect to the (0001) sapphire substrate were investigated with CTEM (imaging and diffraction studies). Both specimens for plan-view and cross-sectional observation were prepared as described in Chapter 3.

Figure 5.17 shows a low magnification plan-view bright field TEM micrograph of the YSZ film grown on the rotated sapphire substrate. The transparent area contains the interfacial region. The brighter areas correspond to the underlying substrate. Bend contours reveal that the sample is strongly curved. The darker, fine grained area contains the bottom region of the YSZ layer. Since the plane view sample was thinning (see Section 3.3.2) first from the side of sapphire until the substrate is missing and then the thinning was continuing from the side of YSZ layer until a hole is produced, there are areas near the hole where either sapphire or YSZ alone can be observed. Figure 5.17b shows schematically the cross-sectional of the plane-view sample. Area 1 represents the case where in the plane-view sample only sapphire can be seen (pointed in Fig. 5.17a), and area 2 which contains only the YSZ layer. At higher magnification (Fig. 5.18) the polycrystalline nature of the YSZ film can be clearly seen. The incident electron beam is parallel to the $[0001]_s$ direction. Due to bending of the sample some parts of the same are not perfectly aligned along the zone axis, resulting in the observed contrast change. The grain boundaries are visible as fine, white lines. A BF micrograph at higher magnification (Fig. 5.19), taken from the same specimen but from a different area clearly shows the presents of porosity.

A selected area diffraction (SAD) pattern (Fig. 5.20a) reveals the orientation of the YSZ grains with respect to the sapphire substrate. The rings around the central beam are from YSZ film in a $[001]$ zone axis. In addition, reflections with 3-fold symmetry around the $\{200\}$ type YSZ reflections are visible (indicated by arrow in Fig. 5.20a). These spots are $\{1\bar{2}10\}$ reflections originating from $[0001]_s$ zone axis of underlying sapphire. A diffraction pattern generated from free standing YSZ film (without the substrate) can be seen in Figure 5.20b.

The stronger reflections on the $\{200\}$ type circles possess a 6-fold rotation symmetry, which may correspond to 3 different orientations of YSZ grains. The overlap of YSZ on the sapphire reflection (Fig. 5.20a) reveals that there is a strong preferred orientation relationship between film and substrate namely $[0001]_s \parallel [100]_{\text{YSZ}}$, with multiple variants which occurs from the texture. The fine spots at the same circles visible in both Figure 5.20a and Figure 5.20b are generated from those grains which possess (100) out-of-plane orientation but are randomly oriented in the plane of sapphire.

Figure 5.21a illustrates schematically the interpretation of the plan-view diffraction pattern. Reflections from the substrate and from YSZ grains are included. There are three equivalent variants each rotated 120° with respect to each other around the $[001]_{\text{YSZ}}$ axis. Figure 5.21b, adapted from *Cain and Lang* [94CaL] (difference between cubic and tetragonal lattice parameters $< 2\%$) shows the 3 possible variants on in-plane orientation of tetragonal YSZ on c-plane sapphire. This is caused by the superposition of the tetragonal unit cell and the threefold rotational symmetry of sapphire. The $[100]$ zone axis of each YSZ cube is exactly parallel to the one of $[1\bar{2}10]_s$ zone axis.

Dark field imaging was used to identify the spatial distribution of well oriented grains which are counted among these 3 variants. Systematical DF imaging measurements with each of $\{200\}$ and $\{400\}$ pronounced reflections were carried out. A representative DF micrograph is shown in Figure 5.22. The DF-images were taken with a small objective aperture, which detects an angle range of 5° degrees of the first inner diffraction ring and 3° degrees of the second diffraction ring. Bright areas are generated by grains which in an exact 2-beam imaging condition are tilted in a way that Bragg's law is fulfilled. The film structure shows irregularly shaped grains. Larger grains may be caused by an assembly of several grains which may be separated by each other by small angle grain boundaries. The grain size varied from 25 to 200nm

The spatial distribution of each of the 3 variants of in-plane orientation is presented in Figures 5.23a, 5.23b and 5.23c, respectively. The contribution of all well oriented grains was summed and calculated with help of image processing program (PV-WAVE). The result is presented in Figure 5.23d, which is an overlap of Figures 5.23a, 5.23b, and 5.23c. It was found that 83% of the grains near the interface have a special orientation relationship to the sapphire. The white areas in Figure 5.23d correspond to that amount of grains (17%) which belong to the (100) out-of-plane distribution but are randomly orientated in the plane of sapphire.

A more detailed analysis of the columns and their orientation relationship to the substrate at the interface was performed by cross-sectional TEM investigations. Figure 5.24 shows a

micrograph with view in the direction perpendicular to the axis of substrate rotation. The film consists of individual columns, which are oriented perpendicular to the interface. The diameter of the columns in the interfacial region (~500nm from the interface) varied from 50nm to 100nm and increase with the distance from the interface. The stress contours in the sapphire at the interface (dark contrast located almost every column) are similar to that observed in S-YSZ_S (see Fig. 5.4b). They can be explained either due to difference in the coefficients of thermal expansion between YSZ and sapphire or due to lattice- constant mismatch between the two materials.

A BF TEM cross-sectional micrograph (Fig. 5.25), taken in direction parallel to the axis of substrate rotation, shows that in this view direction the stress contours are significantly less pronounced. The column structure is similar to that observed in Figure 5.24.

In both TEM micrographs (Fig. 5.24 and Fig. 5.25) closed inter-columnar pores which were observed in Figure 5.16 now are clearly noted. The nano-scale voids at the crystal boundary (shown by arrow) are highly aligned in planes parallel to the substrate surface. The measured pore spacing is ~35nm. The distance between the periodic lines corresponds to the amount of material deposited in one revolution, except for the initial layer. *Terry and Levi* [01Ter] explained this microstructure feature with the need for a significant roughness on the surface before shadowing processes become dominant.

Figure 5.26a represents a SAD pattern recorded from the YSZ / sapphire interfacial region.

The corresponding bright field image with the size of the diffraction aperture is shown in Figure 5.26b. The incident beam is parallel to the $[10\bar{1}0]_S$ zone axis. The result of the interpretation of the diffraction pattern is shown in Figure 5.26c. In this schematic diagram the red and black circles represent reflection from YSZ grains and sapphire substrate, respectively. As indicated, there is a preferred orientation relationship between film and substrate: out of-plane orientation with $(0001)_S \parallel (100)_{YSZ}$ and for many grains additional in-plane orientation with $[10\bar{1}0]_S \parallel [001]_{YSZ}$. As expected, this specific orientation relationship is identical to this observed in the plane view TEM S-YSZ_R sample (Fig. 5.20) and for the interfacial region in S-YSZ_S sample (Fig. 5.7).

Diffraction patterns from YSZ film, which have been obtained from regions at distance of ~1 μ m, and ~2.5 μ m, respect to the interface, are shown in Figures 5.27a and 5.27c, respectively. SAD pattern in Figure 5.27a shows the same features as those obtained for the S-YSZ_S sample from the same film region (Fig. 5.8). Figure 5.27a shows the $[100]$ zone axis diffraction pattern from YSZ with strong intensity of reflections which results from a $\langle 100 \rangle$

texture. SAD pattern, taken from an area $\sim 2.5\mu\text{m}$ away from the interface shows that all columns contributing to this image (see Fig. 5.27d) are oriented in $[100]$ zone axis.

The dark field TEM image in Figure 5.28a is formed by using the selected spots pointed in Figure 5.26a. To get strong diffraction contrast the sample was tilted to two-beam conditions, in which only the direct beam and the diffracted beam are the strong spots in the pattern. The view direction is parallel to the rotation axis, i.e. the sample was oriented in a way that the incident electron beam is parallel to $[1\bar{2}10]_s$ which is perpendicular to the $[0001]_s$. All grains which appear bright in DF image are grains where the crystal planes are at the Bragg condition. Thus indicate that these grains possess a specific orientation relationship to the substrate: $[1\bar{2}10]_s \parallel [001]_{\text{YSZ}}$. This corresponds to variant 2 at the diagram in Figure 5.21b. To compare the results with those for plan-view sample the specimen was tilted about -30° around the $[0001]_s$ zone axis in direction along the interface (Fig. 5.28b). In the $[\bar{2}\bar{1}10]_s$ view direction the micrographs shows relative large number of grains which appear bright. These well orientated grains possess a specific orientation relationship to the sapphire: $[\bar{2}\bar{1}10]_s \parallel [001]_{\text{YSZ}}$ corresponding to variant 1 in Figure 5.21b. The DF micrograph in Figure 5.28c represents the case when the sample was tilted parallel to the interface in direction $+30^\circ$ around the $[0001]_s$ which means $+30^\circ$ from $[1\bar{2}10]_s$ (see the schematic illustration below the Fig. 5.28). The DF image in $[11\bar{2}0]_s$ view direction reveals also a large number of grains which are well oriented to the substrate. They possess a specific orientation relationship to the sapphire: $[11\bar{2}0]_s \parallel [001]_{\text{YSZ}}$ which corresponds to variant 3 in Figure 5.21b

The analysis of the SAD patterns (Fig. 5.20) and the DF images (Fig. 5.23) from the plane-view sample are accompanied by the SAD patterns and DF images analysis of the cross-sectional sample (Fig. 5.26 and Fig. 5.28). As indicated by the these results: the YSZ grains in S-YSZ_R sample possess a preferred orientation relationship to the sapphire with $(0001)_s \parallel (100)_{\text{YSZ}}$ out-of-plane orientation and for many grains additional in-plane orientation with 3 variants: $[\bar{2}\bar{1}10]_s \parallel [001]_{\text{YSZ}}$ (variant 1), $[1\bar{2}10]_s \parallel [001]_{\text{YSZ}}$ (variant 2), and $[11\bar{2}0]_s \parallel [001]_{\text{YSZ}}$ (variant 3).

As can be seen in all three cases, often agglomerates of columns have the same orientation. Those agglomerates of columns may be separated by a small angle boundary.

HRTEM micrographs from the interfacial region between the YSZ film and sapphire substrate in direction perpendicular and parallel to the rotation axis are shown in Figures 5.29a and 5.29b, respectively. The incident electron beam is parallel to $[10\bar{1}0]_s$ and $[1\bar{2}10]_s$ zone axis, respectively. On the atomic level, the YSZ/sapphire interface is quite flat and abrupt. Some

steps are visible. Most likely, the steps are formed during the surface preparation before deposition. No amorphous phase was detected. The $(100)_{\text{YSZ}}$ and $\{1\bar{2}10\}_s$ in Figure 5.29a, $(100)_{\text{YSZ}}$ and $\{10\bar{1}0\}_s$ in Figure 5.29b, lattice fringes which run to the interface are clearly resolved. HRTEM images give evidence that these particular grains possess a specific orientation relationship, which corresponds to variant 2 (see Fig. 5.21b). To observe the other two variants (variant 1 and variant 3) the sample was tilted $+30^\circ$ and -30° from $[10\bar{1}0]_s$ around the $[0001]_s$ in a way described above (see Fig. 5.28). The results can be seen in Figures 5.30a and 5.30b, respectively. The micrographs confirm the specific orientation relationship to the sapphire for those grains.

Figure 5.31 shows an interface detail with a boundary of two YSZ grains. The vertical lattice fringes of the left grain are not clearly resolved, because it is not orientated exactly parallel to the beam direction. These kinds of grains are part of the distribution with a preferred out-of-plane orientation but do not belong to the one of the three main variants (called randomly oriented in the plane of sapphire).

5.3 YSZ Seed Layers on Sapphire Substrates (YSZ thin films produced via liquid precursor method)

As it described in Chapter 3, liquid precursors can be used to form ceramic thin films. For the goals of this work, precursor films were deposited on single crystal (0001) sapphire substrates by spin-coating premixed aqueous solutions of zirconium acetate and yttrium nitrate. The ceramic films were formed by the pyrolysis of the precursor film. During heat treatment at 1100°C and 1600°C the precursor films were converted into a dense ceramic thin film or into isolated islands of YSZ grains, respectively.

The specimens were first investigated by Atomic Force Microscope (AFM). Figure 5.32 shows an AFM image of the YSZ microstructure developed on the (0001) sapphire as a function of temperature for a heat treatment of 1h. As can be seen (Fig. 5.32a) after the 1100°C treatment the film consists of network of crystallites with a size of $\sim 50\text{nm}$. The initial film thickness is about 30nm (height scale below the images). XRD measurements performed at UCSB showed a mixed $[100]/[111]$ texture. After the treatment at 1600° , the grain size increased rapidly and the film began to break up into islands. At 1600°C the substrate was covered with only a single layer of grains as it shown in AFM micrographs (Fig. 5.32b). The grains size is varied from $0.3\mu\text{m}$ to $1\mu\text{m}$ with average height of $\sim 400\text{nm}$. Moreover, during

the break-up process, XRD patterns showed evidence of well developed [100] out-of-plane orientation.

TEM BF micrograph of a sample heated to 1100°C for 1h is presented in Figure 5.33a. The film thickness is approximately 30nm and the grain size is between 50nm and 70nm. The cross-sectional TEM observations confirm the measurements obtained from AFM. The different image contrast of the grains in a polycrystalline film reveals that there are no specific orientation to the sapphire (they are randomly orientated in the plane of substrate). An associated SAD pattern of the sapphire substrate and the YSZ grains shown in Figure 5.33b confirms the polycrystalline structure of the film. The strong intensity reflections are from the sapphire substrate in a $[1210]_s$ zone axis. The rings around the central beam are from YSZ grains and correspond to [100] and [111] zone axes. This out-of plane orientation accompanied the XRD results which reveal mixed [100]/[111] texture. Figure 5.33c shows the corresponding dark-field image. With some exceptions, the YSZ grains appear dark under the same diffraction conditions as the substrate, offering further evidence of its polycrystalline nature. In addition, the bright contrast fringes observed in the sapphire at the interface suggests that there may be strain present in interfacial region.

Figure 5.34 shows the cross-sectional micrographs of a sample heat-treatment at 1600°C for 1h. Two types of islands were distinguished. The first type (Fig. 5.34a and 5.34c) exhibited a flat plate-like morphology and the other ones (Fig. 5.34e) a hill-like shape. The corresponding diffraction patterns show that the grains reveal a preferred orientation to the underlying substrate. However, some of the islands (Fig. 5.34a and 5.34b) are perfectly oriented to the substrate while others are slightly tilted onto the sapphire (Fig. 5.34c and 5.34d).

5.4 YSZ Grown on Rotating Seeded Substrates

To examine whether the isolated, preferably oriented grains produced by precursor method can effectively seed the oriented growth of thicker films, two thin films were compared. Both films were prepared by the precursor technique described in previous paragraph and deposited on (0001) sapphire substrates. The first was heat treatment at 1100°C for 1h and the second one at 1600°C for 1h. As a second step, the substrate containing the seeds is coated by EB-PVD with a $\sim 22\mu\text{m}$ thick film of the same material as the seeds ($\text{ZrO}_2 + 7\text{wt}\% \text{Y}_2\text{O}_3$). For both samples (SS#11 and SS#16) the deposition rate is faster compared with that which was

used for the deposition of the S-YSZ_R samples (see Tab. 3.1). The remnant grains are expected to act as a seeds for the growth of a continuous film of high orientation.

Representative SEM images of the top surface of the two EB-PVD TBC coatings (deposited onto small-seeds-layer substrate: SS#11, and onto large-seeds-layer substrate: SS#16) are shown in Figure 5.35. Well separated columnar structures are found for both samples. The tips of the columns have a shape of quadrangular pyramids but without the strong four-fold symmetry as was observed for S-YSZ_R sample (Fig. 5.13). All bonding surfaces are covered by crystallographic growth steps. The tips morphology in Figure 35.5a exhibits greater roughness and reduced axial symmetry compare to one presented in Figure 35.5b.

In-plane texture orientation was determined by XRD measurements. 2θ scans show [111]/[100] texture for the YSZ coating deposited on the sapphire substrate with the small seeds and [100] texture for the coating deposited on a substrate with larger seeds. In Figures 5.35c and 5.35d the fourfold symmetry is visible for both coatings. However, the texture is less developed in case of small-seeds-layer-substrate (Fig. 5.35c).

TEM cross-sectional investigations (Fig. 5.36a and 5.36b) show the microstructure of the coatings. In Figure 5.36a the substrate is covered with a continuously layer of seeds with a thickness of about ~30nm. The substrate in Figure 5.36b posses a layer of single grains with size of about ~1 μ m and in between them a buds-like with a diameter of about ~50nm.

The columnar structure is similar in both cases. The columns are not as regular and parallels over their length as was observed in case of S-YSZ_R sample. A possible explanation is the faster deposition rate which was used compared to S-YSZ_R deposition. The different image contrast and additionally dark-field study reveals that there is no preferred orientation relationship between the columns and the seeds. In addition the micrographs reveal the absence of highly aligned inter-columnar porosity, typical for S-YSZ_R samples.

BF TEM micrograph of a SS-YSZ_R sample deposited at the same rate as S-YSZ_R (see Tab. 3.1 sample SS#14) is shown in Figure 5.37. This sample is a god example to compare the YSZ deposition on a bare sapphire with that deposited on seed sapphire substrates. The YSZ coating reveals column structure similar to this observed in S-YSZ_R sample. In the area between two neighbor seeds the SS-YSZ_R coating possesses the same features as those observed in S-YSZ_R samples: individual, straight columns, oriented perpendicular to the interface with highly aligned inter-columnar porosity. The coating on the top of seeds possesses a bunch-like structure. It seems as if the coating follows the geometry of the particular seed (Fig. 5.37b). The spacing between the periodic lines (pores) is ~35nm, which corresponds to the amount of material deposited in one revolution.

A representative DF TEM image is shown in Figure 5.37c. As can be seen the columns growing directly on the sapphire substrate appear bright. For these columns the Bragg conditions is fulfilled which means that they possess a preferred orientation relationship to the substrate as in the case of S-YSZ_R sample (Fig. 5.28). The seeds which satisfy the Bragg condition appear bright, which reveal that they are well oriented to the substrate. This fact accompanied the results presented in Figure 5.34. However, the columns on the top of the seeds reveal that there is no preferred orientation relationship between seeds and YSZ (pointed by arrow in Fig. 5.37c). A very thin, amorphous layer can be seen on the surfaces between seeds and YSZ film. The chemical analysis of possible Si contamination (probably from the furnace during the heat treatment of the seeds) is very difficult, since in the EDX signal the K-peak of Si and the L-peak of Y and Zr convolute into one peak due to the low energy resolution of the EDX. Testing the quantitative analysis with nominal pure YSZ showed that even for this material unrealistic high values of Si content were measured.

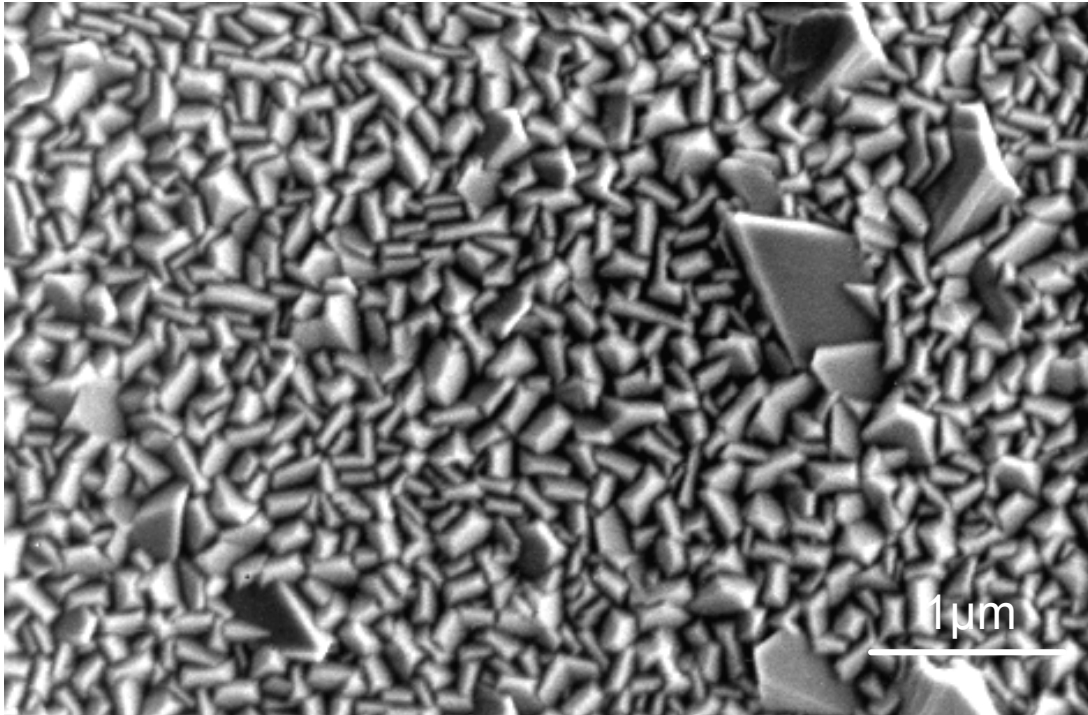


Fig. 5.1 Plane view SEM image of YSZ TBC deposited under stationary condition. The image shows roof- top surface with additionally small population of columns with triangular tips.

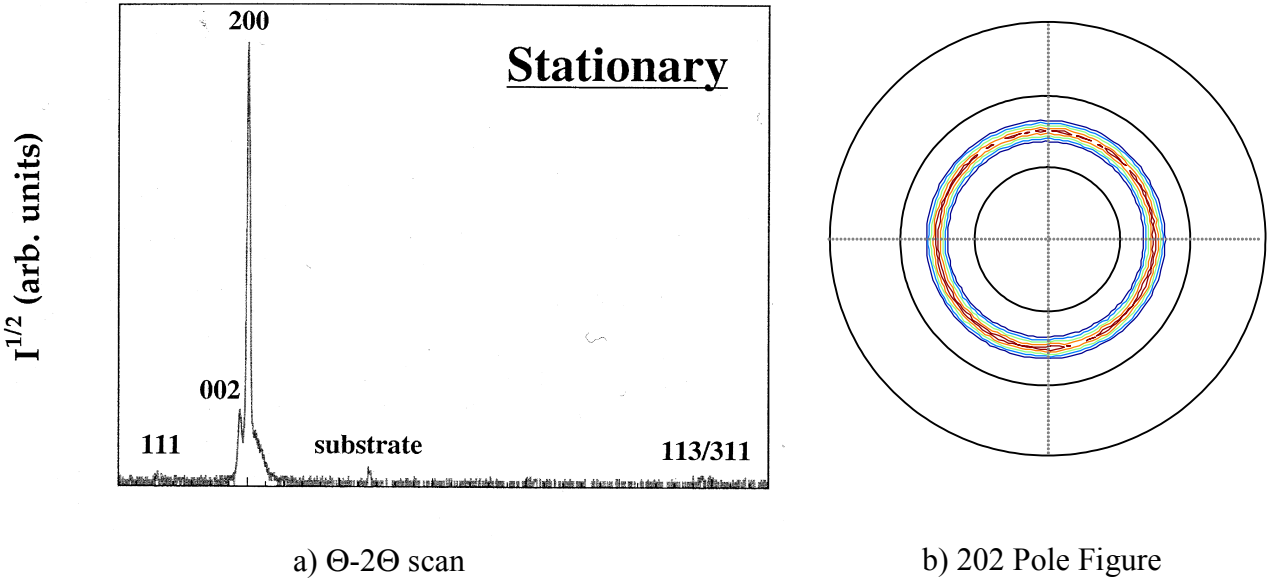


Fig. 5.2 a) Θ - 2Θ scan and b) 202 pole figure of a YSZ deposited under stationary, normal incidence. (XRD by J.Cho, UCSB)

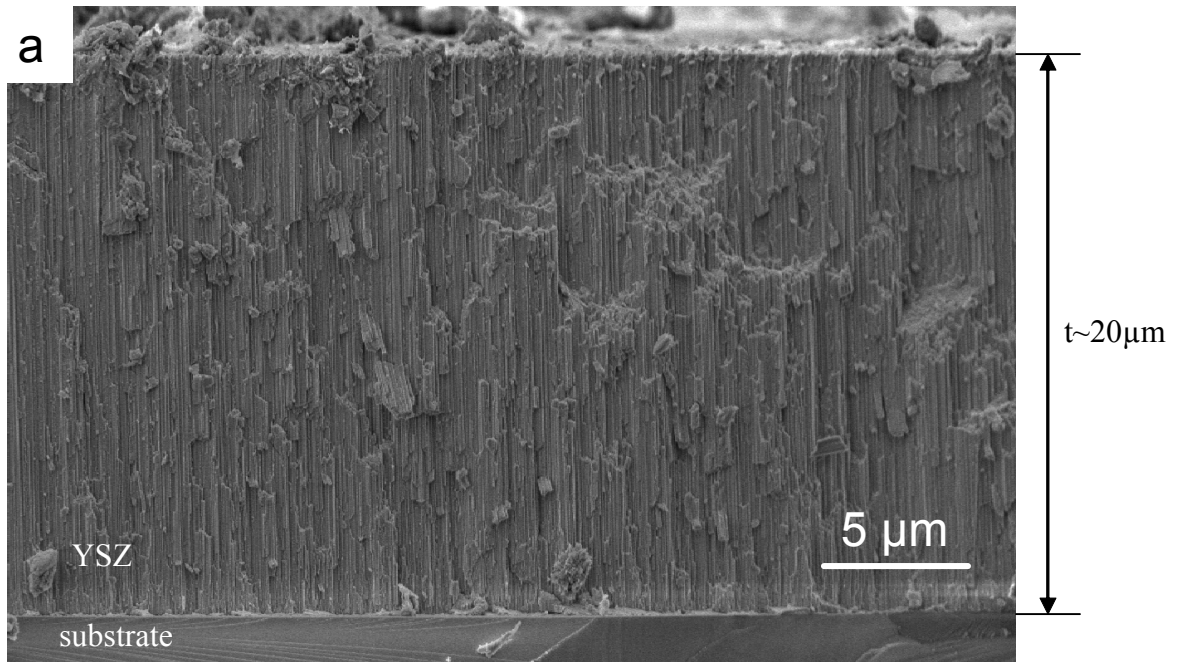


Fig. 5.3 Fracture cross sectional of YSZ grown on stationary substrate: a) at low magnification and b) higher magnification of the columns.

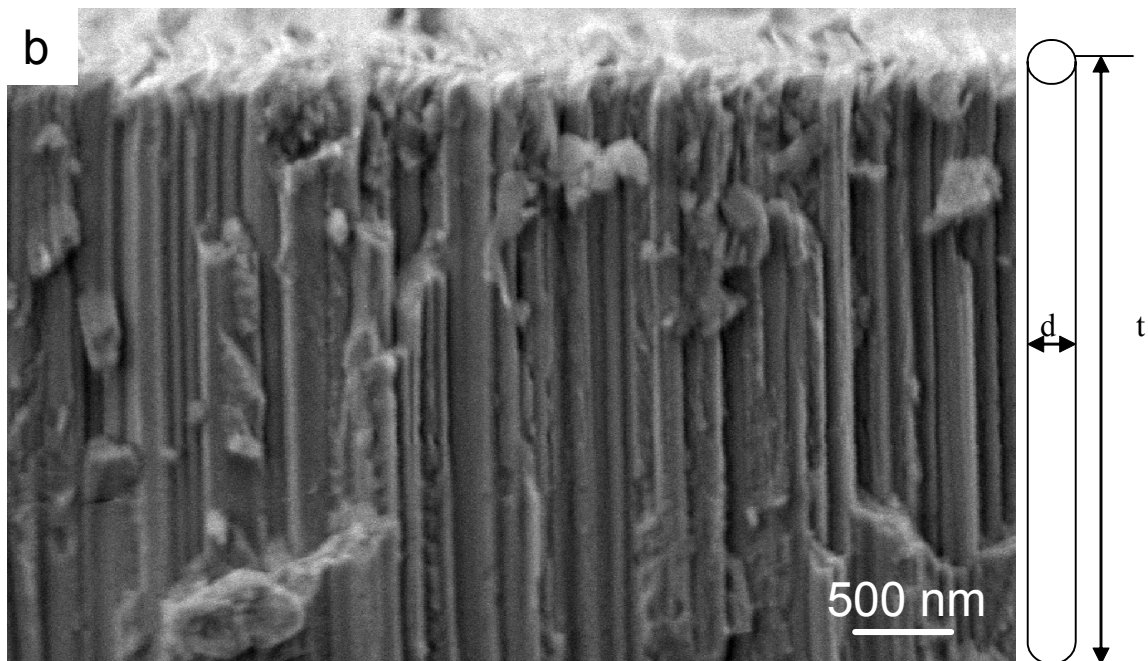
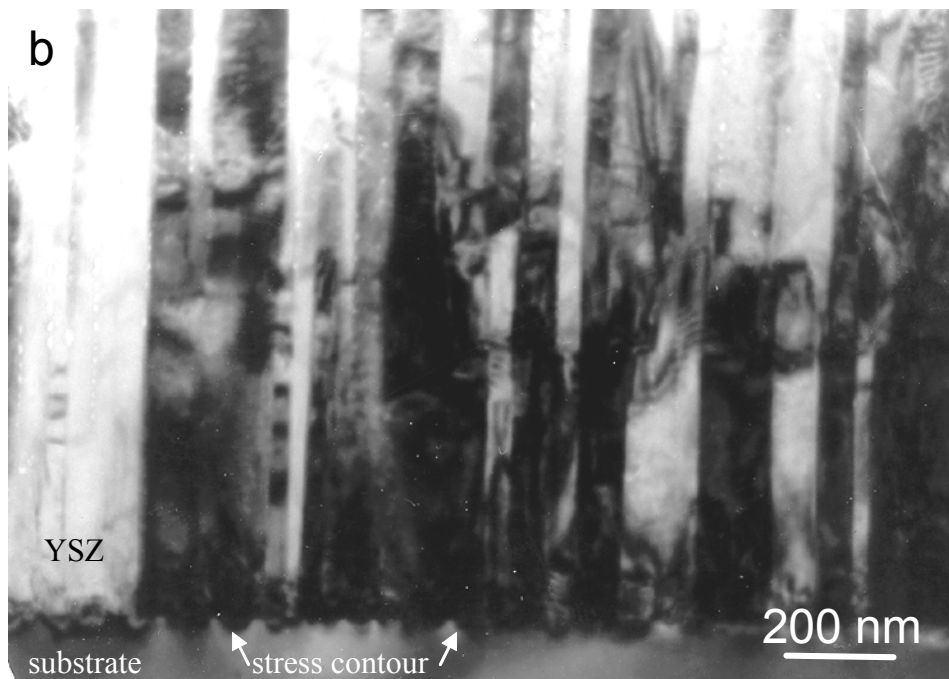




Fig. 5.4 TEM cross sectional micrograph of YSZ coating deposited on a sapphire substrate under stationary conditions: (a) top section ($\sim 1\mu\text{m}$ above the interface) and (b) bottom section of the columns.



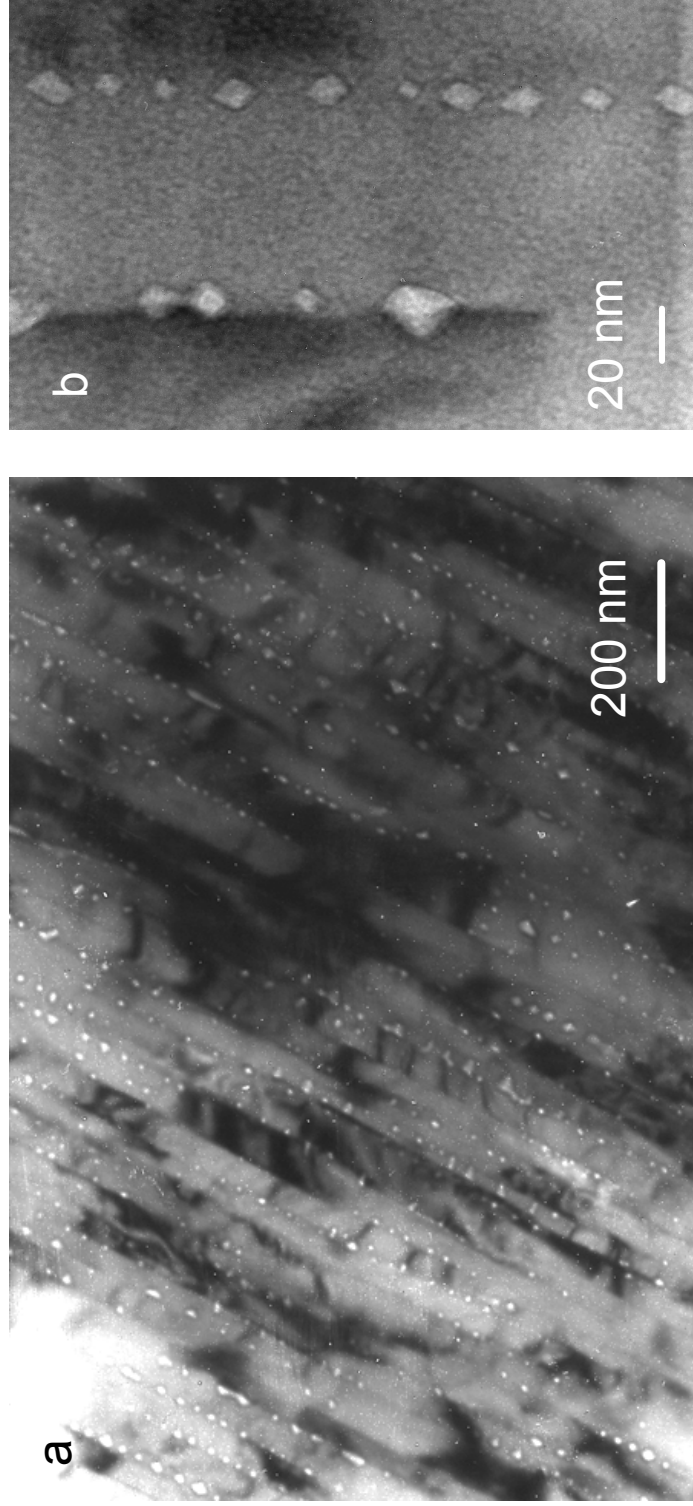


Fig. 5.5 Typical TEM bright field image of YSZ exhibiting inter-columnar porosity. a) lower magnification showing the pores distribution and b) higher magnification of pores with octahedral shape.

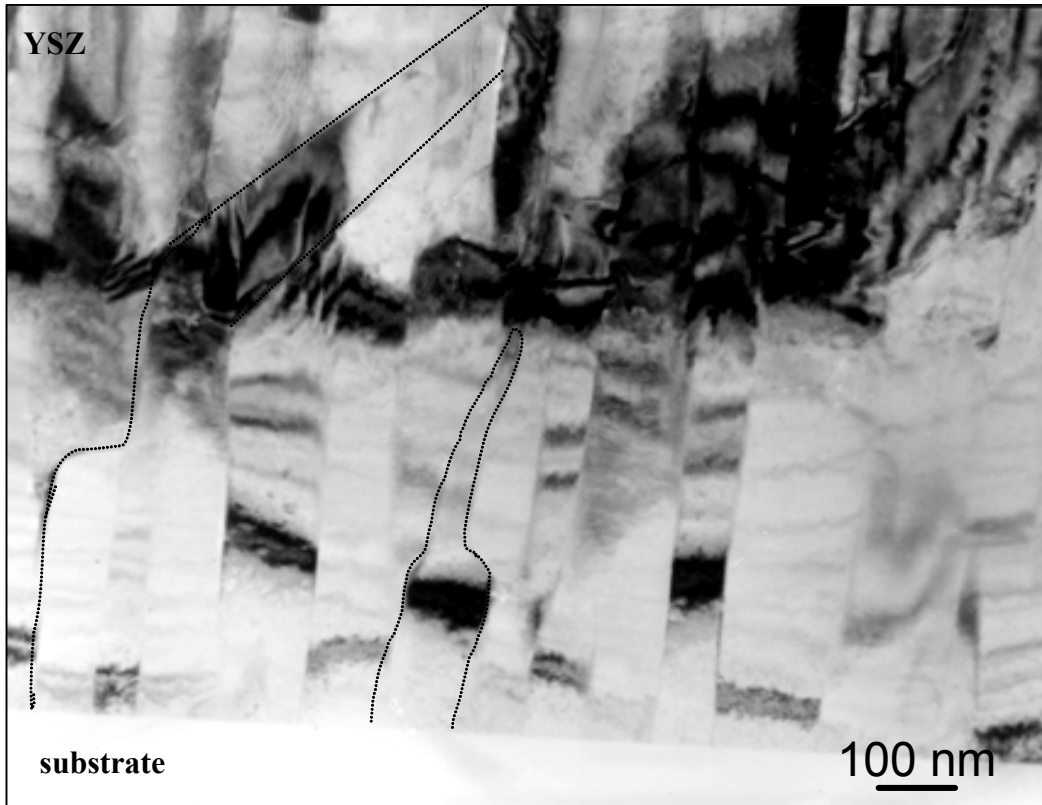
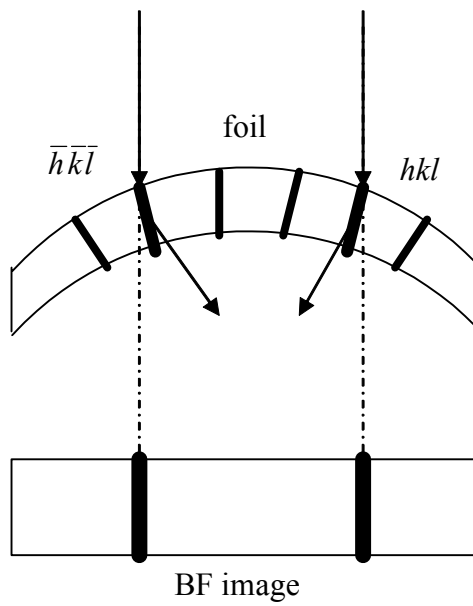


Fig. 5.6 TEM bright-field image of the interface region between the columnar YSZ and the sapphire substrate. Dashed lines indicate the off-axis columns in YSZ. The bend contours (dark lines) correspond to a specimen orientation where a certain set of lattice plane is in Bragg orientation (schematic illustration below).



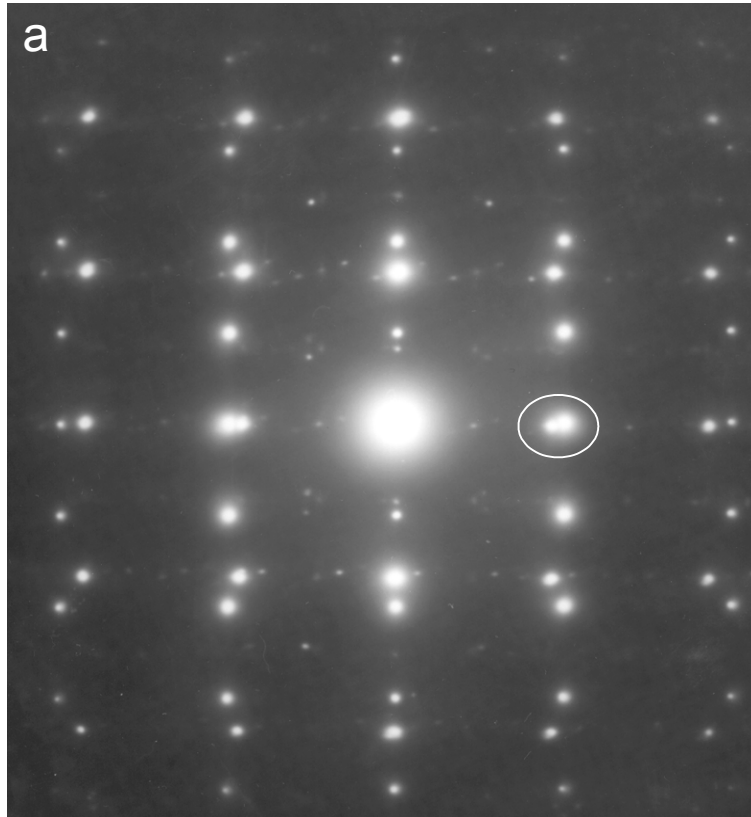
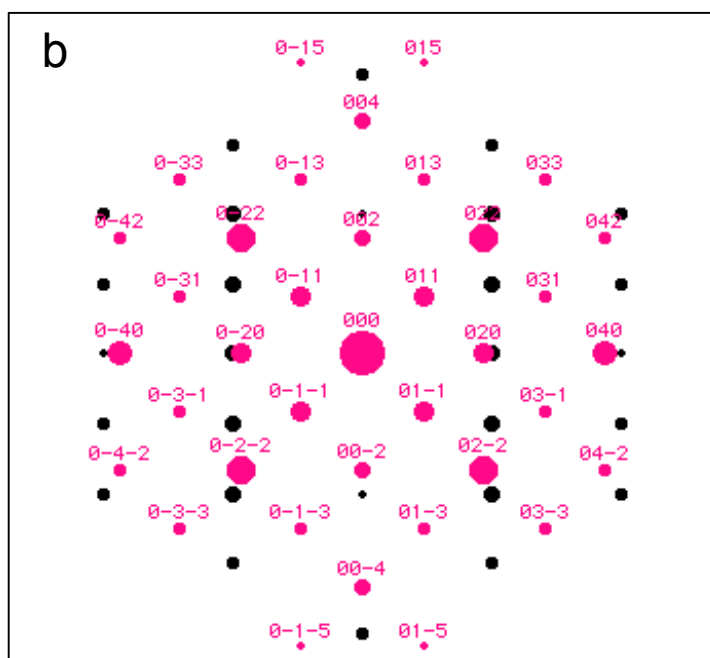


Fig. 5.7 a) SAD pattern and b) schematic diagram with the indexes of diffraction pattern recorded from of the interfacial region between YSZ and sapphire substrate. The red circles present reflection from YSZ in a [100] zone axis, and the black circles present reflection from sapphire in a [1010] zone axis.



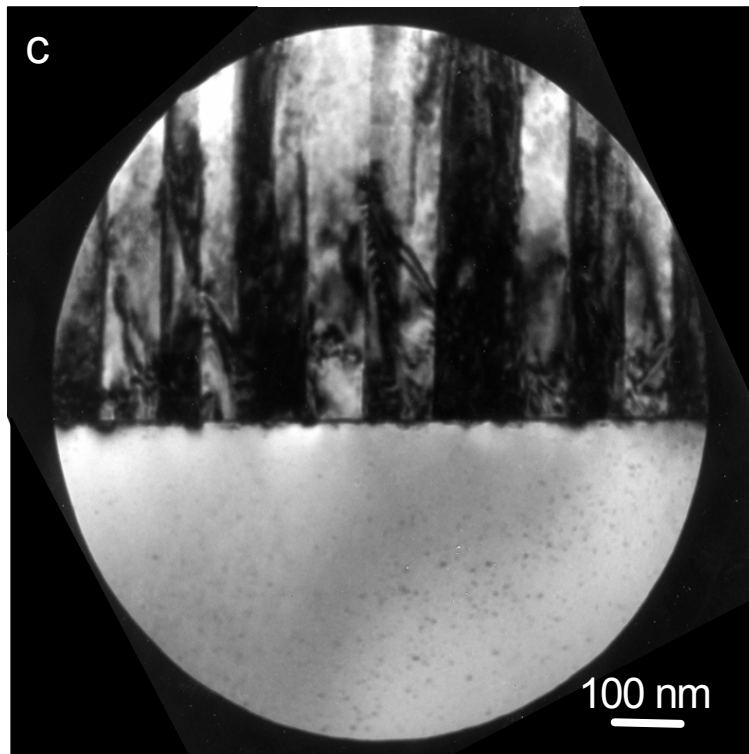
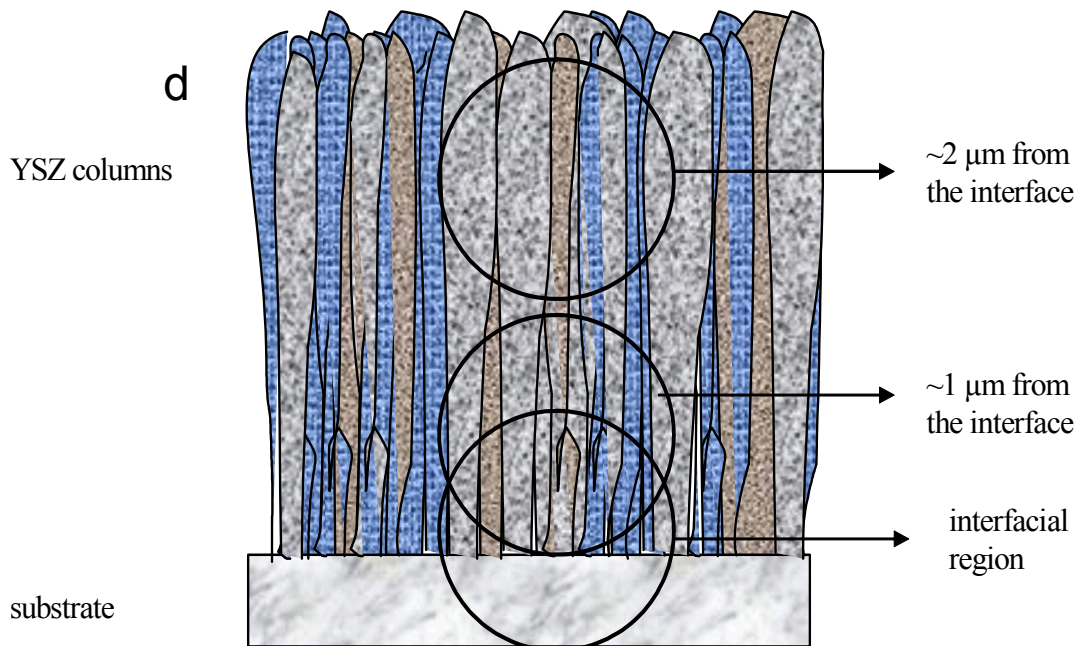


Fig. 5.7 c) Bright-field diffraction pattern including the SAD aperture and d) Schematic illustration of the positions of the SAD apertures at the places where the diffraction patterns were recorded.



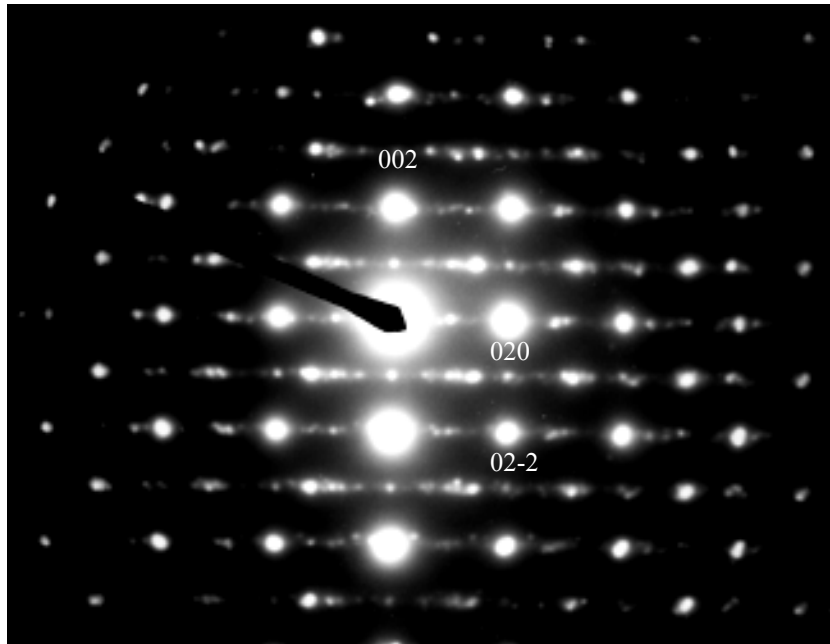
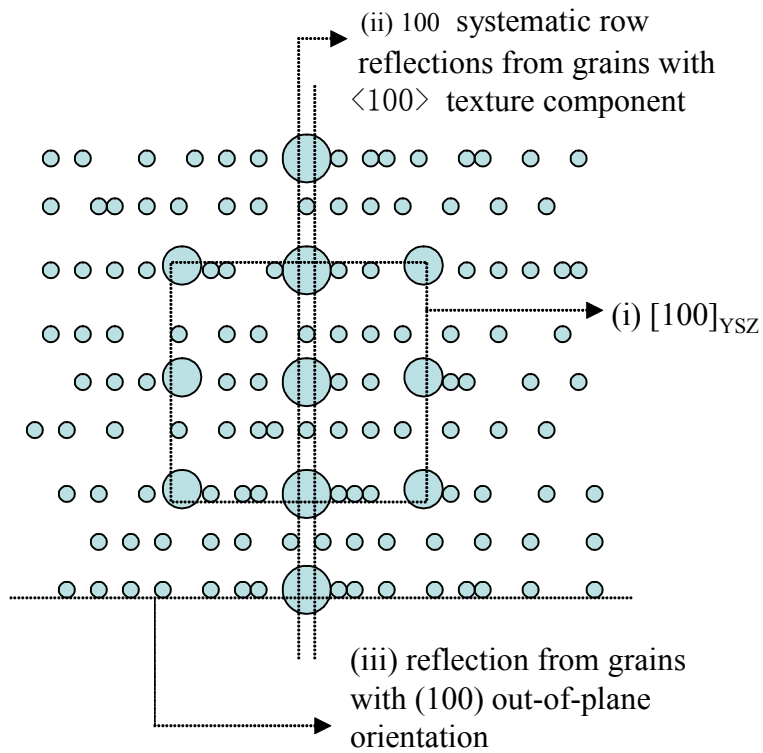


Fig. 5.8 Diffraction pattern of YSZ film corresponding to the $[100]$ zone axis, recorded $\sim 1\mu\text{m}$ from the interface. The schematic diagram of this DP is presents below.



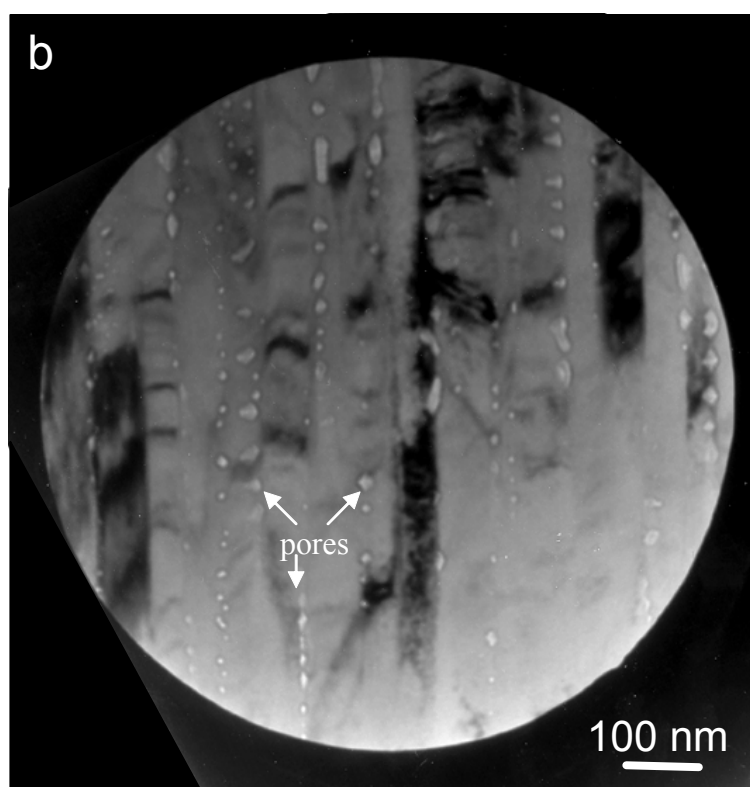
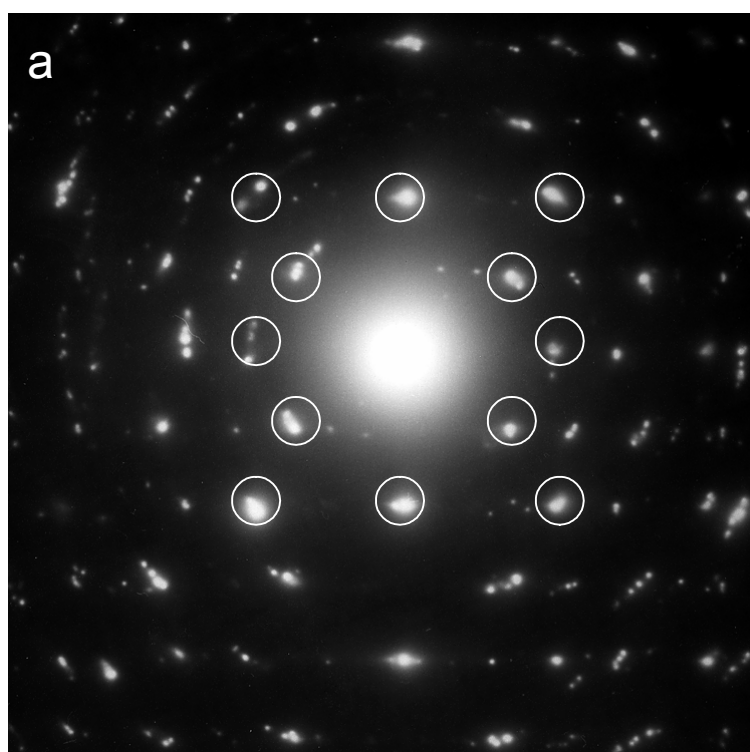


Fig. 5.9(a) Diffraction pattern of YSZ film recorded $\sim 2 \mu\text{m}$ from the interface with sapphire substrate. (b) Bright-field micrograph including the SAD aperture.

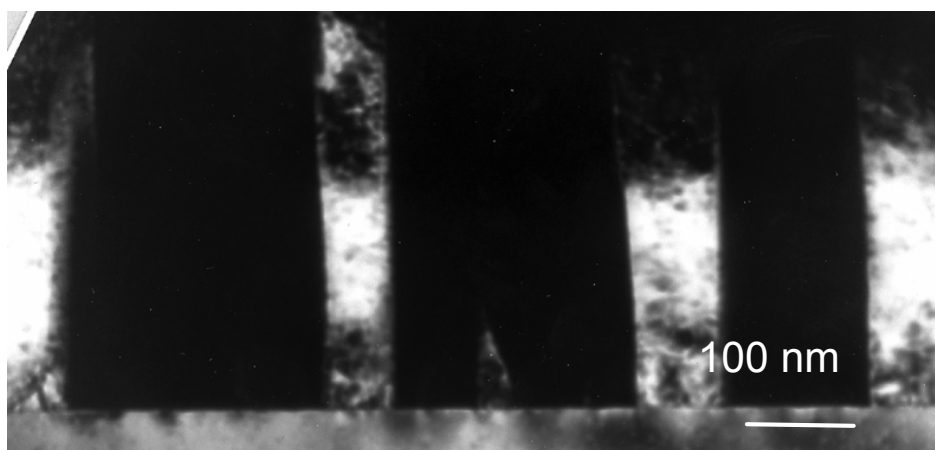
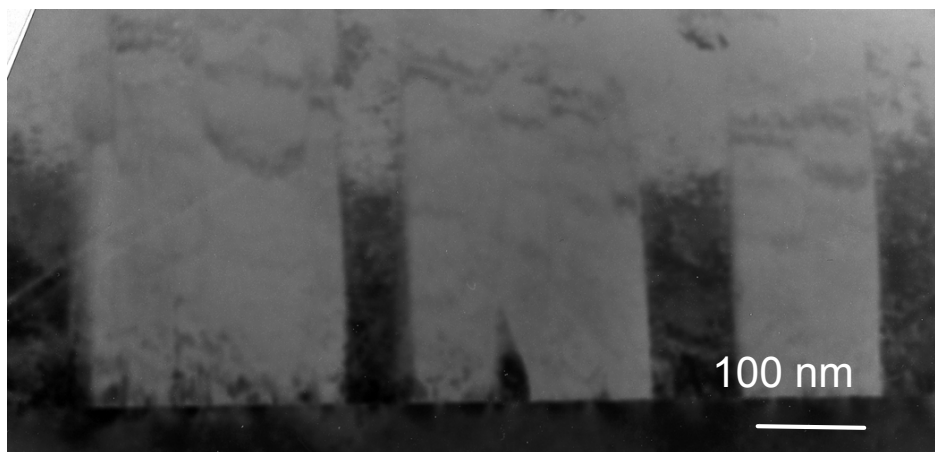


Fig. 5.10 YSZ columns which are well orientated relative to the sapphire. a) bright-field image b) corresponding dark-field image, which was taken with reflection parallel to the interface.

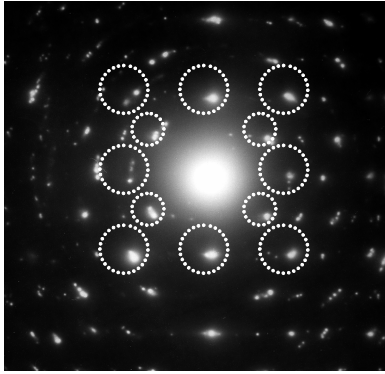


Fig. 5.11d SAD patter from YSZ obtained $\sim 3\mu\text{m}$ from the interface with the sapphire substrate.

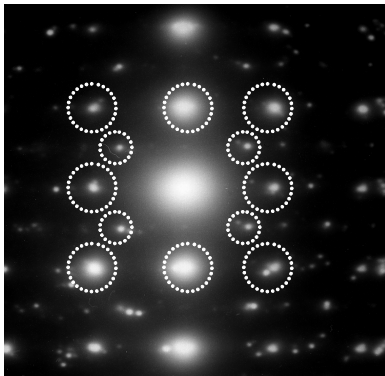


Fig. 5.11c SAD patter from YSZ obtained $\sim 2\mu\text{m}$ from the interface with the sapphire substrate.

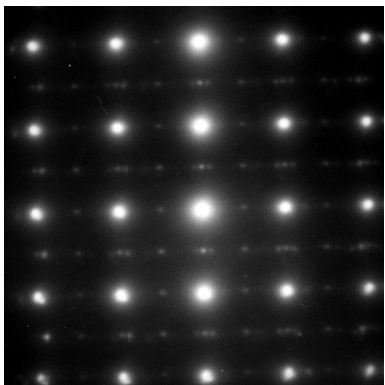


Fig. 5.11b SAD patter from YSZ obtained $\sim 1\mu\text{m}$ from the interface with the sapphire substrate.

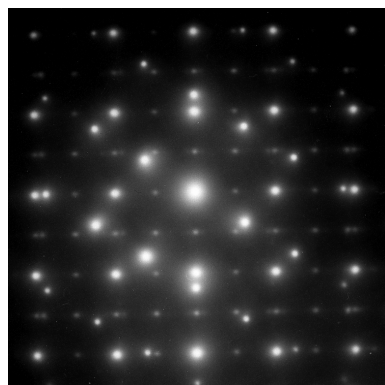
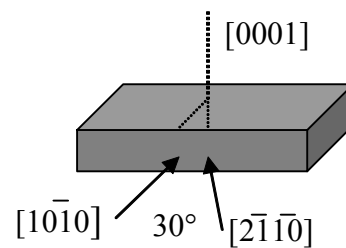


Fig. 5.11a SAD patter from the interfacial region between YSZ and sapphire substrate. The view is in direction when the sample is tilted about -30° around the $[0001]$ zone axis of the sapphire.



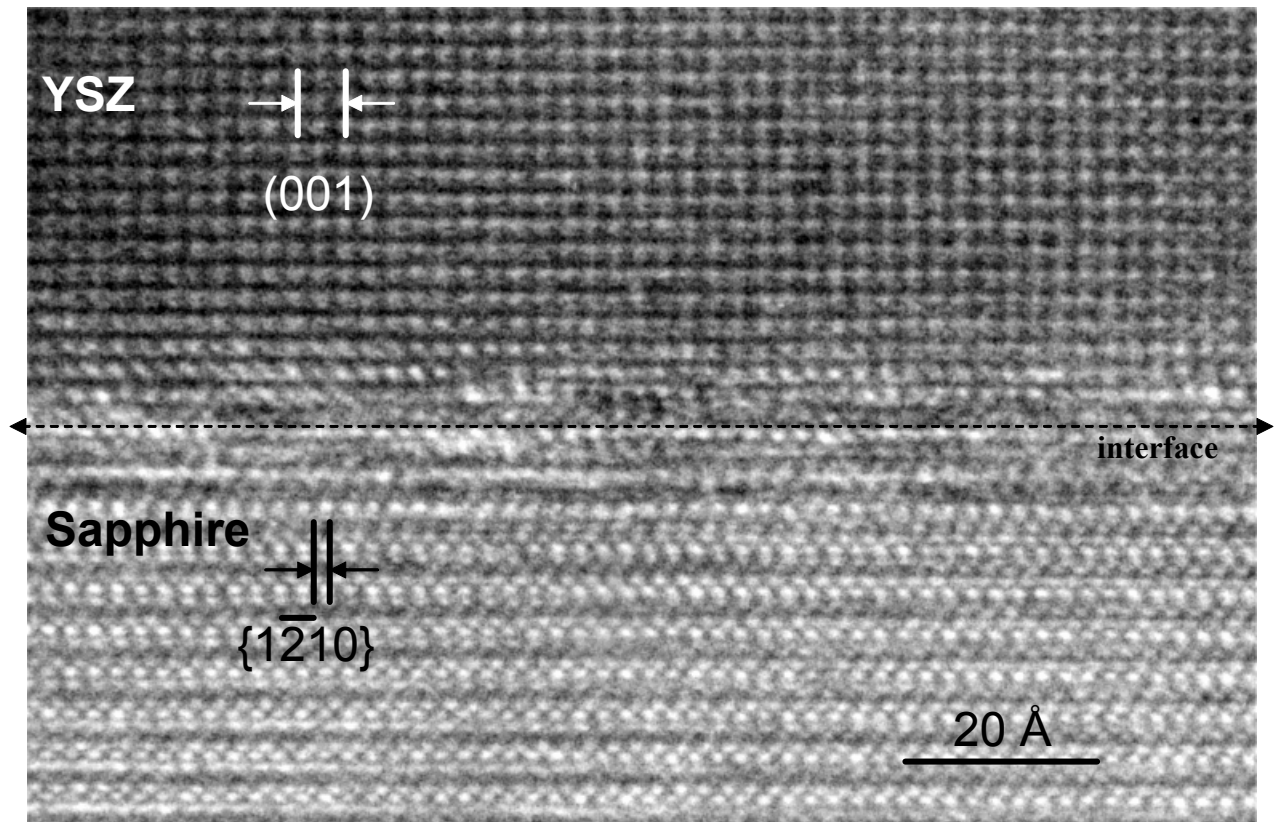
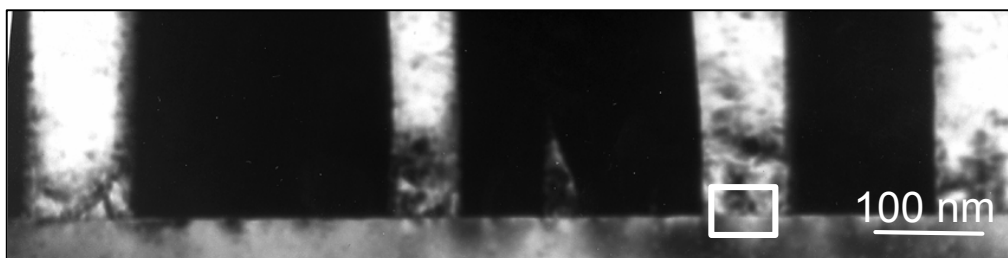


Fig. 5.12 HRTEM image of the interfacial region between YSZ film and sapphire substrate. The image is recorded from the area presented below from the same region as one which is shown in Fig. 5.10. (HRTEM courtesy of G. Richter, MPI-Stuttgart)



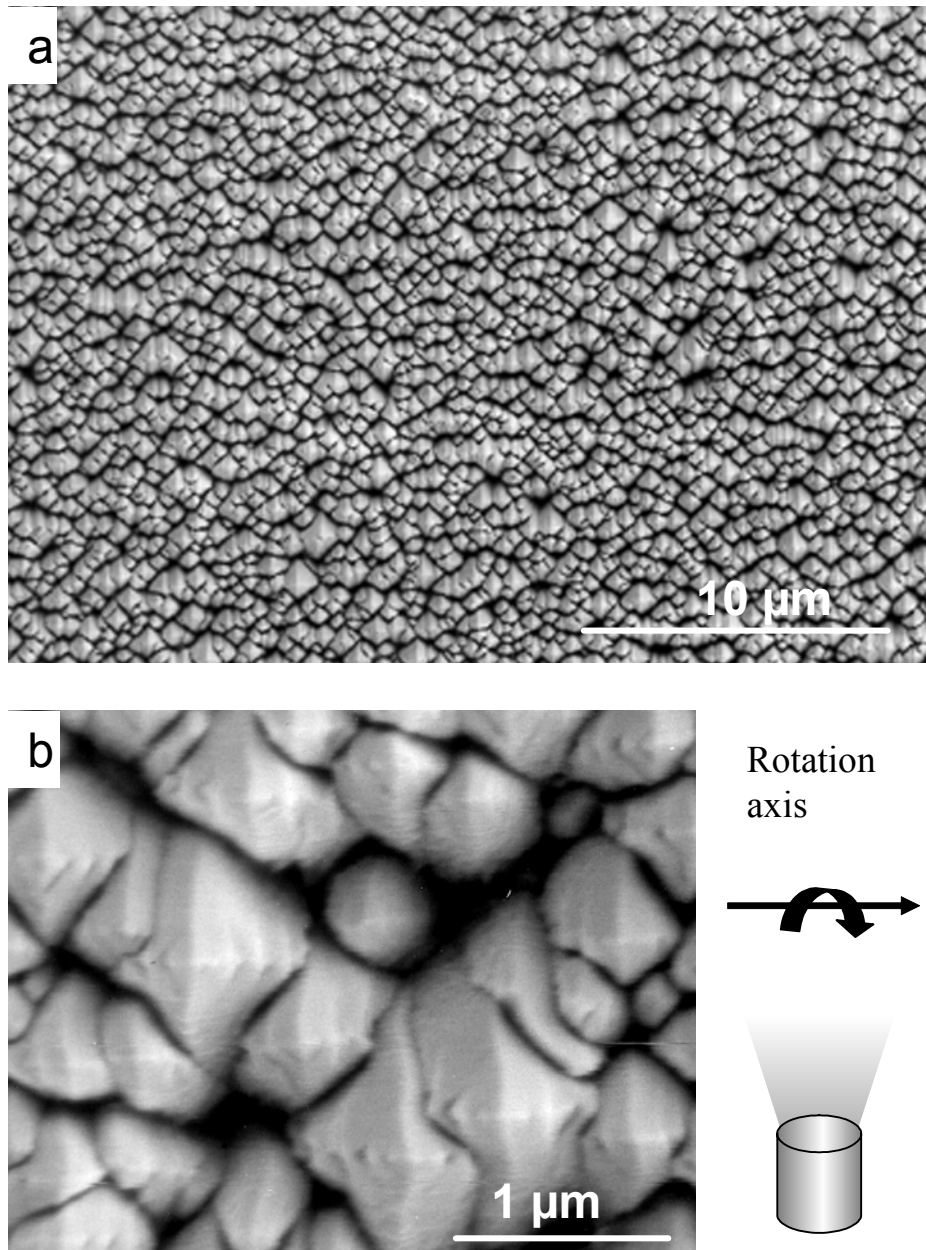
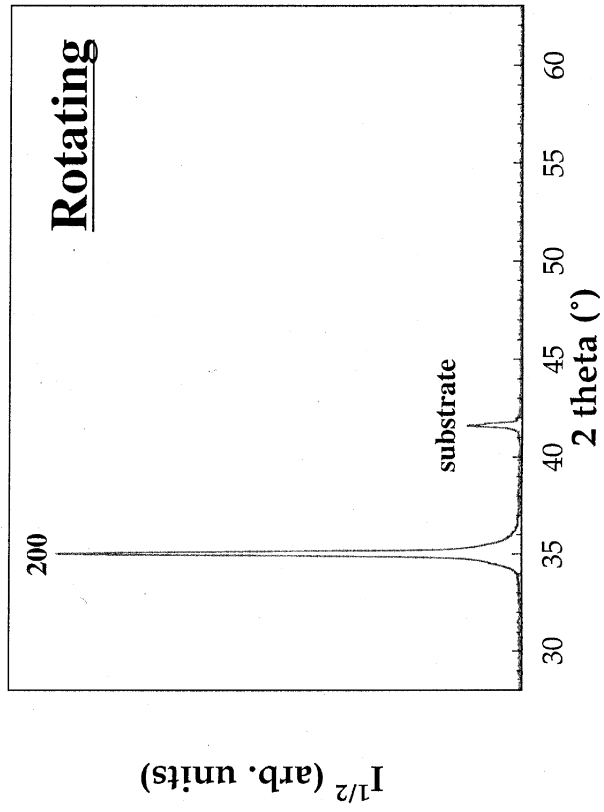
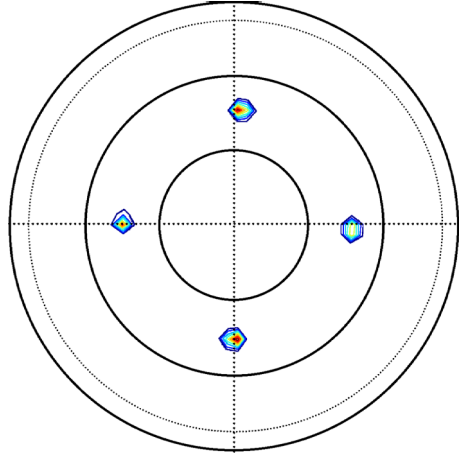


Fig. 5.13 Plane view SEM image of YSZ film grown on sapphire substrate rotated at 8rpm. (a) surface morphology of the film deposited on rotating substrate (b) details of the column tip: pyramidal shape with diagonals oriented orthogonal and parallel to the rotating axis.



a) X-ray $2\theta-\theta$ scans



b) 202 pole figure

Fig. 5.14 (a) $2\theta-\theta$ scans and (b) 202 pole figure of YSZ film deposited on a rotating sapphire substrate. (XRD by J. Cho, UCSB)

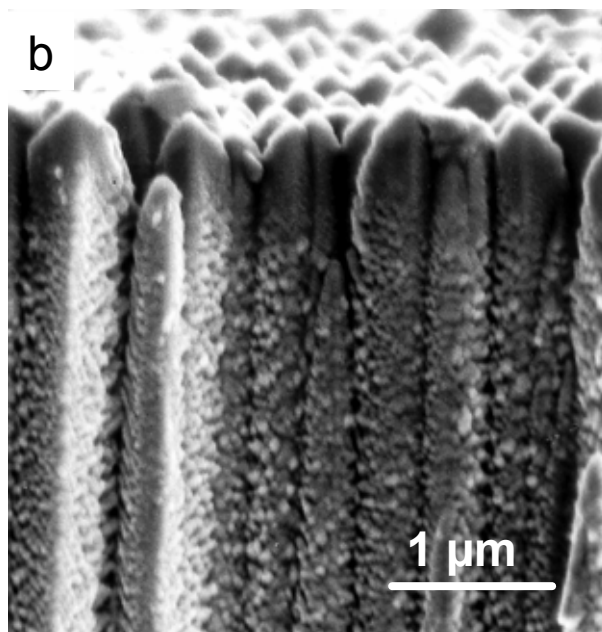
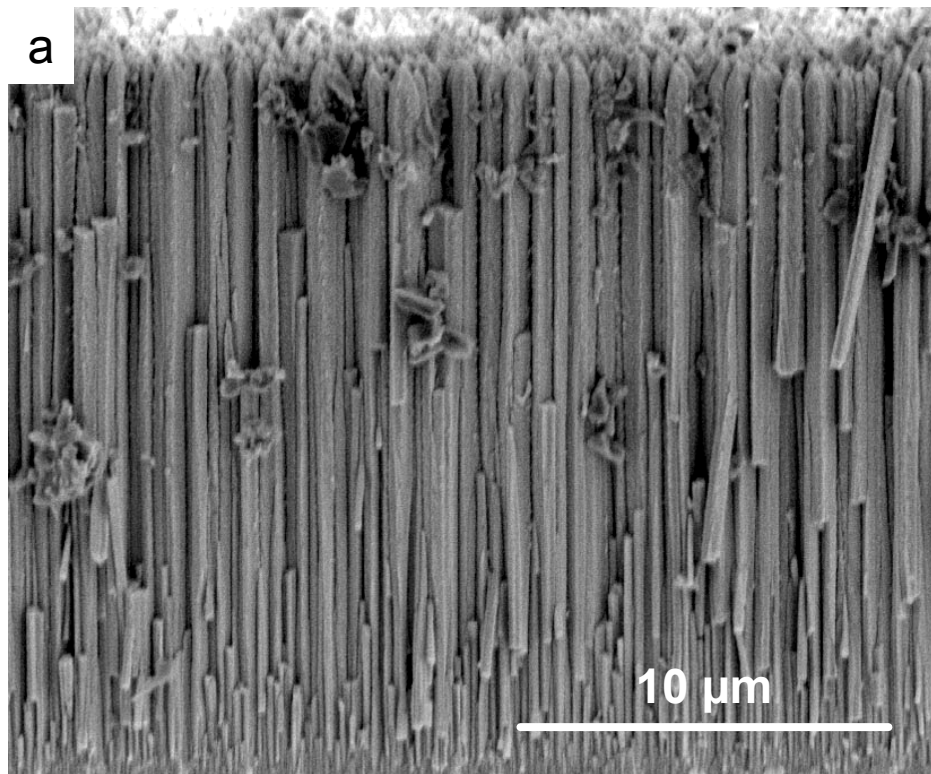


Fig. 5.15 (a) and (b) SEM fracture surface of YSZ coating grown on rotated sapphire substrate. At higher magnification (b) the porous structure became visible.

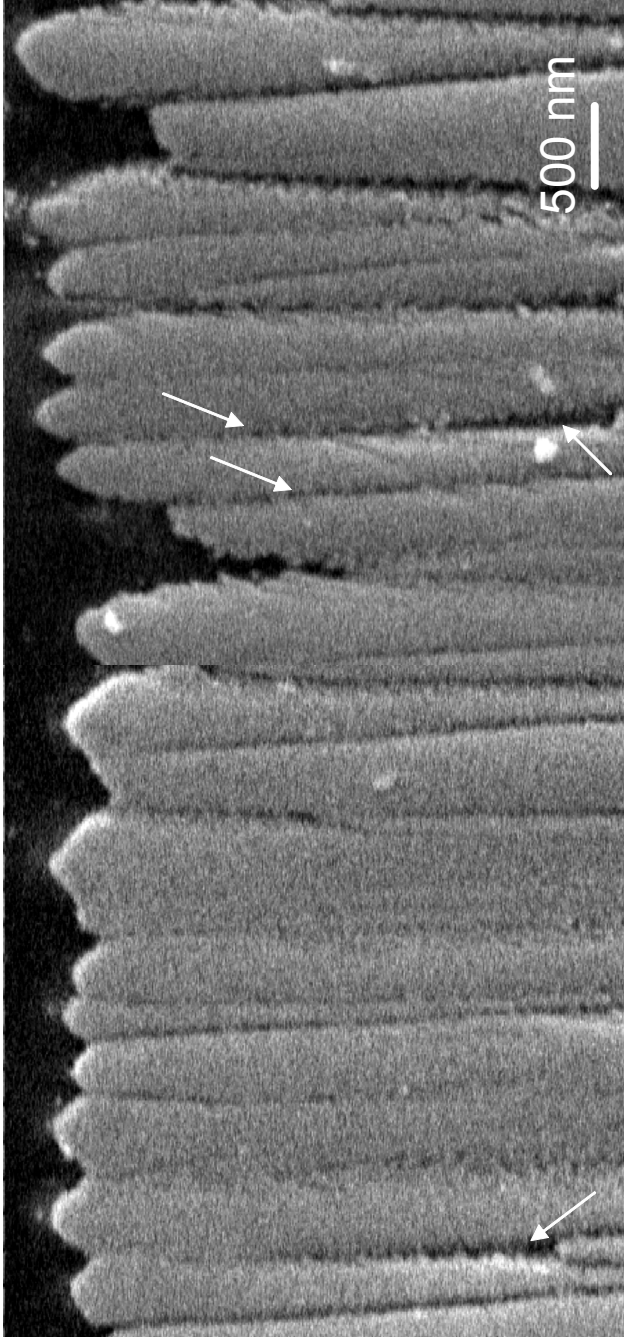


Fig. 5.16 SEM micrograph of polished cross-section of YSZ film deposited on a rotated substrate. The gaps (pointed by the lower arrows) and closed inter-columnar porosity are indicated by arrows.

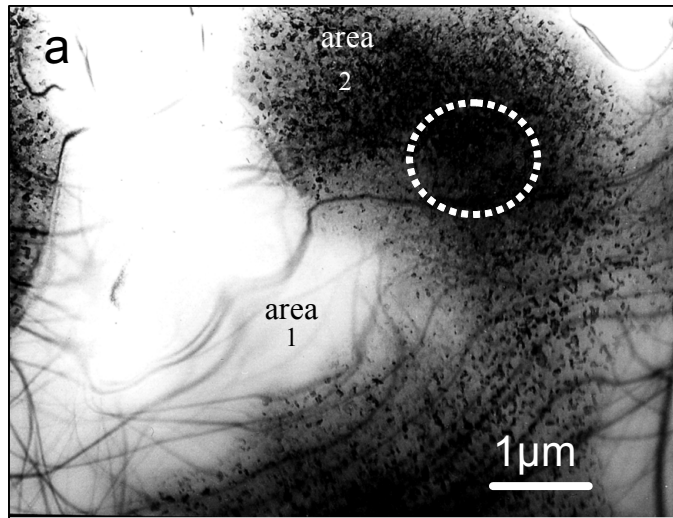


Fig. 5.17 a) Plane - view BF TEM image of the YSZ film deposited on a rotated substrate and b) schematic illustration of the image above in cross-sectional and plan-view

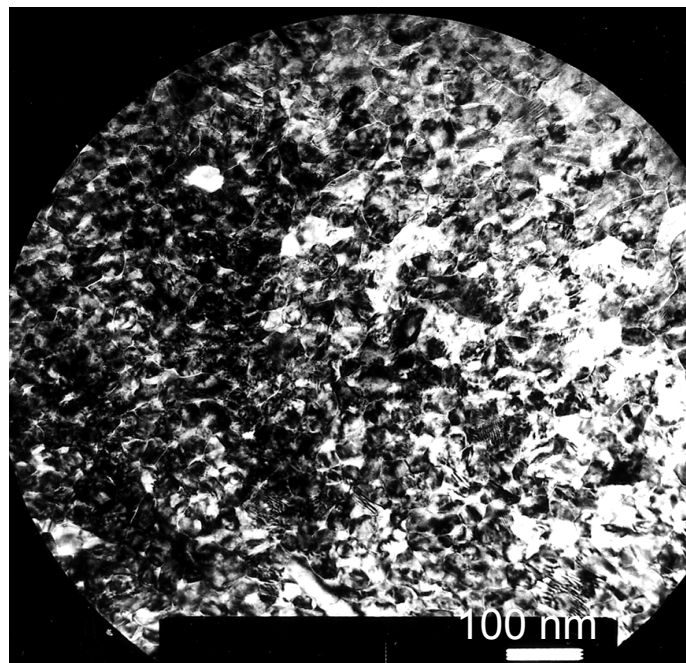
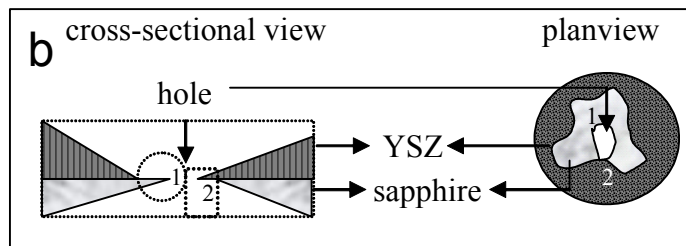


Fig. 5.18 Higher resolution BF TEM image of the area pointed by dashed line in Fig.5.17a.

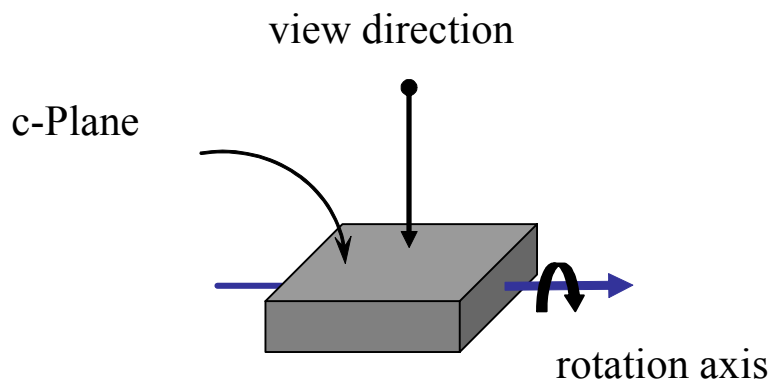
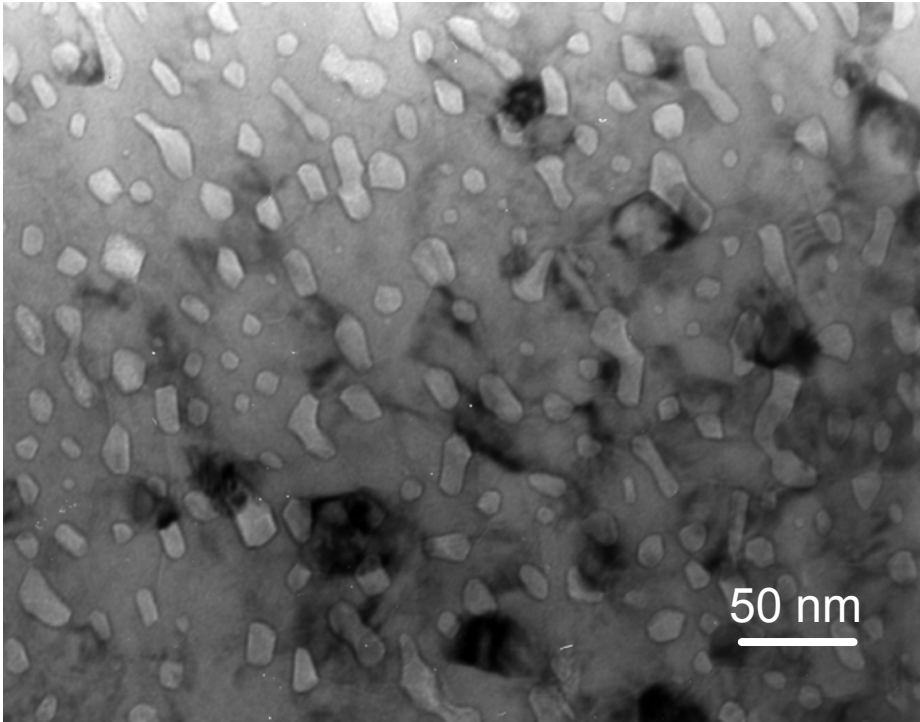


Fig. 5.19 Bright-field TEM image showing the development of porosity in the YSZ coating in a plane-view sample.

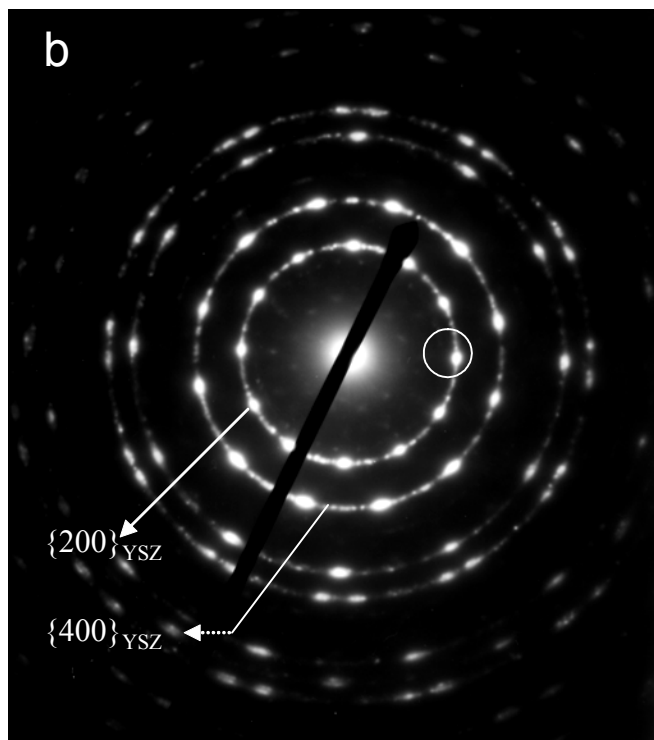
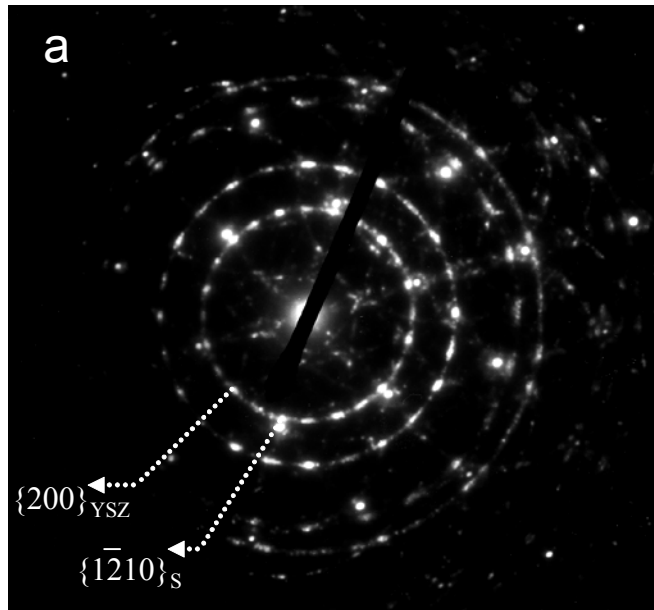


Fig. 5.20 SAD pattern obtained (a) from the interface between YSZ and sapphire; and (b) from YSZ film near the interface (without substrate).

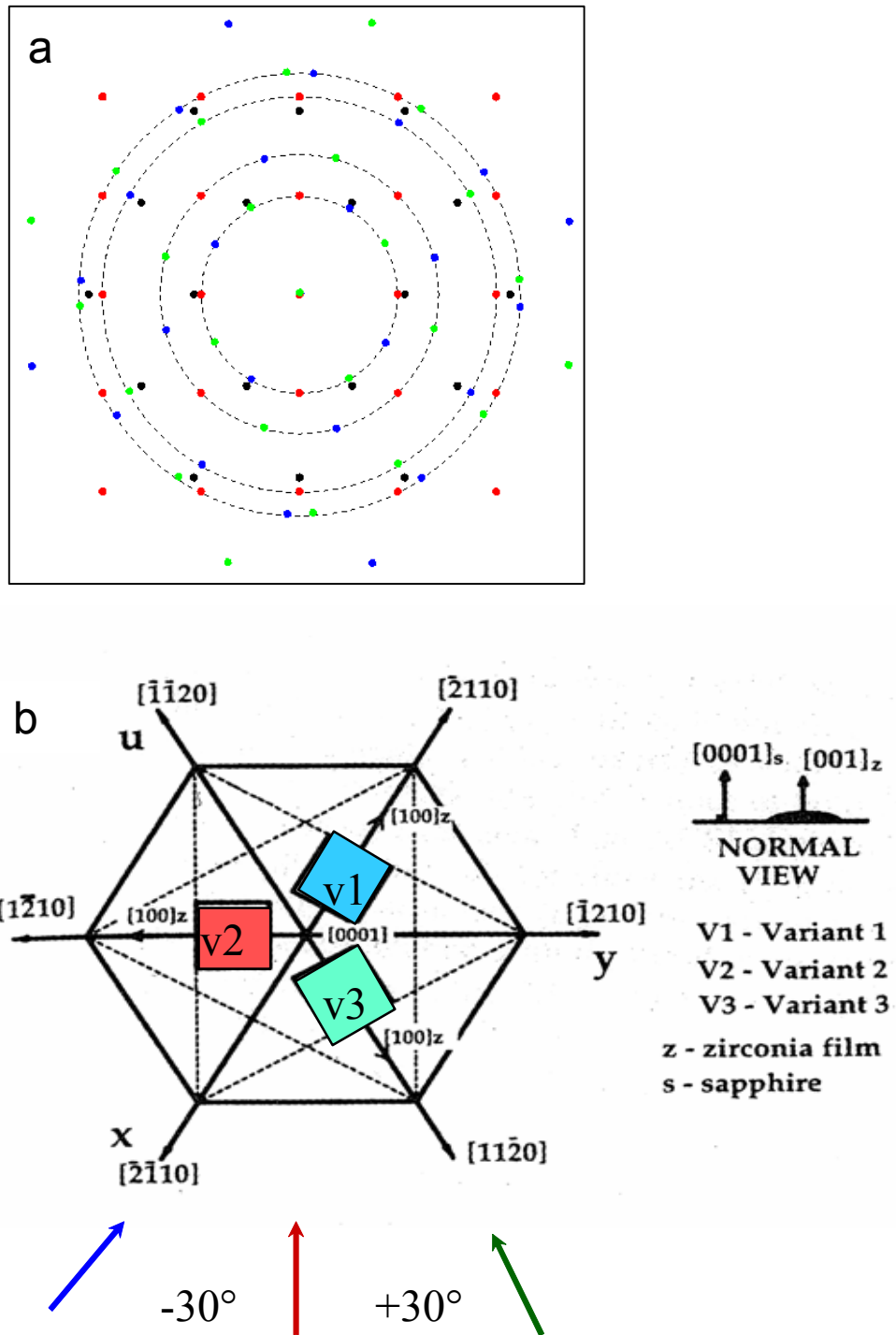


Fig. 5.21 Schematically illustrations (a) interpretation of the plane-view diffractions pattern including reflections from the sapphire substrate and YSZ film; (b) three equivalent in-plane orientation of cubic YSZ on c-plane sapphire substrate. Figure adapted from *Cain and Lang* [94 CaL].

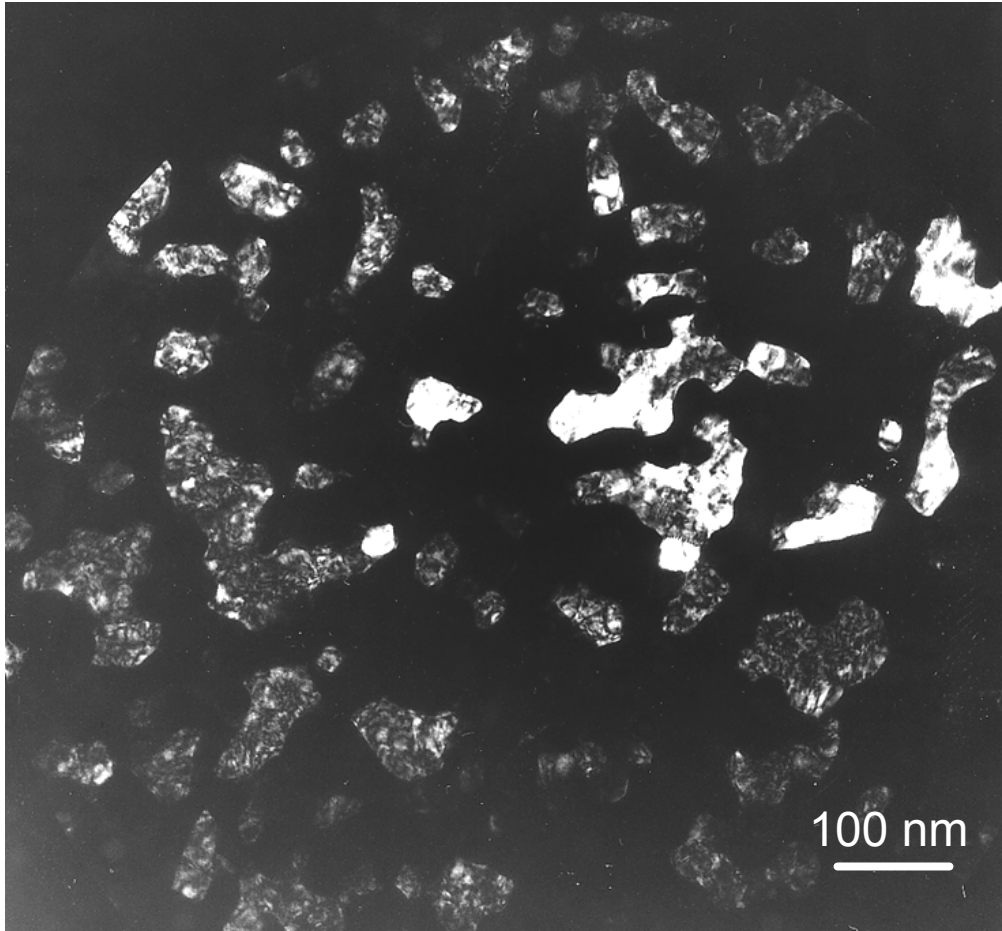


Fig. 5.22 Dark-field TEM plane-view image of YSZ polycrystalline film. The grains which are in a Bragg condition appear bright.

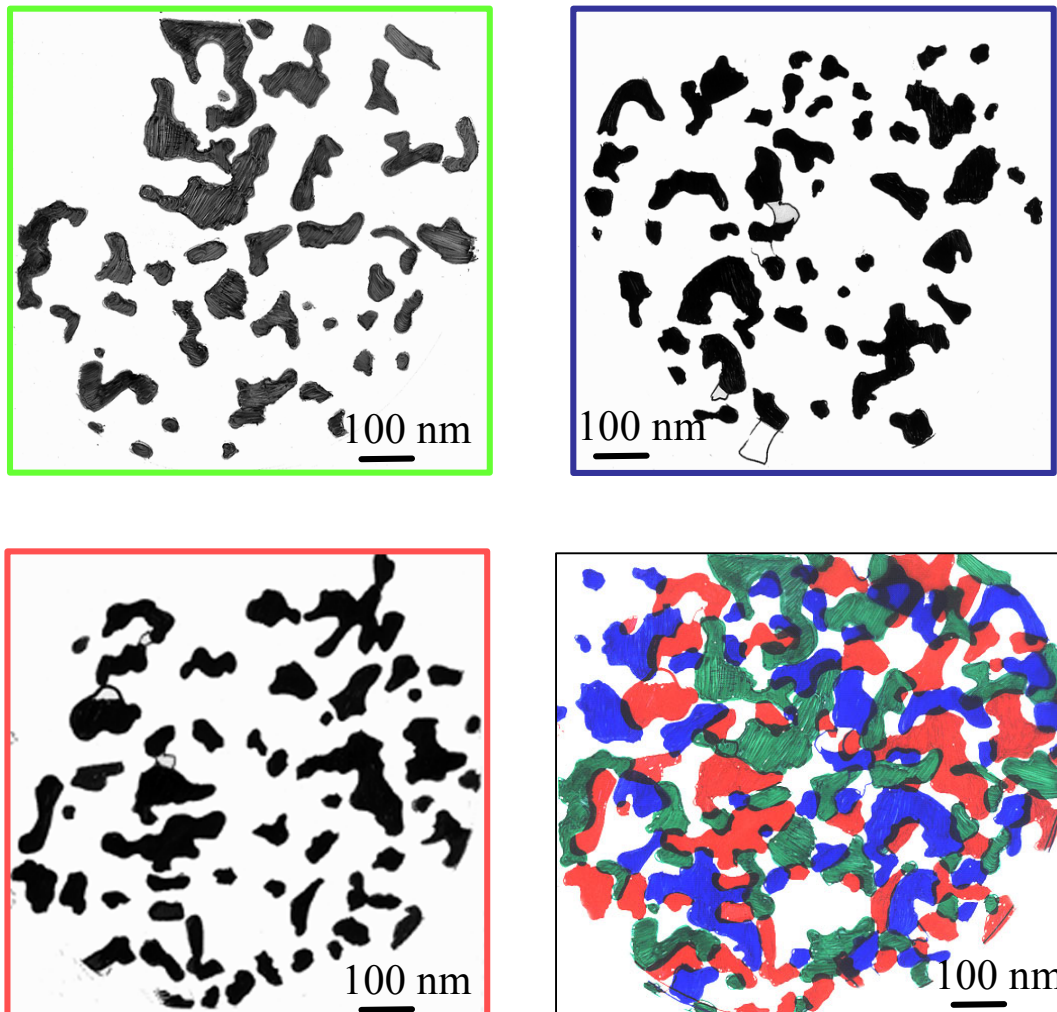


Fig. 5.23 (a-c) Spatial distribution of each of the three variants of in-plane orientation. The amount of all well orientated grains (red, green and blue areas) near the interface is 83%. The white areas corresponds to that grains which are randomly oriented in the plane of sapphire.

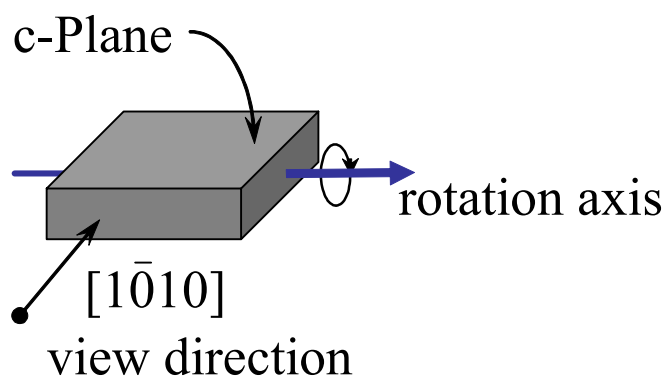
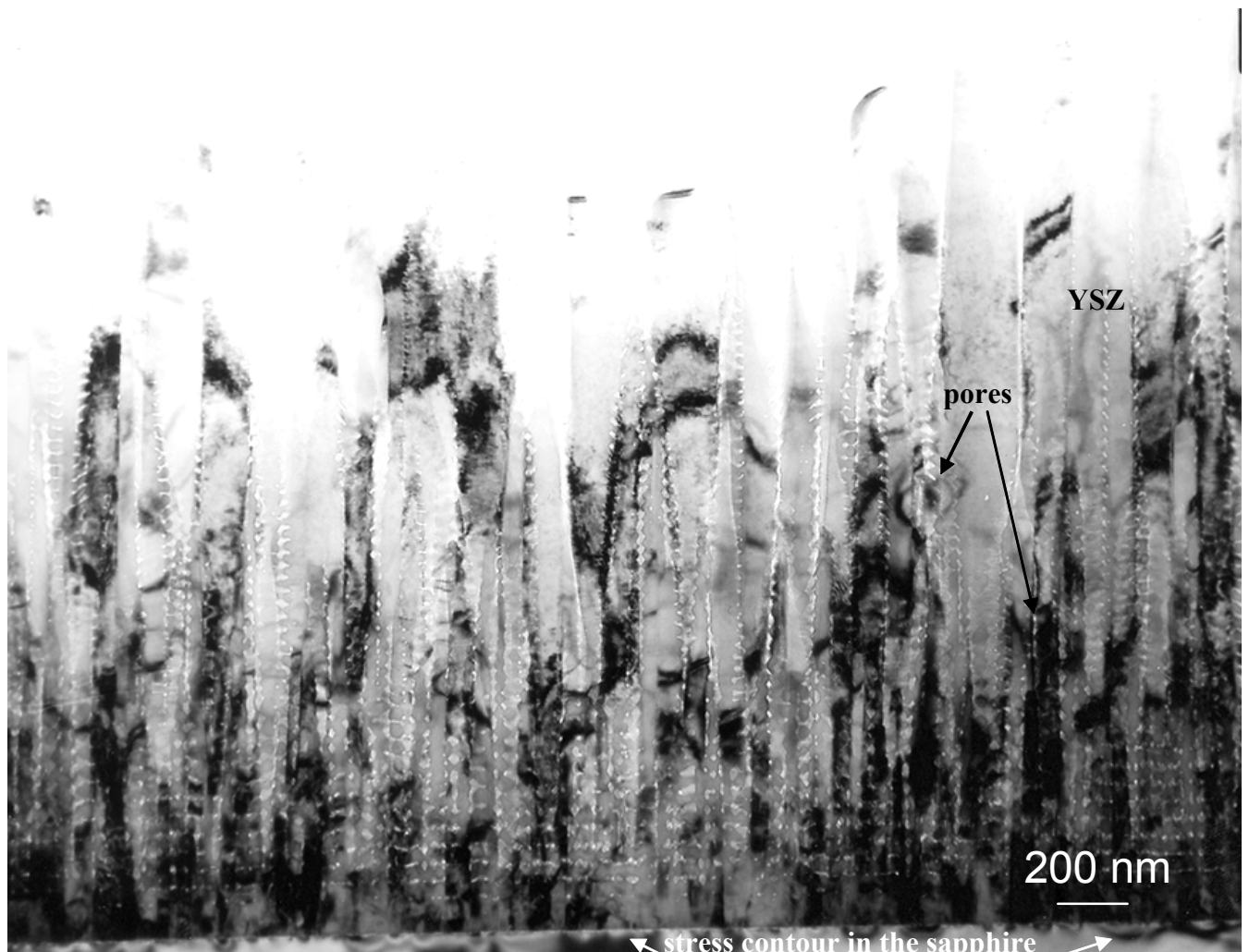


Fig. 5.24 BF TEM cross-sectional micrograph of YSZ film deposited on a rotating sapphire substrate (S-YSZ_R). A view in the direction perpendicular to the axis of substrate rotation. The highly aligned inter-columnar porosity (bright spots indicated by arrows) is evident. The stress contours in the sapphire below the YSZ columns are denoted by white arrows.

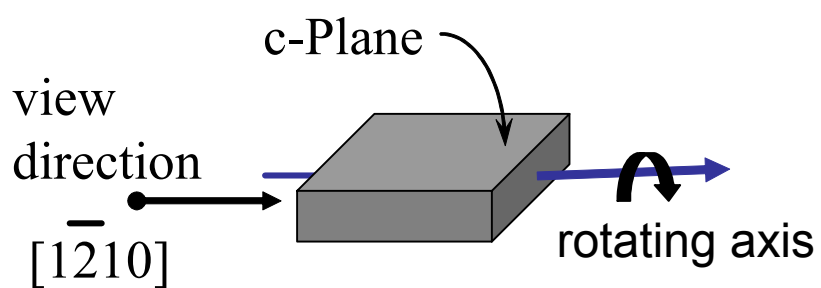
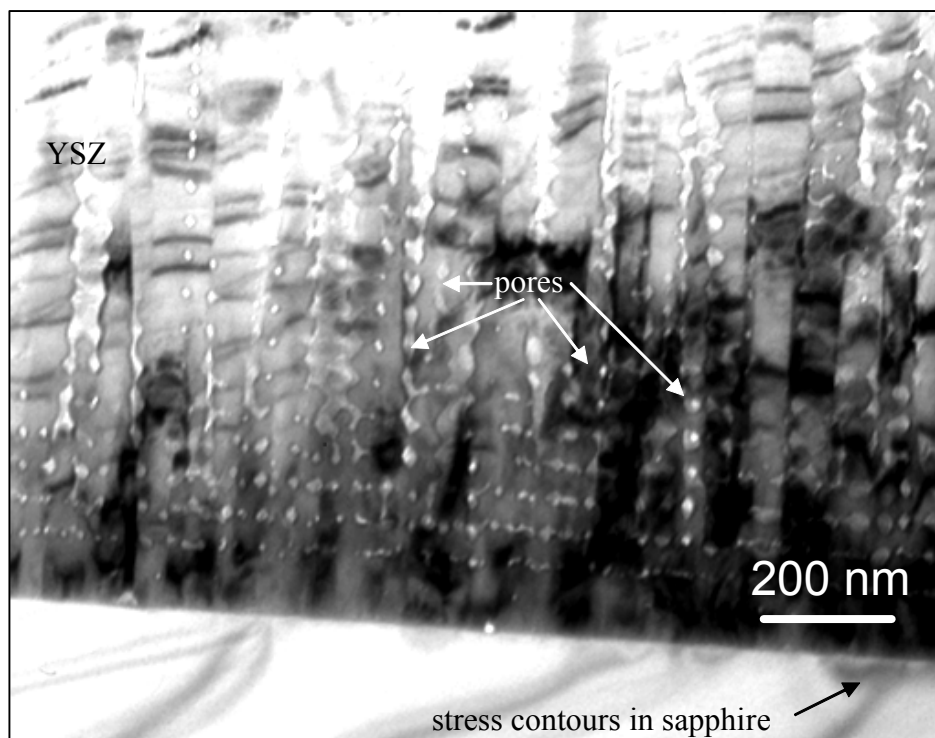


Fig. 5.25 BF TEM cross-sectional micrograph of YSZ film deposited on a rotated sapphire substrate. The view direction is parallel to the axis of substrate rotation.

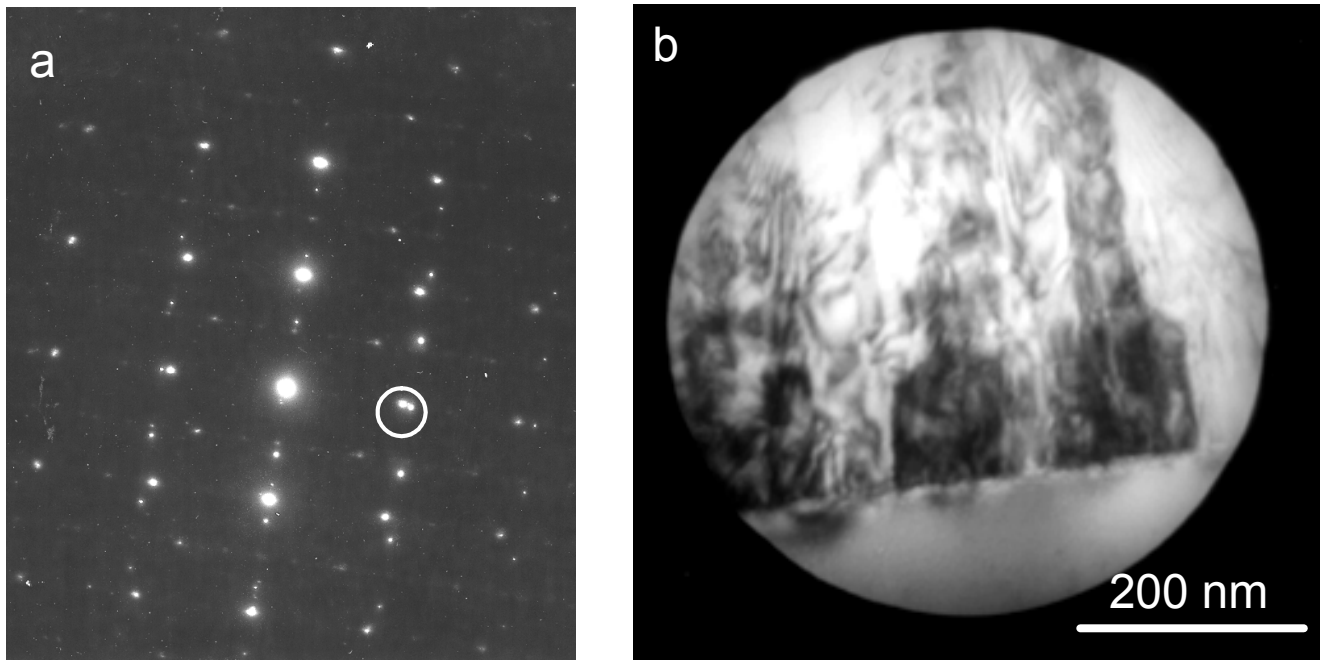


Fig. 5.26 (a) SAD pattern from interfacial region between sapphire substrate and YSZ film in S-YSZ_R sample; (b) corresponding bright - field image and (c) schematic diagram and indexing of the diffraction pattern, where red and black circles represent reflections from YSZ and sapphire, respectively.

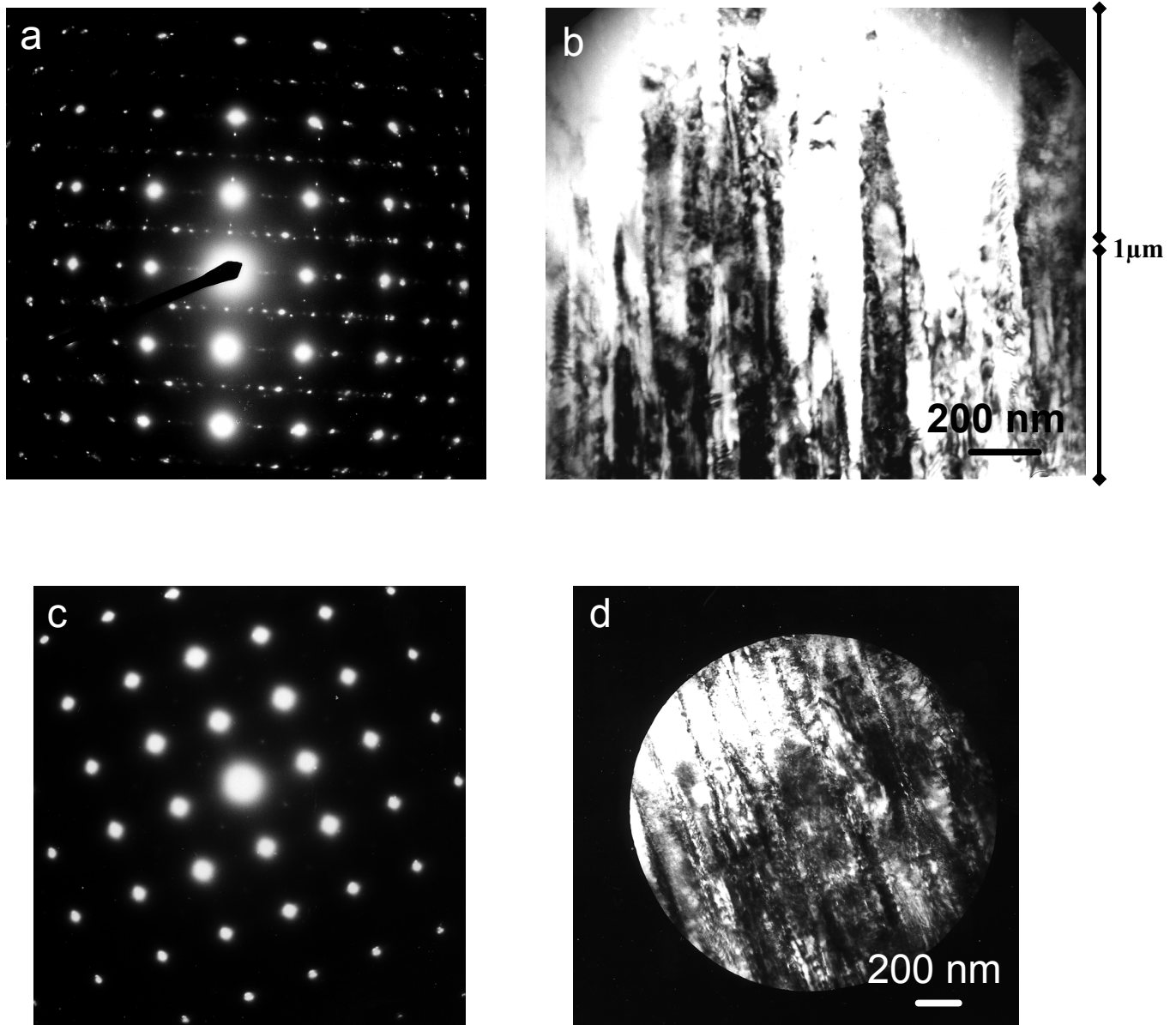


Fig. 5.27 (a) SAD pattern from YSZ obtained $\sim 1\text{-}2\ \mu\text{m}$ from the interface with sapphire substrate; (b) corresponding bright-field image from the place; (c) SAD pattern recorded $\sim 2.5\ \mu\text{m}$ from the interface; (d) bright-field pattern including the SAD aperture from the place.

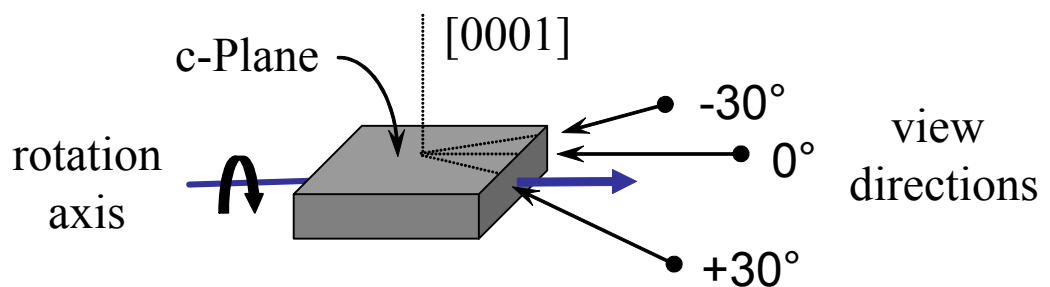
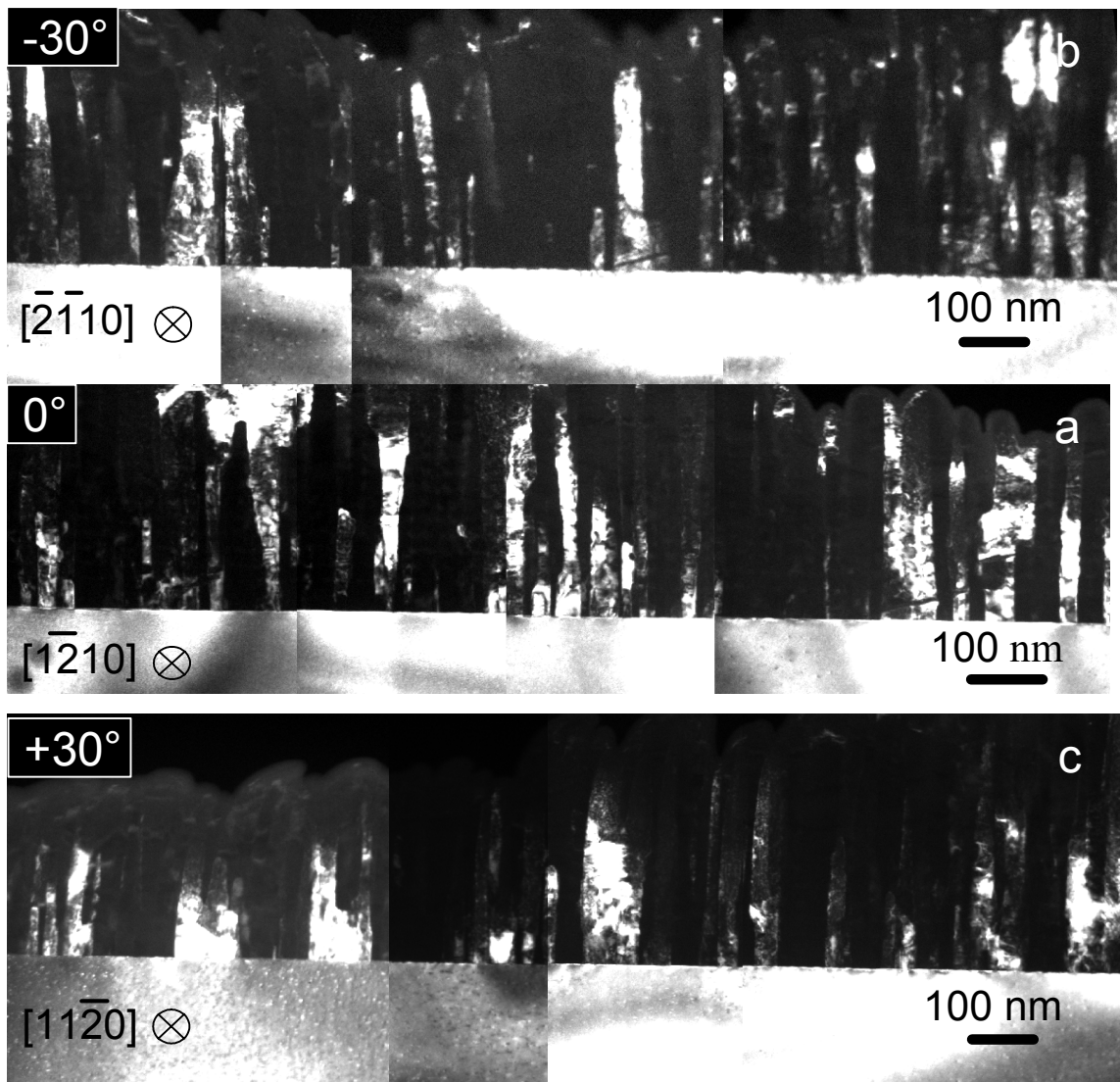


Fig. 5.28. DF TEM micrographs obtained from the interfacial region. (a) in direction parallel to the axis of substrate rotation; (b) and (c) present images taken with tilting the sample about -30° and $+30^\circ$ from $[1\bar{2}10]_S$ around the $[0001]$ axis of the sapphire, respectively.

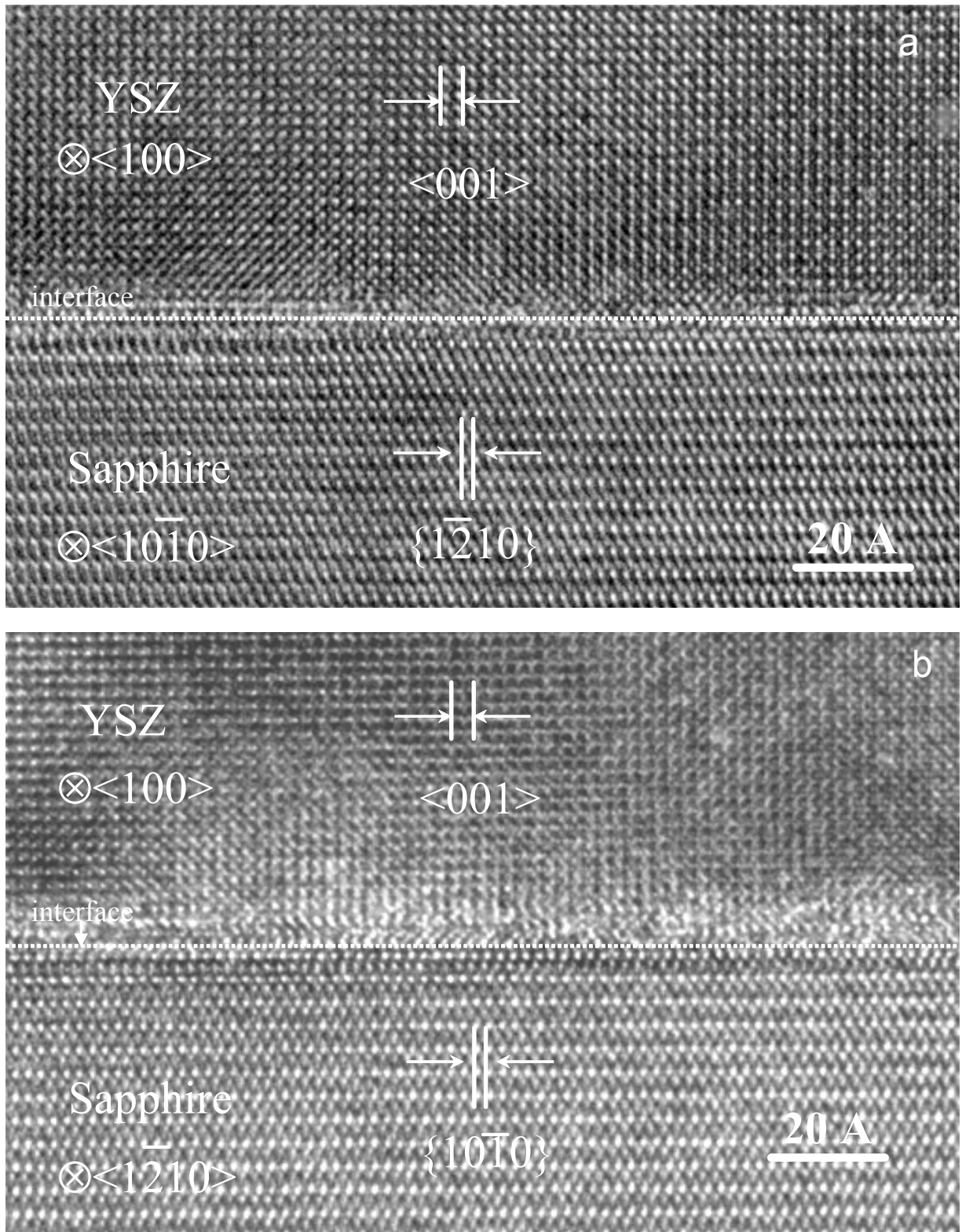


Fig. 5.29 HRTEM micrographs from the interfacial region between YSZ and sapphire substrate. (a) the incident beam is parallel to the $[1010]$ zone axis of sapphire, view perpendicular to the rotation axis; (b) the incident beam is parallel to the $[1210]$ zone axis, view parallel to the axis of rotation. HRTEM courtesy of G. Richter, MPI-Stuttgart

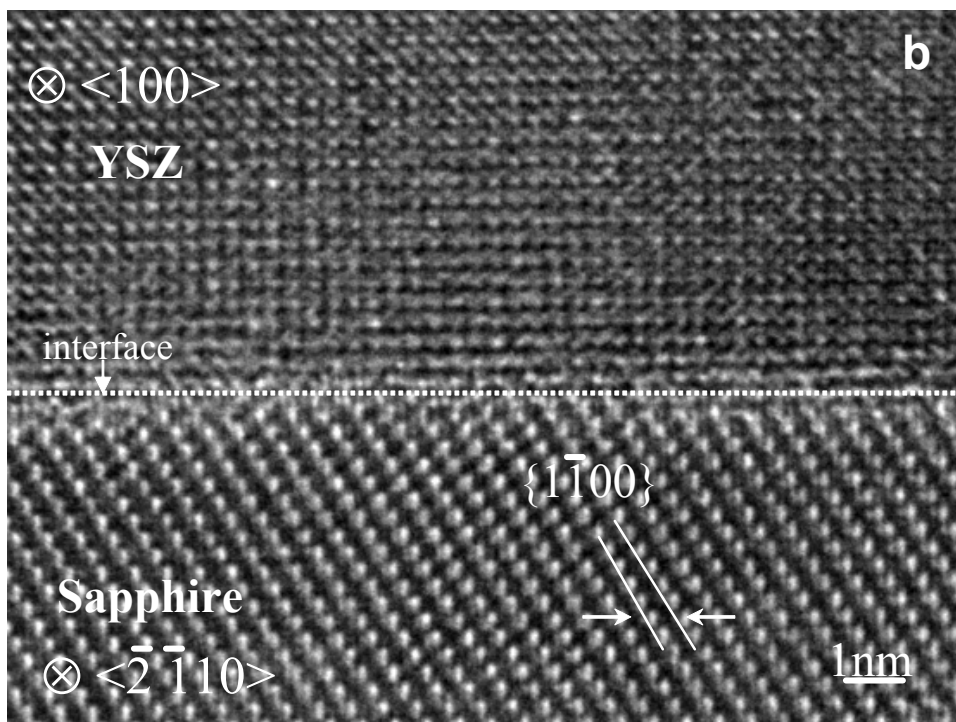
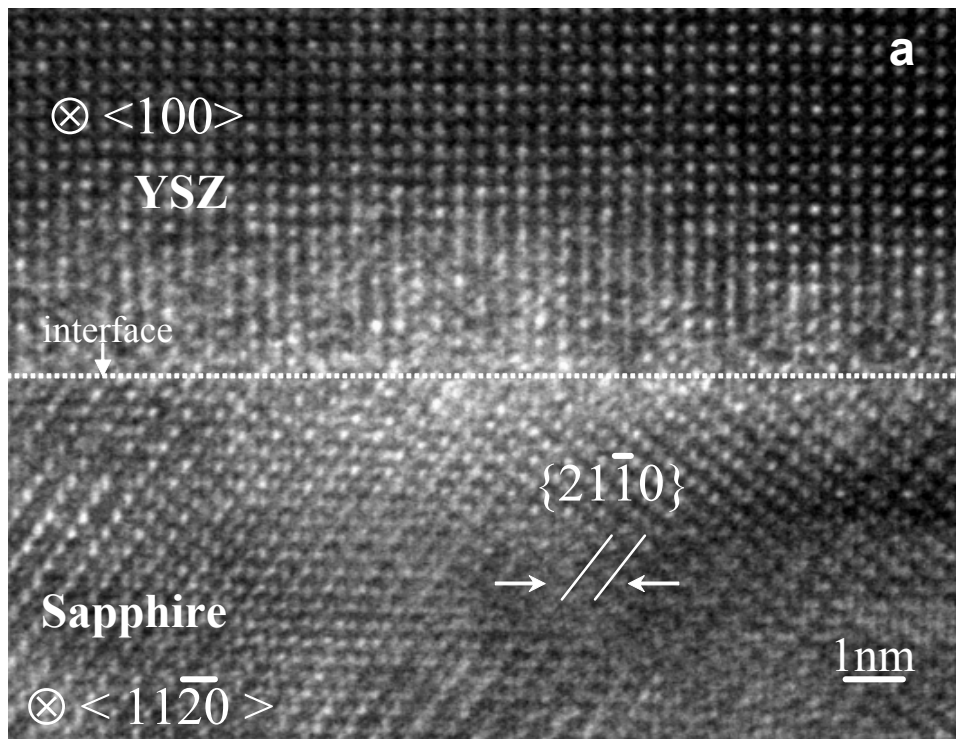


Fig. 5.30 HRTEM micrographs from the interfacial region between YSZ and sapphire in S-YSZ_R sample. a) the sample was tilted +30° from the $[10\bar{1}0]_S$ around the $[0001]_S$ i.e. the incident beam is parallel to $[11\bar{2}0]$ the view direction, and b) the sample is tilted -30° from the $[1010]_S$ i.e. the incident beam is parallel to the $[2\bar{1}\bar{1}0]_S$ view direction.

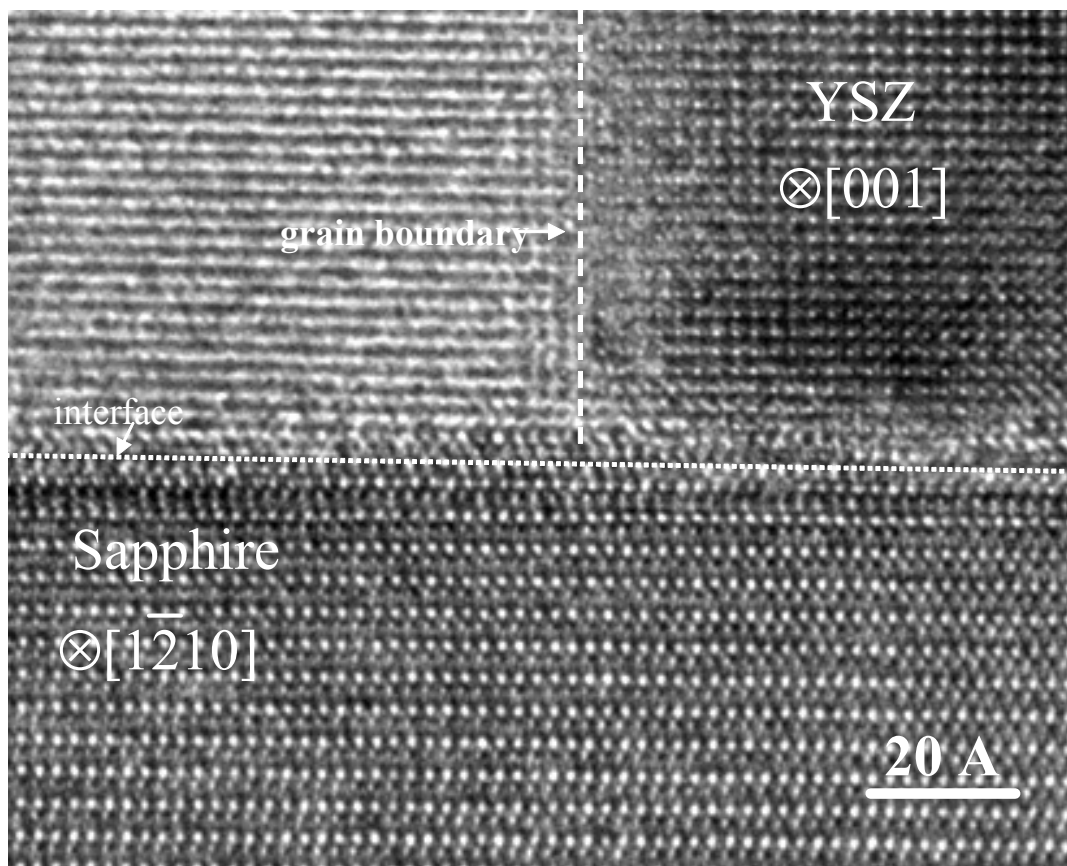


Fig. 5.31 HRTEM micrograph from the interfacial region between YSZ film and substrate in S-YSZ_R sample. The dashed lines show the interface and the grain boundary between two YSZ grains. The vertical lattice fringes of the left grain are not clearly resolved, because is not oriented exactly parallel to the $[1\bar{2}10]_S$ beam direction.

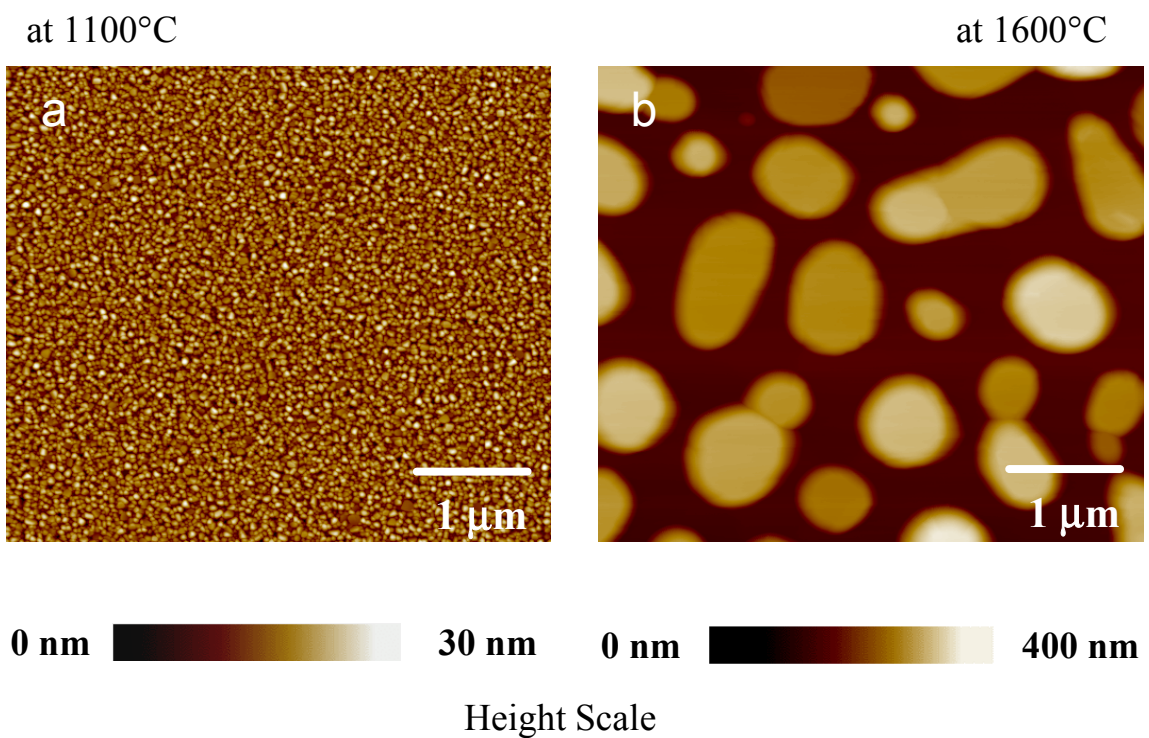


Fig. 5.32 AFM images from YSZ grains (spin coated) on the sapphire substrate after 1h heat treatment: (a) at 1100°C the film possess a mixed of [100] / [111] texture and (b) at 1600°C the grains reveals well developed [100} texture. The thickness of the film can be evaluated on the basis of the height scale below the images: for the S-YSZ_p sample annealed at 1100° C, the thickness is around 30 nm, and for the S-YSZ_p sample annealed at 1600° C, the grains achieve height of about 400nm.

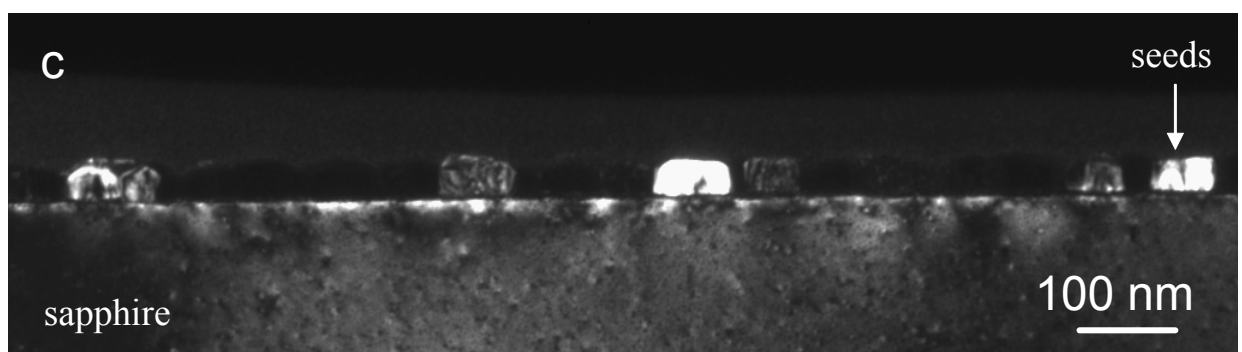
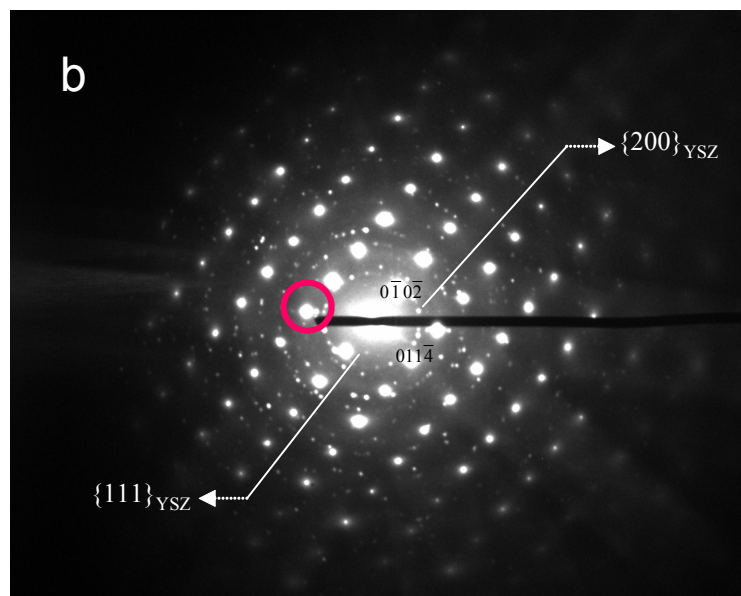
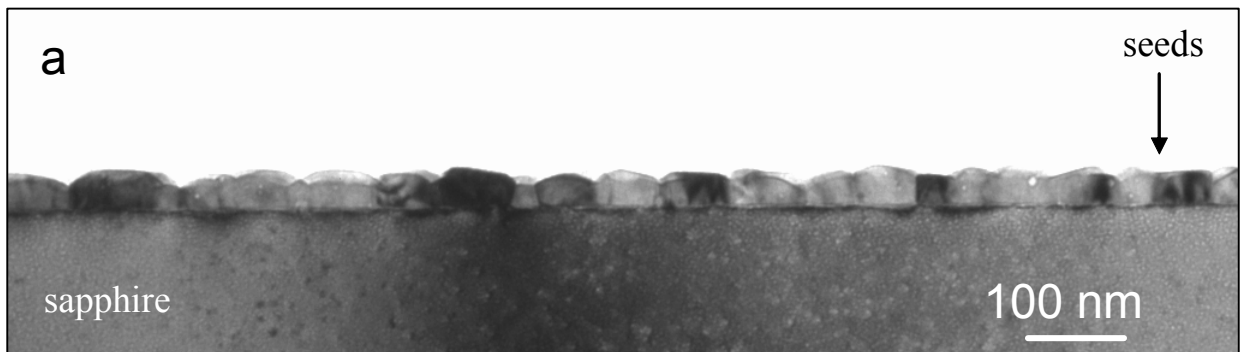


Fig. 5.33 TEM cross-sectional micrograph of YSZ seeds treatment at 1100°C for 1h. a) BF image; (b) diffraction pattern from the interfacial region between sapphire substrate and seeds; where the reflection from sapphire and YSZ polycrystalline are indexed in black and white, respectively (c) DF image recorded with the reflex showed above

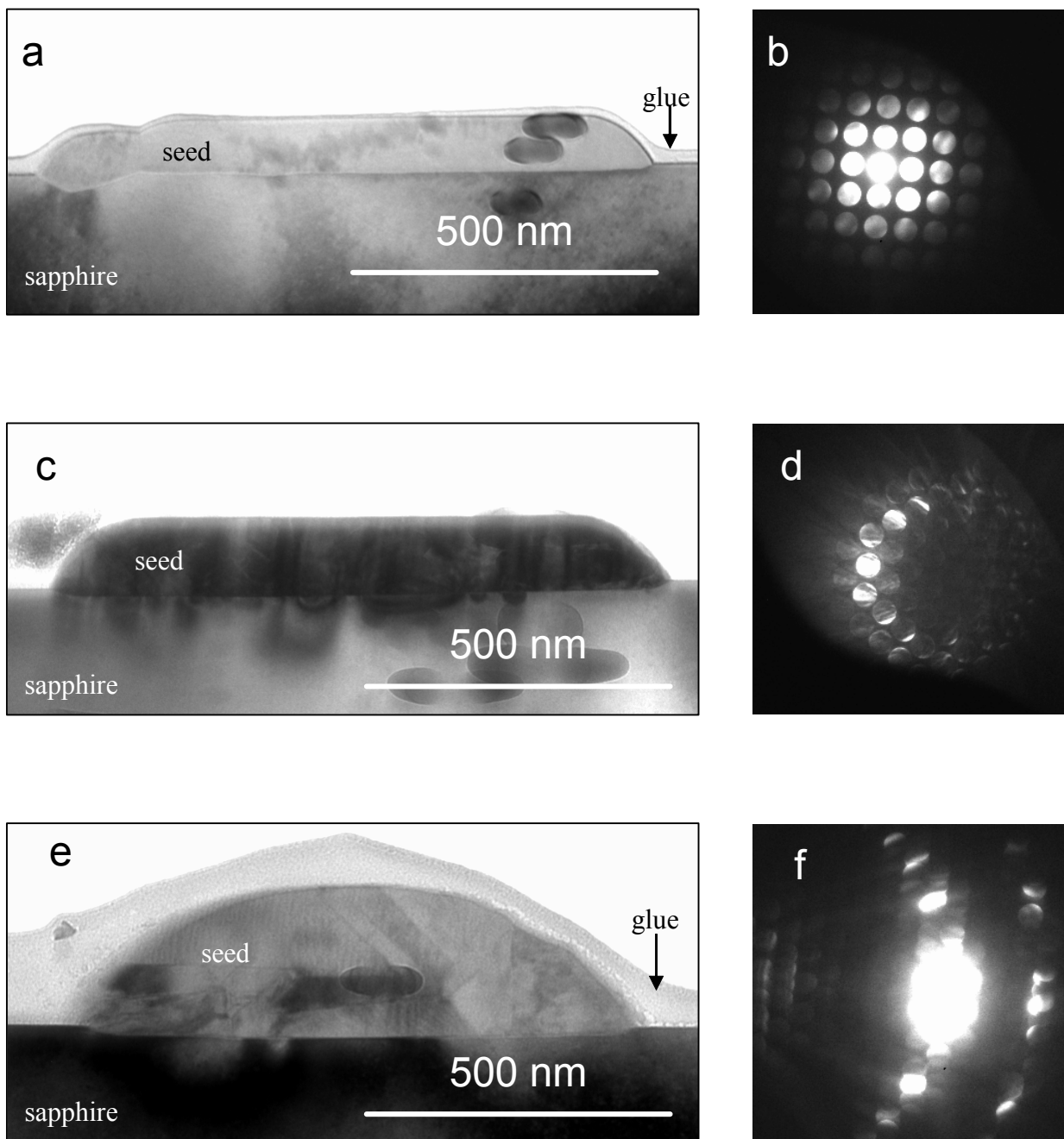
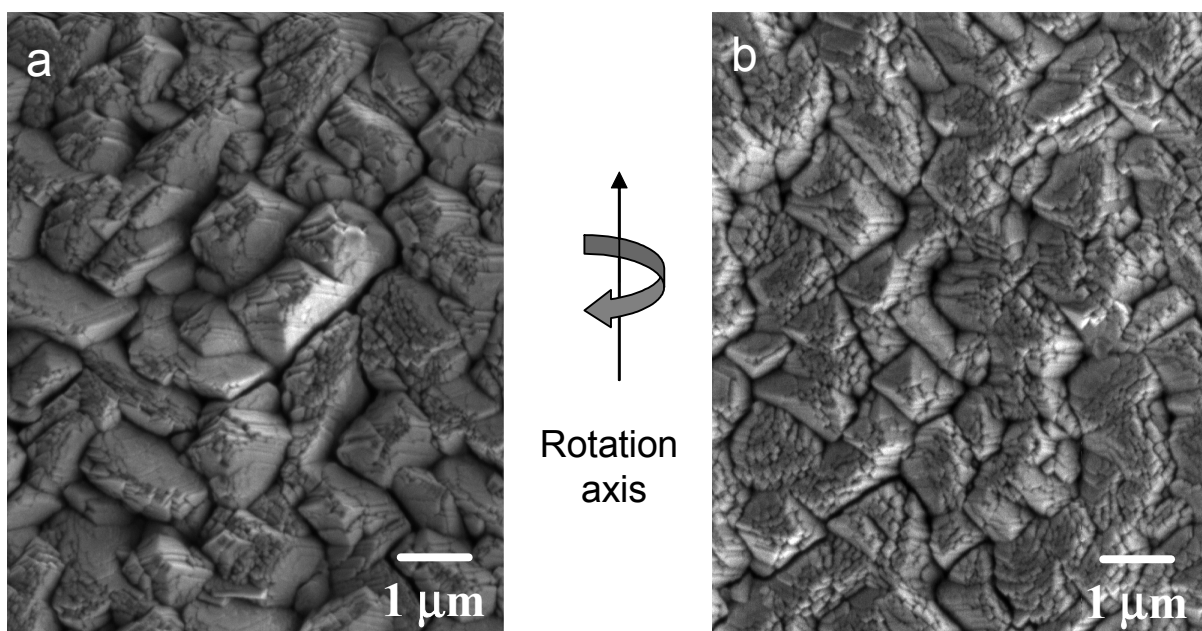
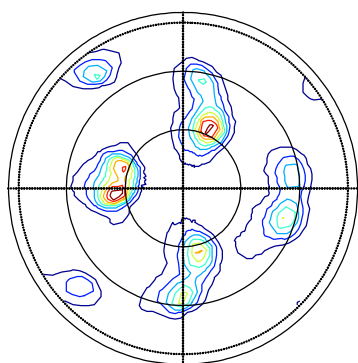


Fig. 5.34 BF TEM cross-sectional micrographs of YSZ seeds treatment at 1600°C for 1h and associated diffraction pattern showing the orientation of seeds to the sapphire substrate.

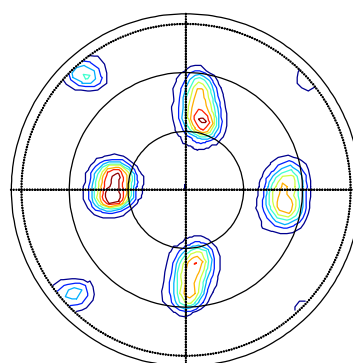


[311/100] texture

[100] texture



(c)



(d)

Fig. 5.35 SEM plane view and corresponding XRD measurements from SS-YSZ_R sample. (a) onto sapphire substrate with seeds annealed at 1100° C for 1h; (b) onto sapphire substrate with seeds annealed at 1600°C at 1h; (c) and (d) 202 pole figures corresponding to (a) and (b), respectively.

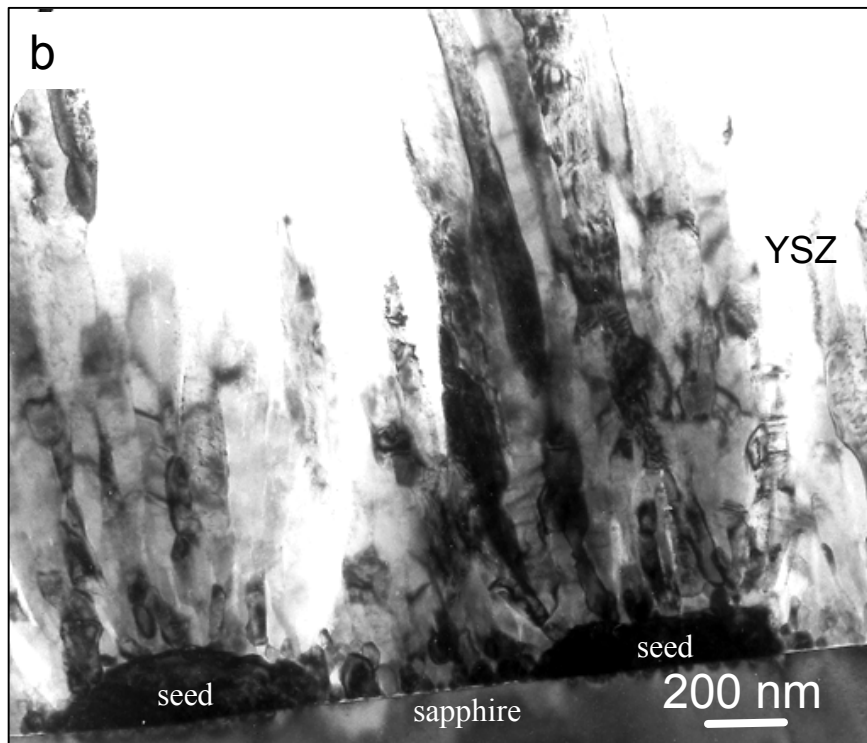
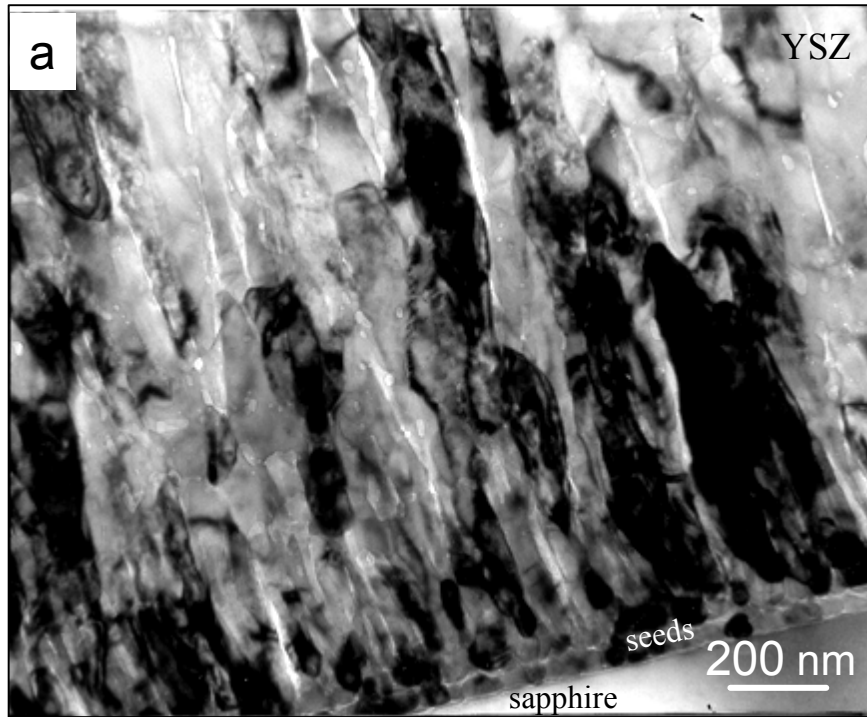


Fig. 5.36 BF TEM cross - sectional micrographs of SS-YSZ_R (a) with seeds treatment at 1100°C for 1h and (b) with seeds treatment at 1600°C for 1h.

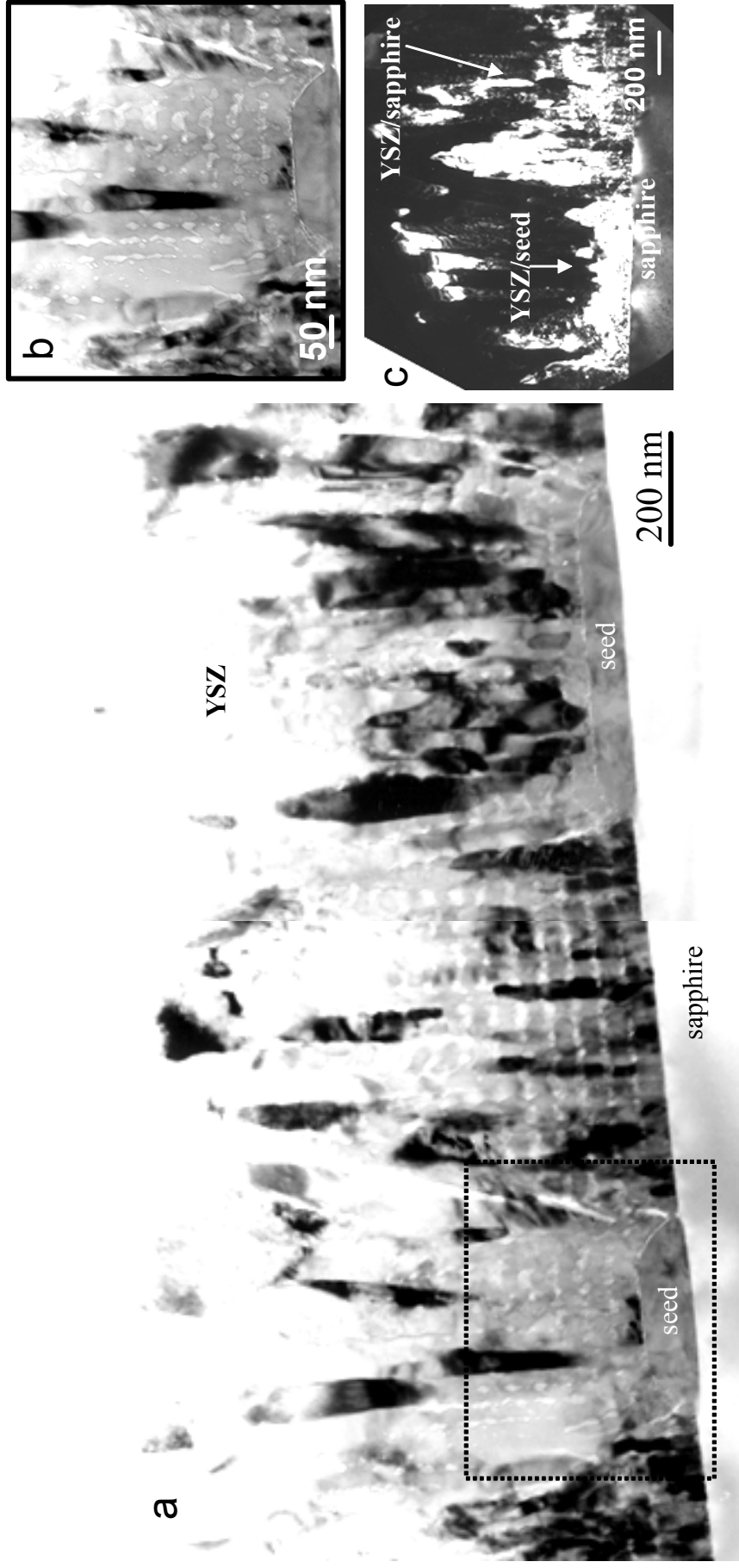


Fig. 5.37 a) BF TEM cross-sectional micrograph of SS-YSZ_R sample, where the seed were annealed at 1400° C for 15h. The EB-PVD coating is deposited at deposition rate ~0.3 μm/min; b) higher magnification of the seed selected in (a) with dashed line, where the highly aligned porosity is clear to see. The lines follows the curvature of the substrate i.e. the geometry of the seeds; c) DF TEM image showing the orientation relationship between YSZ and sapphire between two seeds and YSZ and seed (pointed by arrows).

5.5 Summary

The systematic series of experiments presented in this chapter provide information about the morphology and texture of the EB-PVD YSZ coatings. The preference is given on the microstructure of the YSZ/Sapphire interface. The results can be summarized as follows:

- YSZ TBCs deposited on stationary substrates resulted in a dense columnar microstructure with strong $\langle 100 \rangle$ fiber (out of plane) texture and roof-top morphology. The columns extend through the whole layer thickness with almost constant width. TEM studies reveal for many grains a preferred orientation relationship at the interface with $(0001)_S \parallel (100)_{YSZ}$ and $[10\bar{1}0]_S \parallel [001]_{YSZ}$. The HRTEM images reveal that many columns possess well defined orientation. No intermediate interfacial phase could be detected.
- YSZ TBCs deposited on rotated substrates yields a less dense, porous microstructure possessing additionally to the $\langle 100 \rangle$ out-of plane texture a strong in-plane orientation. The column tips have four-fold symmetry represented by pyramidal morphology. TEM analysis from the interfacial region confirm the in-plane orientation relationship with $(0001)_S \parallel (100)_{YSZ}$ and $[10\bar{1}0]_S \parallel [001]_{YSZ}$ yielding in the formation of three equally populated variants, which in total compose 83% of all grains. HRTEM investigations confirm the specific orientation of those specific oriented grains on the atomic level. The two materials do not react to form a third phase and show an atomically abrupt interface.
- YSZ TBCs deposited on seeded sapphire with rotating of the substrate show $\langle 100 \rangle$ texture (large seeds) and mixed from $\langle 311 \rangle / \langle 100 \rangle$ texture (small seed). The column tips possess the shape of quadrangular pyramids but without four-fold orientation, as observed for the YSZ deposited on bare sapphire under rotation. TEM study reveals that there is no preferred orientation relationship between the seeds and the columns.

6. Discussion

The results section of the present work documents a $\langle 100 \rangle$ fiber texture and a roof-top morphology for the YSZ deposited on stationary substrates, and a biaxially $\langle 100 \rangle$ texture with four-fold morphology for the coating deposited on rotating substrates. The results are found to be accompanied by the $(0001)_s \parallel (100)_{\text{YSZ}}$ preferred orientation of the grains to the sapphire for both stationary and rotated substrates. Large amount of YSZ grains (83% in case of the deposition on rotating substrates) with a specific orientation relationship $(0001)_s \parallel (100)_{\text{YSZ}}$ and $[10\bar{1}0]_s \parallel [001]_{\text{YSZ}}$ are observed in the interfacial region. HRTEM images show an atomically abrupt interface, where the two materials have not reacted to form a third phase.

The discussion section aims to correlate the observed morphology to the texture type of the TBC coating deposited on stationary and rotating substrates, respectively. It is focused on the development of the interface microstructure and examines reasons for the preferred orientation of YSZ TBCs to the sapphire substrate. The results are compared with the morphology and crystallographic orientation of TBCs on polycrystalline alumina observed by other authors. The influence of seeded layers on the growth of YSZ TBCs is also discussed.

6.1 Morphology and texture

Under the conditions of kinetically constrained growth (limited diffusion of adatoms on the depositions surface) occurring during TBC deposition, stable columnar growth requires that each of the faces comprising a column tip receives equal amounts of vapor flux [01Ter]. Unfavorable column tip morphologies (and thus growth directions) which do not satisfy the conditions of equal amounts of flux will be screened out by evolutionary selection, as discussed in Section 2.3. Thus, concurrent with the growth of columnar TBC grains is the evolution of crystallographic texture.

The textures observed for EB-PVD TBC are strongly influenced by the processing conditions where temperature and direction of the vapor flux play a key role [01Ter]. Observations by [96SFP, 96SOB, 99TLL, 00ScS, and 01Ter] show that for PVD the dominant direction during film growth is the pattern of vapor incidence. The orientation obtained in this case is characterized by an out-of-plane fiber texture. As observed by *Terry* [01Ter] (see Ch. 2.3) the column tip morphologies always possess $\{111\}$ active growth facets in agreement with the periodic bond chain analysis predicting the $\{111\}$ planes to be dominated during growth of

fluorite structure. The symmetric arrangement of $\{111\}$ facets with respect to the incidence vapor flux allow the potential for columnar growth in the $\langle 100 \rangle$, $\langle 110 \rangle$, $\langle 111 \rangle$, and $\langle 311 \rangle$ directions, respectively. The presence of these type columns in a thick TBC film will be dependent upon which of these types grows fastest under a given combination of temperature and pattern of vapor incidence.

YSZ deposited on stationary substrates, which are oriented normal to the vapor flux, shows columnar grains that grow perpendicular to the substrate surface and extend through the entire coating thickness with almost constant width. The YSZ columns grow on stationary sapphire substrates under normal incidence flux (Fig. 5.2) reveal a $\langle 100 \rangle$ out-of-plane orientation. A fiber texture is common for PVD on a stationary substrate because the vapor flux defines only one preferred orientation. However, development of a $\langle 100 \rangle$ fiber texture is not observed in cases of YSZ TBC deposited on stationary metallic substrates with polycrystalline alumina surface produced by oxidation. For example, the fiber texture reported by *Terry* [01Ter], for TBCs on preoxidized FeCrAlY substrates, deposited at $T_s = 1000^\circ\text{C}$ and under conditions of normal vapor incidence is a mix of $\langle 111 \rangle$ and $\langle 101 \rangle$ column growth directions. This, clearly suggests an influence of the sapphire substrate on the selection of a $\langle 100 \rangle$ growth direction in the present coatings.

The growth of columnar grains on the rotating substrates can be explained through the evolutionary selection mechanism previously discussed. At elevated temperature the cross-section micrographs of S-YSZ_R (cf. Fig. 5.15 and Fig. 5.24) suggest an increase in the columns diameter with increasing coating thickness. The increase in columns width is a consequence of the competitive growth, discussed in the Section 2.3. Grains with crystallographic orientations unfavorable for columnar growth are screened out, making room for a gradual increase in diameter of more favorable oriented grains. The surviving grains possess a column $\langle 100 \rangle$ growth direction and a four-fold arrangement of $\{111\}$ habit facets and this symmetry is represented by the column tip morphology (cf. Fig. 5.13), where the diagonal of the pyramid is parallel to the axis of substrate rotation. The appearance of this type morphology, which is observed only under conditions of substrate rotation, is explained by *Terry* [01Ter] wherein alignment of the column tips in the plane of the coating results from the requirements that all facets capture equal amount of flux. This condition is possible because boundaries of $\langle 100 \rangle$ tips lay in the plane of the coating and are coincident with one another so that condensation on the column sides is minimized during rotation (see Fig. 2.8 in Ch. 2.3). Observations of a four-fold symmetry and $\langle 100 \rangle$ texture orientation agree also with the

results by *Schulz et al.* [96SFP, 96SOB, and 00ScS]. The authors explained the observed symmetry for all YSZ TBC deposited on a polycrystalline TGO with the shadowing effect but did not elaborate the mechanism.

Since continued growth of TBC on rotating substrates (polycrystalline or/and single crystal alumina) resulted in the development of a $\langle 100 \rangle$ in-plane crystallographic texture, it is reasonable to assume that the influence of the substrate is overshadowed from the evolutionary selection that becomes dominant with increasing coating thickness. The question remains as to the specific orientation of the columns at the interface for both S-YSZ_S and S-YSZ_R samples and what might cause the observed $\langle 100 \rangle$ texture orientation for S-YSZ_S. This will be addressed in the upcoming sections.

6.2 Orientation Relationship at the Interface

As discussed above, the YSZ EB-PVD coatings consist of columnar grains growing perpendicular to the substrate surface. The columnar grain morphology develops through the constrained growth from randomly oriented nuclei as reported by *Terry* [01Ter]. Random orientation of these initial grains with respect to the substrate normal will occur simply as a result of the TGO roughness.

The early stages of TBC deposition (see Section 2.3) on polycrystalline alumina TGO was discussed by *Unal et al.* [94UMH], *Meier et al.* [99SYT], and *Schulz et al.* [96SOB, 00ScS]. The authors observed the formation of a mix zone containing fine, randomly oriented grains from α -Al₂O₃ and YSZ. There was no evidence that the substrate influences the appearance of the fine-grained, texturless zone. Since continued growth resulted in the development of a crystallographic texture, it can be interpreted that the growth is governed by evolutionary selection and that texture of rotated EB-PVD TBC is controlled by growth rather than by nucleation.

The TEM studies in the present work are the first to reveal that in the case of TBC deposition on stationary sapphire substrates the grains possess a preferred orientation at the interface, which is significantly different from those deposited on polycrystalline substrates.

The diffraction patterns from the interfacial region (see Fig. 5.7a and Fig. 5.11a) present both reflections from sapphire and YSZ. All columns possess an out-of-plane orientation with $(0001)_S \parallel (100)_{YSZ}$, where the grains are randomly rotated around the normal of the surface plane. This is in agreement with the XRD results, which show a strong $\langle 100 \rangle$ fiber texture. The overlap of the DPs reveals that these particular columns have an additional in-plane

orientation. However, the patterns reveal that a preferred orientation relationship exists at the interface between the sapphire and YSZ. The DPs recorded at a larger distance to the interface with the same sized SAD aperture shows that only the reflection corresponding to the $\langle 100 \rangle$ texture component remain dominant. The lateral streaks caused by grains that belong to the $\langle 100 \rangle$ texture, but which are randomly rotated around the normal of the surface plane, are not visible. The changes in DPs from the interface to the regions at a distance of about 1 to $3\mu\text{m}$ can be explained with the changes in thickness of the TEM sample. Figure 6.1 presents a schematic illustration of how the sample thickness changes with the distance to the hole (see also Fig. 3.2 and Fig. 3.3 in Ch. 3).

With increasing distance from the substrate the thickness of the samples decreases. Near to the edge of the sample (near to the hole) the polycrystalline layer becomes thinner. The Moiré fringes, which are caused by an overlap of the grains with a different orientation, are not visible in the edge region. Although, the same size of SAD aperture was used, the actual number of grains contributing to these DPs is less than in the regions near the interface. This could explain why the lateral streaks disappear or become less pronounced and only the $[100]$ systematic row reflections caused by the $\langle 100 \rangle$ texture component remain dominant. The pattern with arc-shaped spots results from the overlapping of individual spots generated from grains which belong to the $[100]$ zone axis, but which are slightly tilted relative to each other. The thin edge of the YSZ layer caused by sample preparation is bended, which can be seen in Figure 6.2. The bending occurs in plane primarily perpendicular to the TEM foil. Since the diffraction patterns have been taken under an angle of 30° part of the bending is visual in the diffraction pattern as a small elongation of the diffraction spots from the originally circle geometry. However, because of the fact that the TEM sample is very thin and only a small area can be observed compared to XRD measurement which contain more averaged information, the following can be concluded: YSZ TBC grow with a preferred (100) orientation on the (0001) sapphire substrates, which is evidenced by DP and DF studies, XRD texture measurements, and observed surface morphology.

The diffraction pattern of YSZ recorded from the interfacial region for the S-YSZ_R samples (Fig. 5.26a) shows the same features. Reflections from sapphire and YSZ are aligned which is an indication for a preferred orientation relationship between film and substrate. In the region near the interface ($\sim 1\mu\text{m}$ from the substrate, Fig. 5.27a) the diffraction patterns from YSZ contains similar features as those obtained from the same region of the S-YSZ_S sample. All columns contributing to this image have the same $[100]$ zone axis. In contrast to the sample S-YSZ_S, diffraction pattern from YSZ recorded at the large distance from the interface

(Fig. 5.27c) exhibit the same features as those observed near the interface. Even more, the parallel strikes disappeared, which reveals that the in-plane orientation becomes stronger. These results confirm the SEM top views (Fig. 5.12) and XRD results (Fig. 5.13), which reveals a four-fold symmetry.

For both coatings deposited on stationary and on rotated substrates, the SAD patterns from the interfacial region show preferred out-of-plane and for large amount of grains additional in-plane [100] crystallographic orientation. In addition, the average diameter of the columns in the interfacial region (Fig. 5.4a and Fig. 5.24), is approximately the same in both samples. This together with the fact, that the deposition conditions like substrate temperature and chamber pressure are with the same value, it may be assumed that the initial stages in the growth process for both stationary and rotating conditions is identical.

Based on the values of the activation energy of the process, *Movchan et al.* [69MoD] assume that the condensation of the zirconium dioxide film in Zone 2 (Fig. 2.6) is formed by the nucleation and growth of islands. The process of “surface recrystallization”, which may occur, consists in the coalescence of two neighboring, differently oriented islands. The result is a island which adopts one of the original orientations. This may explain the agglomerates of grains observed in the DF-images in the region at/near the interface for S-YSZ_R sample. The irregularly shaped grains, which appear bright in Figure 5.22 (plane view sample), can be linked to the bundles of columns in Figure 5.28 (cross-section), which appears bright because of their specific orientation relationship to the substrate.

It was discussed in the previous paragraph, that the initial growth process may be identical for both stationary and rotated deposited films. Therefore, this kind of approach should be also used in the case of S-YSZ_S sample. The micrographs in Figure 6.3 show the bright-field and corresponding dark-field images which were taken with the reflection perpendicular and parallel to the substrate normal, respectively. The distribution of well oriented columns relative to the sapphire substrate corresponds to variants 1 and 3 on the schematic illustration in Figure 5.21. The micrographs reveal two distinct differences compared to the S-YSZ_R sample: (1) well oriented grains are generally separated and do not form bundles as in the case of the rotated sample, (2) the bright contrast of well aligned columns in dark-field micrographs extends into the coating, further away from the interface than under rotated conditions. The first difference indicates that grains exist which nucleate in a preferred orientation, but owing to the continuous flux the initially thin film cannot undergo grain growth which might be accompanied by a further texture development. In contrast, by the rotation of the substrate (Fig. 6.4), YSZ grains spend longer time at elevated temperature than

in S-YSZ_S sample. The reorientation of the grains through grain boundaries migration can continue to some extent during the “night” time, in which no flux impinges on the substrate (Fig. 6.5c). The second layer of the film, deposited during the second revolution, follows those orientations and during the subsequent “night” time further reorientation and secondary grain growth can occur (Fig. 6.5e-f). During the next revolution steps the influence of the geometrical down selection due to shadowing gets more prominent and takes the control (Fig. 5h). From the primarily 3 main variants remains only one, in which the grains with column tip morphologies satisfy the equal amounts of flux, i.e. which are oriented parallel to the axis of substrate rotation (see Fig. 2.8, Section 2.3). In the case of deposition on the stationary substrate where the substrate is always exposed to the vapor flux (no rotation), no such external effect takes place and the columns grow uninfluenced with the same orientation (Fig. 6.5d and Fig. 6.5g).

As shown by *Lange et al.* [91MLa and 94CaL] the need for a substrate of similar crystal structure and lattice parameters is not a necessary requirement for forming an epitaxial thin film. The [100] epitaxial growth of YSZ on basal plane sapphire substrates is explained due to a special orientation relationship leading to a low interfacial energy that may exist between dissimilar structures. YSZ has a face-centered near cubic fluorite structure which may be viewed as a cubic close packing of zirconium and yttrium cations with oxygen anions occupying every tetrahedral interstitial site. The +3 valence of the yttrium cations is compensated by the introduction of oxygen vacancies. Sapphire on the other hand, has a rhombohedral structure commonly described with a hexagonal unit cell and may be approximately viewed as a hexagonal close packing of oxygen anions with aluminum cations occupying 2/3 of the octahedral interstitial sites. These materials have no apparent common planes or sublattice orientations of closely matching structure and do not react to form a third phase as observed by HRTEM (Fig. 5.12 and Fig. 5.29). The mechanism suggested by *Lange et al.* [91MLa and 94CaL] describes how grains within the polycrystalline film undergo normal grain growth until they form a columnar microstructure. The columnar grains with a lower interfacial energy due to a special orientation will undergo abnormal growth and consume other grains. Although a single normal orientation may exist: $[001]_{\text{YSZ}} \parallel [0001]_{\text{S}}$, grains can have different in-plane orientations due to the different symmetry operations between the film and the substrate. The three in-plane YSZ orientations, each rotated by 120° about the c-axis of the sapphire, are related by the threefold rotational symmetry of the substrate. The $[001]_{\text{YSZ}} \parallel [0001]_{\text{S}}$ orientation development was also found by *Mazerolles et al.* [86MMP] to be the favored during the slow solidification of pseudo-binary eutectics of ZrO₂

(Y₂O₃) / Al₂O₃, implying that this is indeed a low energy interface. The observation of more than one epitaxial orientation as suggested by [94CaL] is due to the small difference in total interfacial energy between these orientations and/or the kinetics of the exclusive growth of the lowest energy interface is limiting.

However, the determination of the in-plane orientations done by [94CaL] were carried out for specimens prepared by the solution precursor route and heated for 50h at 1500°C, where all yttria stabilized cubic zirconia grains were isolated islands, and were expected to have achieved their lowest free energy configurations. In the present work, the YSZ (tetragonal phase) film with a 20μm thickness is EB-PVD deposited with a high rate of 0.3μm/min, at 1000°C temperature, and a chamber pressure of ~0.4mtorr. The difference in lattice parameter between cubic and tetragonal phase is less than 2% (see Ch. 2.1), but there is a significant difference in the deposition conditions. At these fast growth conditions, one might expect that the equilibrium orientations (relative to the substrate) could not be developed for all YSZ grains. That could explain the present results where in the interfacial region not all of the grains deposited under rotating conditions have an epitaxial orientation to the substrate. However, the fact that 83% of the YSZ columns (in the second layer) do have one of the preferred orientations can have two implications: (1) many grains start already as well oriented nuclei, (2) the surface and/or interface diffusion is so fast, which enables the reorientation of the nuclei.

Moreover, to achieve the equal film thickness, the S-YSZ_R persists about three times longer under high temperature compared to the S-YSZ_S sample. It might generally be expected that in the case of the rotating substrate the grains which have preferentially orientation due to the lower interfacial energy would have more time than those on the stationary substrate to grow and to consume the other oriented grains. This can explain the result that in the case of S-YSZ_R the number of well oriented grains near the interface is higher than those in case of S-YSZ_S.

Unfortunately for the S-YSZ_S sample an equivalent plane-view analysis was not possible since large stresses in the sapphire (Fig. 6.6) impede the TEM sample preparation. Nevertheless, cross sectional analysis revealed that well oriented columns exist in all three equivalent directions. The recall of the results for surface morphology and XRD (for both S-YSZ_S and S-YSZ_R samples) suggest the following model: In both cases YSZ growth begins with preferred (out-of plane) oriented nuclei, some of them possess additionally a preferred in-plane orientation. Since the TBC deposition occur in conditions of constrained growth, where the surface diffusion is limited, it could be interpreted, that the sapphire substrate

promotes nucleation of grains well oriented onto sapphire. During the continuous vapor flux the grains formed from these nuclei grow with the same orientation, which result in $\langle 100 \rangle$ fiber texture. In case of deposition on rotating substrates the rearranged of the grains caused agglomerates with preferred orientation to the substrate. At/near the interface, 83% of the grains belong to the 3 main variants and possess a specific orientation relationship. The other 17% are grains which do have a preferred out-of plane orientation, but they do not belong to these variants. However, with increasing coating thickness, the evolutionary selection mechanism becomes dominant and only one variant, of those three main variants, remains: the variant in which the grains with column tip morphologies satisfy the equal amounts of flux, i.e oriented parallel to the axis of substrate rotation. Thus, growth of the columns resulted in morphology with a strong in-plane orientation.

6.3 Interface Microstructure

In the case of epitaxial growth, the periodicity and symmetry of the substrate lattice provides interface-energy anisotropy for in-plane orientations of the grains. It is possible that steps or other substrate surface defects can lead to preferred in-plane orientation. HRTEM images for both S-YSZ_S and S-YSZ_R samples show clearly resolved lattice fringes of the two materials. In both micrographs no reaction layer is observed. In case of S-YSZ_S (Fig. 5.12) in the near interface region, the HRTEM images showed distortion of the Al₂O₃ and ZrO₂ lattices, the interface is rough and contains many steps, which originate from the (0001)_s surface preparation. In comparison, the HRTEM image from the S-YSZ_R sample (Fig. 5.29) shows an abrupt interface with fewer defects. The epitaxial orientation relationship between YSZ film and alumina substrate: $[0001]_s \parallel [100]_{\text{YSZ}}$ can also be observed.

The coincident site lattice principle can be used to help understand why two lattices form frequently observed interfaces *Balluffi et al.* [82BBK]. The model in Figure 6.8 represents the geometrical description of forming an interface between Al₂O₃ and YSZ crystals based on the principle of the near coincident site lattice (NCSL). A two-dimensional model is considered, where alternations of planes with metal ions and oxygen ions is preserved across the interface. By this choice the Al₂O₃ substrate is assumed to terminate with O ions (red circles) and the deposited film to start with Zr ions (black circles). The lattice constants for 7wt% YSZ were interpolated from X-Ray data, which were available for 3mol% YSZ and the range between 10-18mol% YSZ (Fig. 6.7). In the $[10\bar{1}0]$ direction site coincidence is observed every 13th zirconium ion and correspondingly every 14th alumina oxygen ion. In the $[1\bar{2}\bar{1}0]$ direction

the oxygen distance is roughly half the one of Zr ions. But here the site coincidence appears already every 7 zirconium and 13 alumina oxygen ions, respectively. The planar crystal lattice cell for ZrO_2 and Al_2O_3 are presented with black and red lines respectively. In high resolution TEM only the projection along atom columns is detectable. Therefore the visible periodicity is reduced by a factor of two, as indicated by the dashed lines.

The geometrically calculated matching of the two lattices is in close agreement with the interfacial contrast features observed in the HRTEM images, presented in Figure 6.9. A typical HRTEM micrograph recorded along the $[10\bar{1}0]$ zone-axis of sapphire is shown in Figure 6.9a. The correspondingly fast Fourier transformation (FFT) filtered image of the selected part of the HRTEM micrograph (Fig. 6.9b) shows the misfit dislocations at the interface. Between the inserted lattice planes the interface structure is coherent. The distance between two misfit dislocations corresponds to approximately 13 to 14 lattice (200) planes within this image. The distorted areas due to the inserted lattice plane are highly localized. Thus, the Al_2O_3/YSZ interface exhibits a semi-coherent structure in this direction. However in the $[1\bar{2}\bar{1}0]_s$ zone-axis orientation the interface between Al_2O_3 and YSZ exhibits a more coherent structure. The model in Figure 6.8 shows that on average the initial distance between oxygen ions and the nearest Zr ions is less in this direction which is a result of the smaller distance of oxygen ions. This may explain the less stress contours at the interface in this viewing direction (Fig. 5.25). Preliminary calculations based on electrostatic potentials show that in the $[1\bar{2}\bar{1}0]_s$ direction the interfacial energy has a much sharper minimum with respect to the translation state of the two crystal half than in the other $[10\bar{1}0]_s$ direction [Stefano Fabris, private communication]. This implies again the better geometrical fit for the $[1\bar{2}\bar{1}0]_s$ direction.

It could be concluded that the given interface between YSZ and sapphire has a large amount of coherency, on one hand side due to the relative small lattice-constant mismatch between YSZ and sapphire along the $[1\bar{2}\bar{1}0]_s$ direction and on the other hand due to the small core size of the misfit dislocations along $[10\bar{1}0]_s$.

6.4 YSZ Growth on Seeding Layers

As was described earlier a liquid precursor method can be used to form highly oriented thin films in material systems with dissimilar crystal structures and interatomic spacing. The present study was undertaken with the objective of using these films as templates to produce highly textured and well oriented YSZ thin films by inducing two dimensional grain growth,

the idea being that grains having special interfaces with low energy will grow at the expense of other grains. The remnant grains should act as seeds ultimately leading to the growth of a highly oriented EB-PVD deposited YSZ film.

The microstructure of the precursor derived film developed after 1h heat treatment at 1100°C reveals small YSZ grains with [111]/[100] texture. In the DF images, only some of the grains appear bright under the same diffraction conditions as the substrate offering an evidence of their epitaxial orientation. Additional heat treatment promotes the break-up and further orientation of the film. At 1600°C the film consists of a single layer of grains. The XRD observations show that the grains reveal a [100] preferred orientation to the sapphire. This suggests that the thin film breakup process has effectively removed those grains which are not in the [100] orientation by the mechanism described by *Thompson* [90Tho]. Electron diffraction analysis showed that most of the individual grains are tilted about several degrees from the perfect epitaxial orientation relationship to the sapphire. This property hampers the originally intended investigation of a global templating effect.

Both coatings, deposited on the small seeds- and on the larger seeds-substrates under rotating conditions, possess a preferred in-plane orientation, as determined by XRD. Although the deviation from the XRD results observed for the S-YSZ_R are significant. This effect appears also in the morphology of the coating. The column tips possess the shape of quadrangular pyramids but without four-fold orientation, as observed for the YSZ deposited on bare sapphire. The XRD results for the YSZ deposited on larger seeds, reveal [100] texture and sharper in-plane orientation compared to those deposited on the smaller seeds, where the texture is mixed from [311]/[100]. From the surface morphology and XRD-results might be concluded that the templating effect from the seeds on the growth of YSZ is negligible.

The cross-sectional TEM observations show that the columns are irregularly in form and diameter and not parallel over their length as was observed for the coating deposited on a bare sapphire. The deposition parameters in these cases are quite different compared to those used for the deposition on the bare sapphire: a higher rate (~1.2µm/min) and a higher pressure (6.0mtorr). However, as it is discussed by *Thornton* [77Tho], the gas pressure is one of the parameters which influences the microstructure of PVD layers in Zone 1, but has little influence on the structure at high temperatures typical for Zone 2. Thus, the variations in the deposition rate could be one of the reasons for the observed changes in the column microstructure. Comparison between two TEM images Figure 5.36 (YSZ deposited at ~1.2µm/min) and Figure 5.37 (YSZ deposited at ~0.3µm/min) provide evidence to this suggestion. The coating deposited at slower rate (the same as for the S-YSZ_R) shows

columnar structure similar to that observed for the S-YSZ_R. In the area between two neighbor seeds (bare sapphire), the SS-YSZ_R coating reveals even the same microstructure as this in the S-YSZ_R sample.

However, the coating on the top of seeds (Fig. 5.37) possesses a bunch-like structure, which suggests an influence of the surface of the seeds. In the TEM micrographs (Fig. 5.36) from the interfacial region, the seeded surface appears rough. The high perfection of the smooth sapphire substrate is missing in this case. This affects the initial stages of the film growth. The YSZ columns follow the geometry of the seeded surface forming a bush-like structure. Additionally, the DF study reveals that there is no preferred orientation relationship between the seeds and the columns. This result is unexpected considering the observations by *Miller et al.* [93MCC], where a layer of epitaxial ZrO₂ (3-40mol% Y₂O₃) film has formed on the substrate of single crystal (100) oriented ZrO₂ (9.5mol% Y₂O₃) using an aqueous precursor method. Since the epitaxial growth may be sensitive to defects and substrate contamination, a possible explanation for the unusual results can be some organic contamination, which is formed on the seeded surface during the crystallization of the precursor. Clear evidence for this influence could not be found: The analysis of a possible Si contamination is very difficult since in the EDX signal the K-peak of Si and the L-peaks of Y and Zr overlap due to the low energy resolution of the EDX. Testing the quantitative analysis with nominal pure YSZ showed that even for this material unrealistic high values of a Si content were measured. On the other hand the present results confirm to some extent the measurements by *Clarke et al.* [01HLC] on the crystallographic texture of 7-wt% YSZ coatings deposited by EB-PVD under stationary conditions at different temperature on (100) single crystal ZrO₂. These results reveal that the coatings exhibited a <100> texture at both 1050°C and 1150°C temperature but no preferred in-plane orientation.

In conclusion, the experimental results indicate that the intended templating effect is rather weak. One reason might be that the starting texture of the seeds was not ideal enough to produce a pronounced effect. The results clearly show the influence of the surface shape. Even small deviations from a flat surface lead to a strong distortion of the columnar TBC structure. Nevertheless the final columnar growth and the general character of the morphology of the coating is achieved irrespective of whether the surface is rough or mismatched, showing the dominant influence of the geometrical shadowing effect through the substrate rotation.

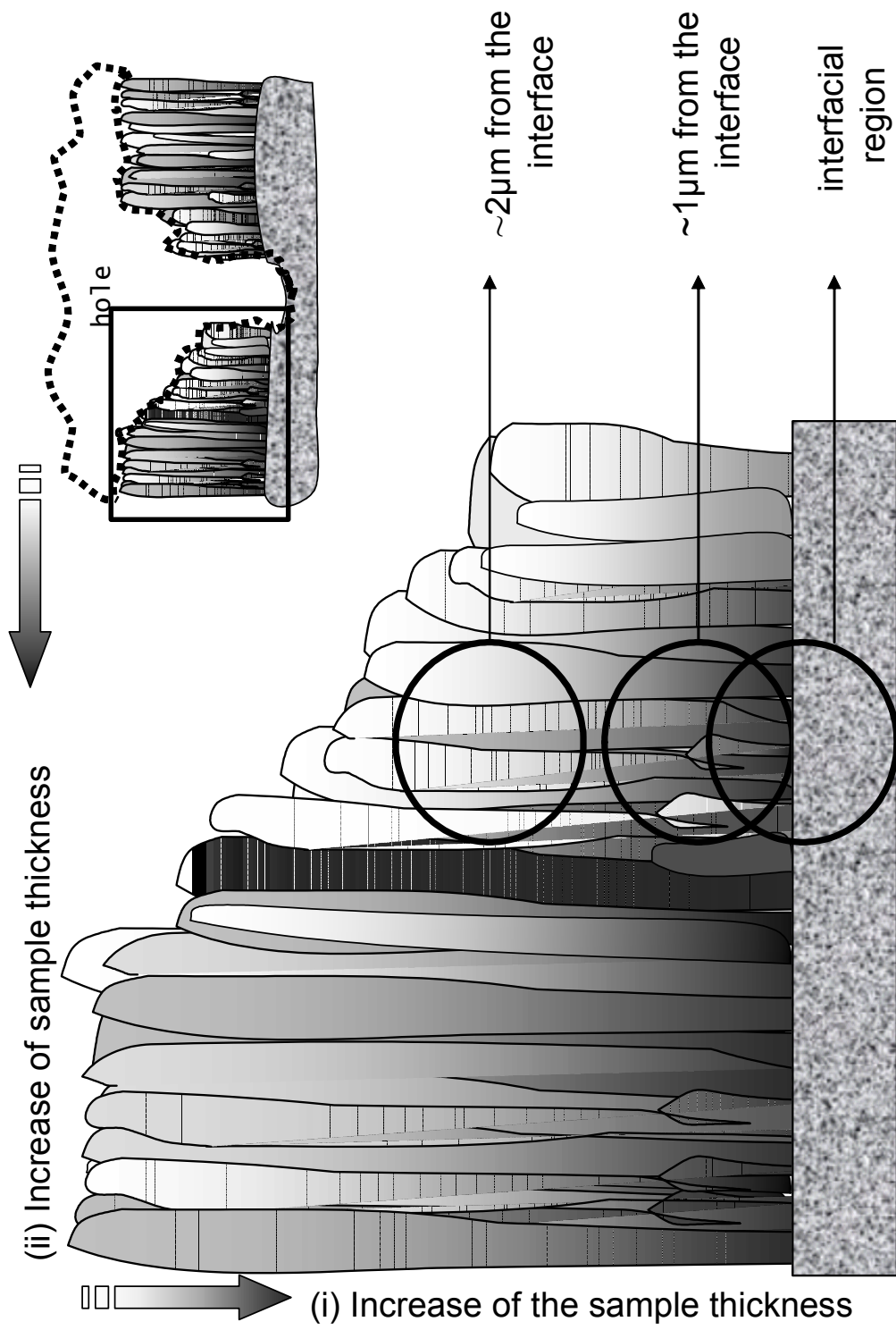


Fig. 6.1 Schematic illustration showing: the thickness of TEM sample decreases with (i) increasing distance from the substrate and (ii) decreasing distance from the hole. The positions of the SAD aperture at the places where the diffraction patterns were recorded are marked by circles.

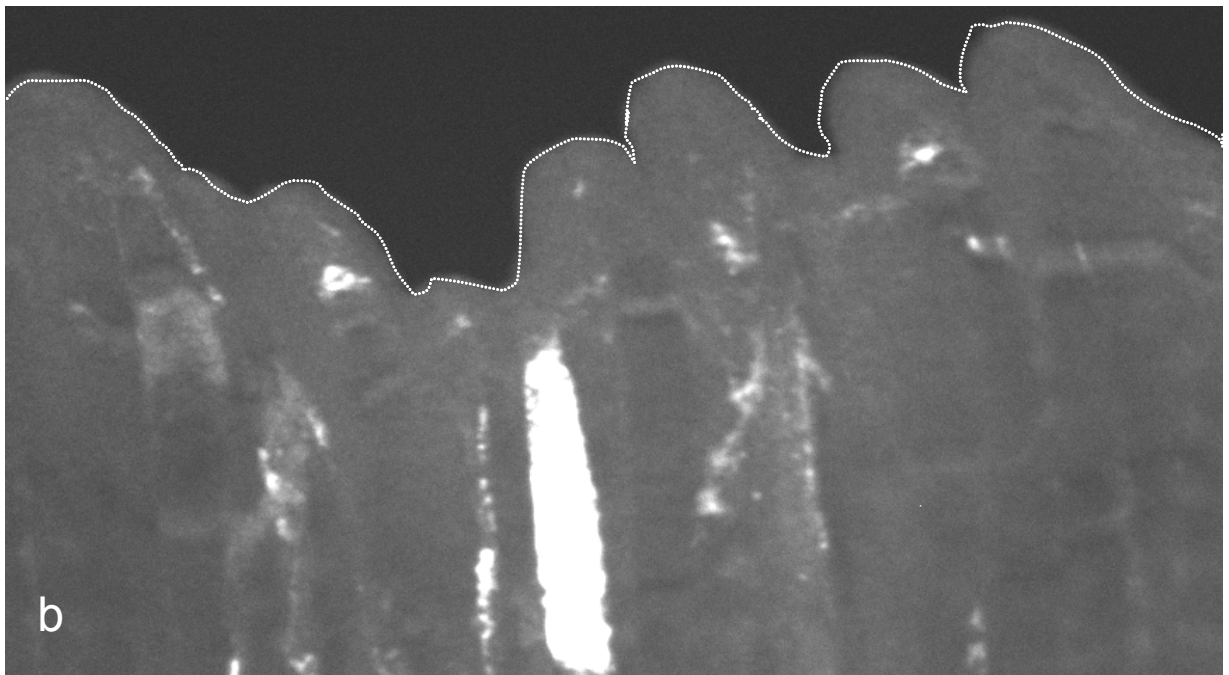
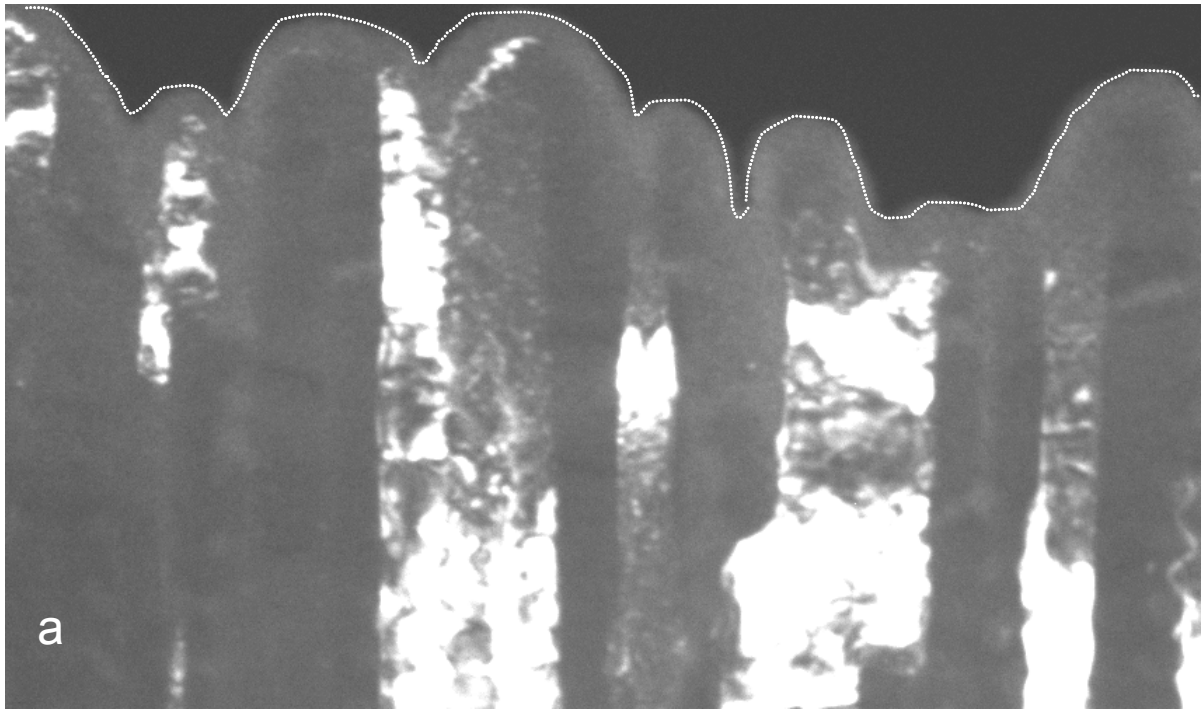


Fig. 6.2 a) DF micrographs of YSZ columns (S-YSZ_R sample) taken in $[10\bar{1}0]_S$ view direction and b) after tilting the sample of -30° , where the bending of the of the columns is clearly to see.

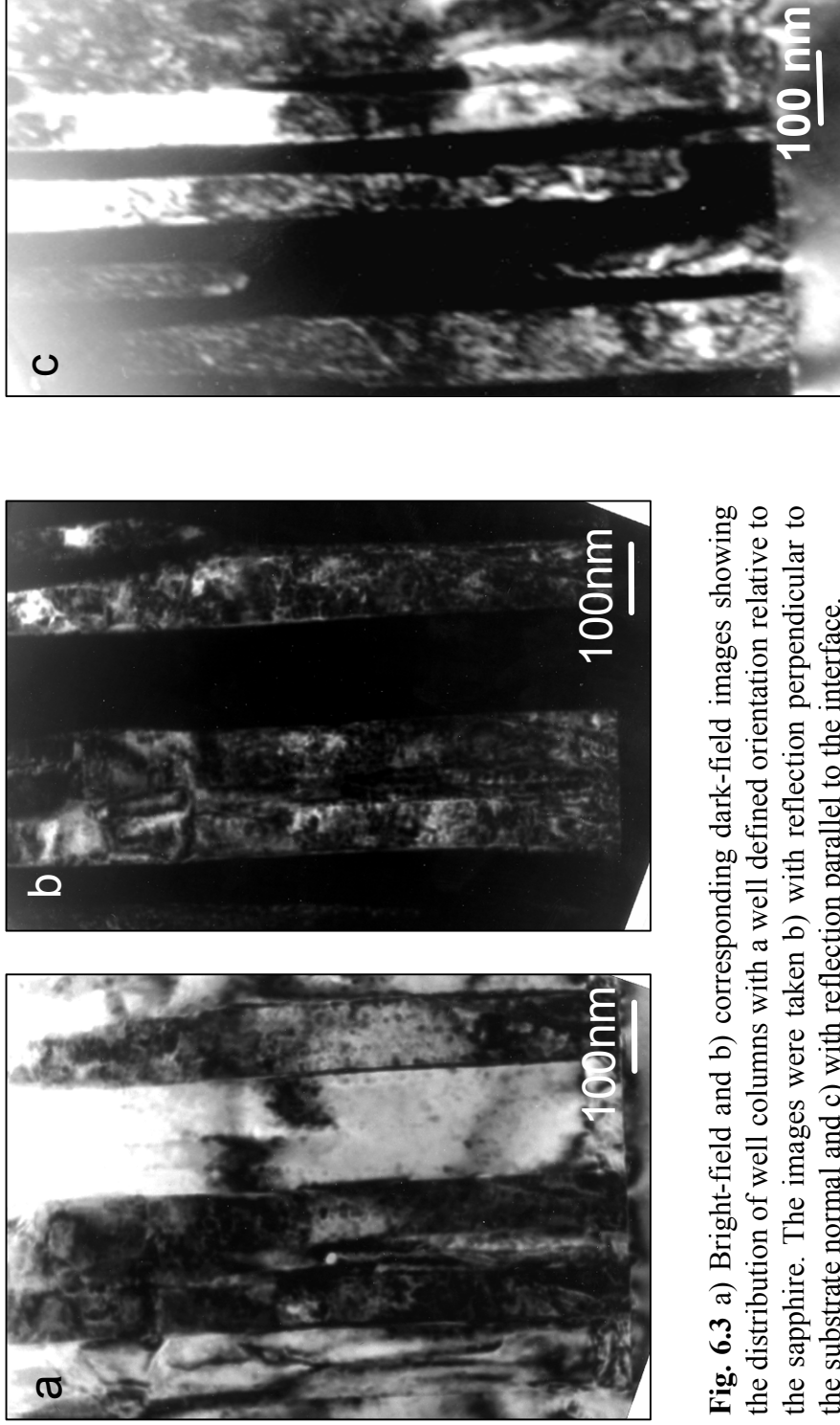


Fig. 6.3 a) Bright-field and b) corresponding dark-field images showing the distribution of well columns with a well defined orientation relative to the sapphire. The images were taken b) with reflection perpendicular to the substrate normal and c) with reflection parallel to the interface.

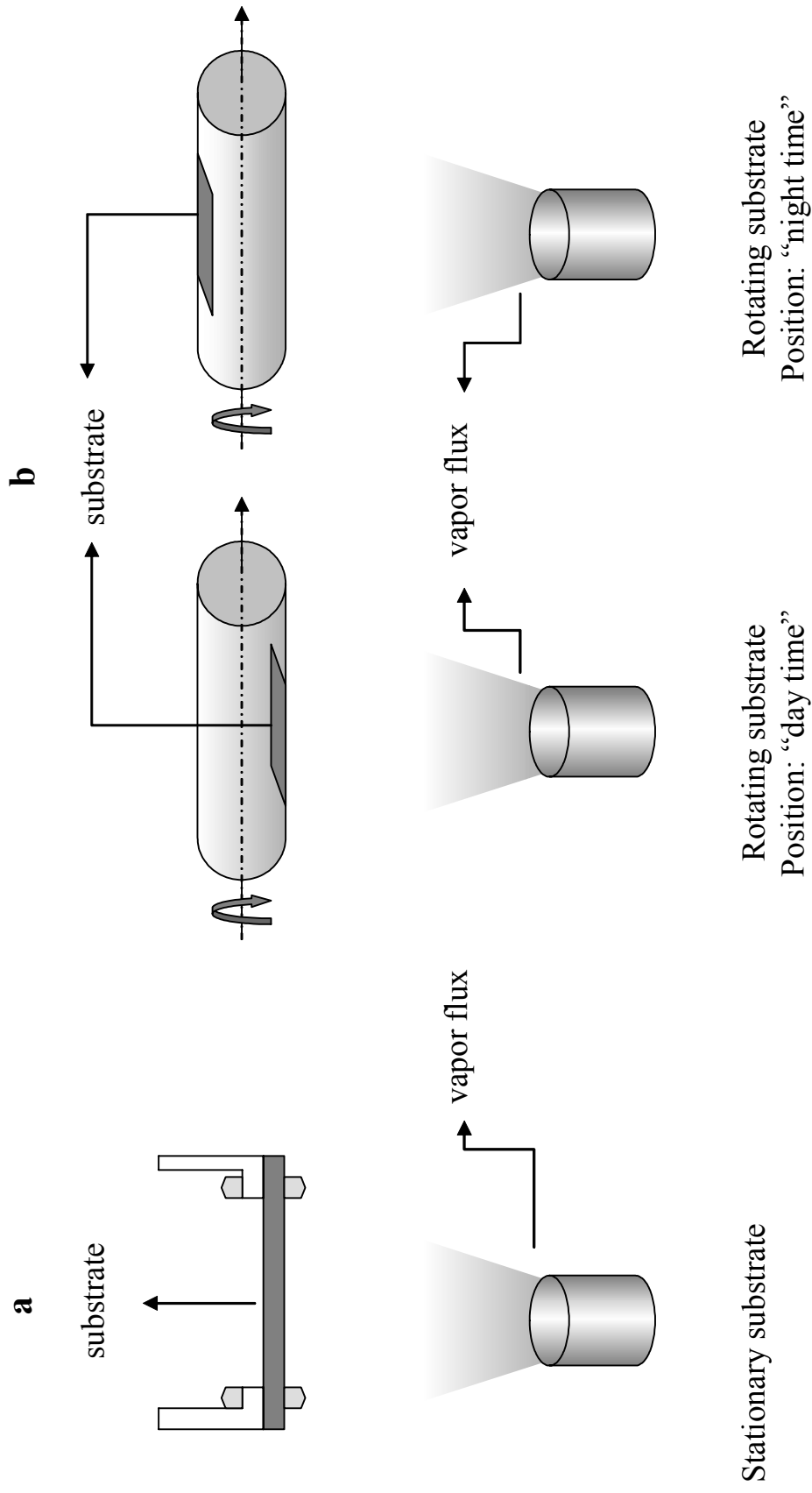


Fig. 6.4 Schematic representation of the two different arrangements of the samples investigated by EB-PVD deposition: a) stationary substrate and b) rotating substrate.

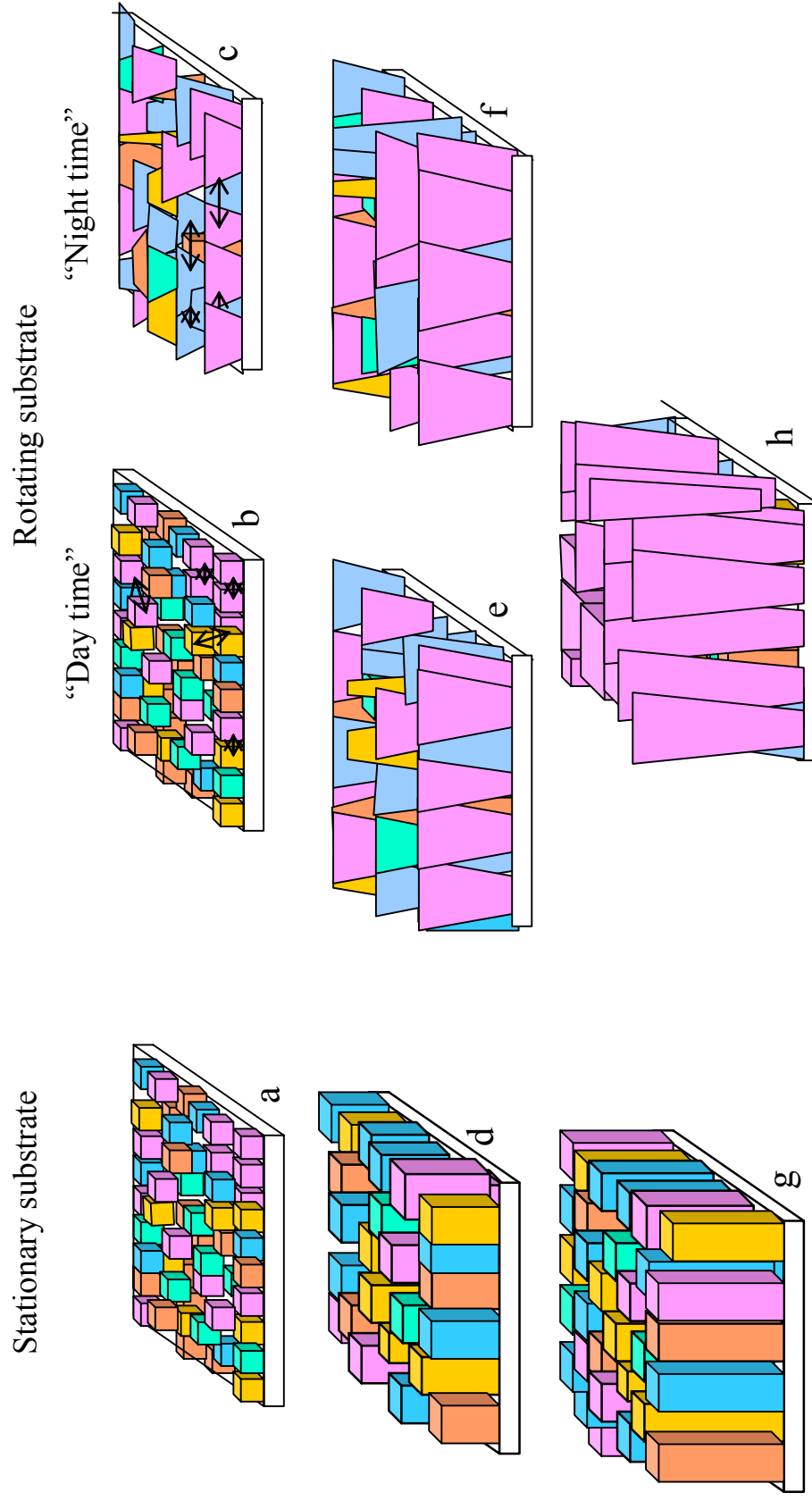


Fig. 6.5 Schematic illustration of the YSZ growth on stationary and rotating substrates, respectively. The nuclei with (100) out-of-plane orientation are represented by cubes. The different colors describe the random orientation in the plane of the substrate. a) first layer of S-YSZ_S; b) and c) first layer of S-YSZ_R during the “day” - “night time”, respectively; d) S-YSZ_S during the second revolution; e) second layer of S-YSZ_R at the “day time” and subsequent f) reorientation of the grains during the “night time”; g) S-YSZ_S growth with increasing film thickness and h) S-YSZ_R growth with increasing film thickness where the geometrical down selection becomes more prominent.

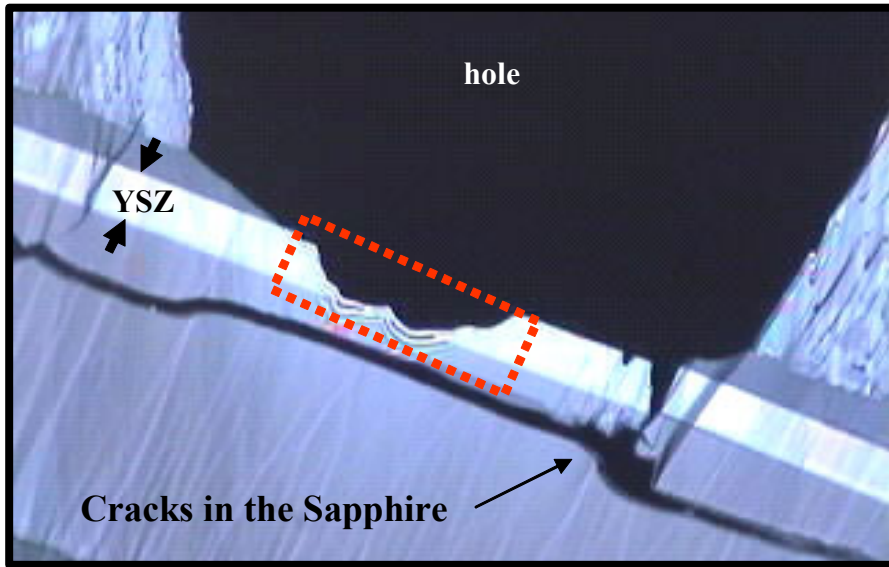


Fig. 6.6 Light Microscopy image of S-YSZ_S cross-sectional sample. The cracks in the sapphire (large arrow) drive the spallation of the thin area of the sample. The red contour with dashed line shows the interfacial region investigated by TEM.

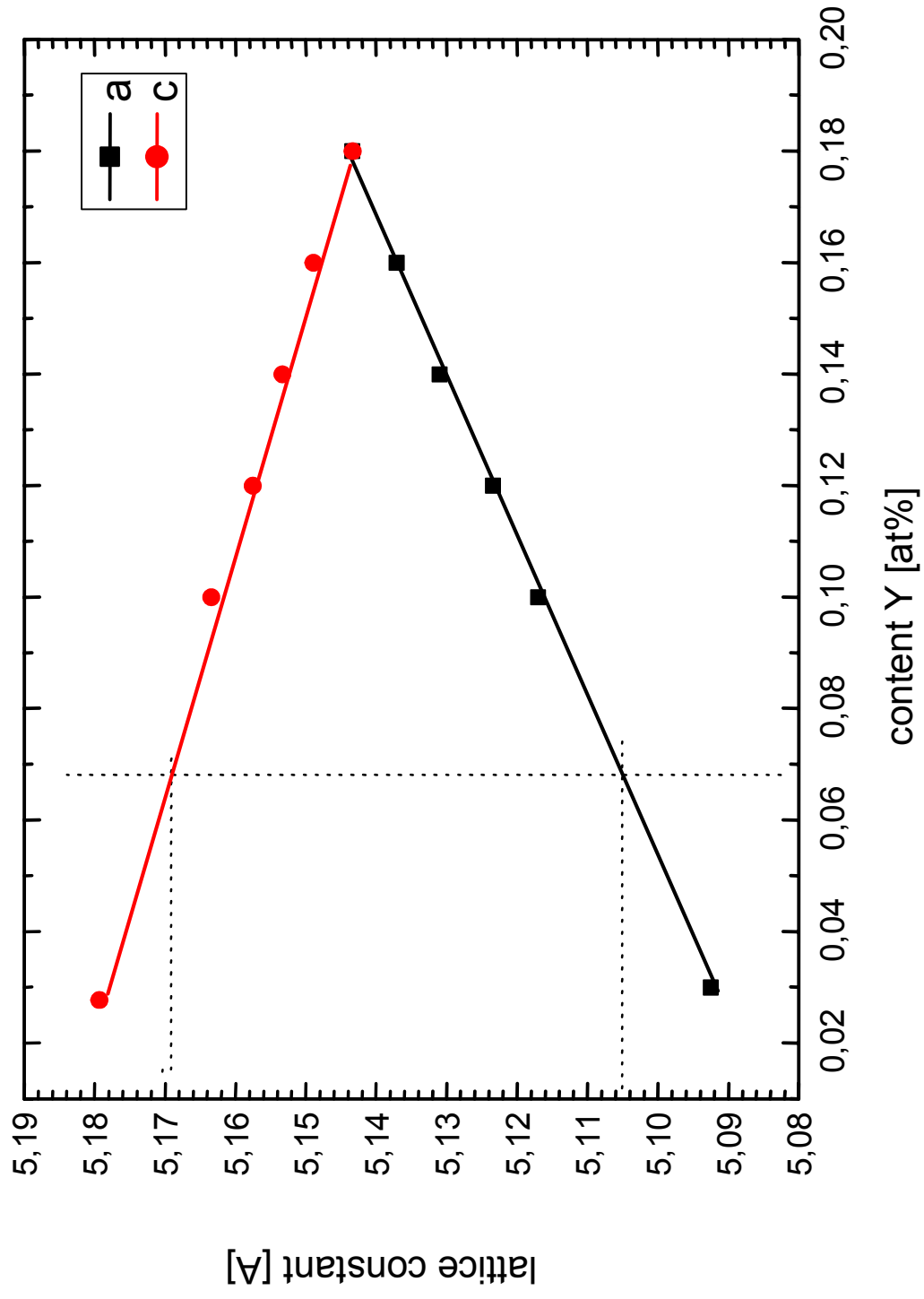


Fig. 6.7 Lattice constant of YSZ as a function of Yttrium content [94YSK]

YSZ (7%Y)

$a = 5.106 \text{ \AA}$

$c = 5.171 \text{ \AA}$

Sapphire

$a = 4.759 \text{ \AA}$

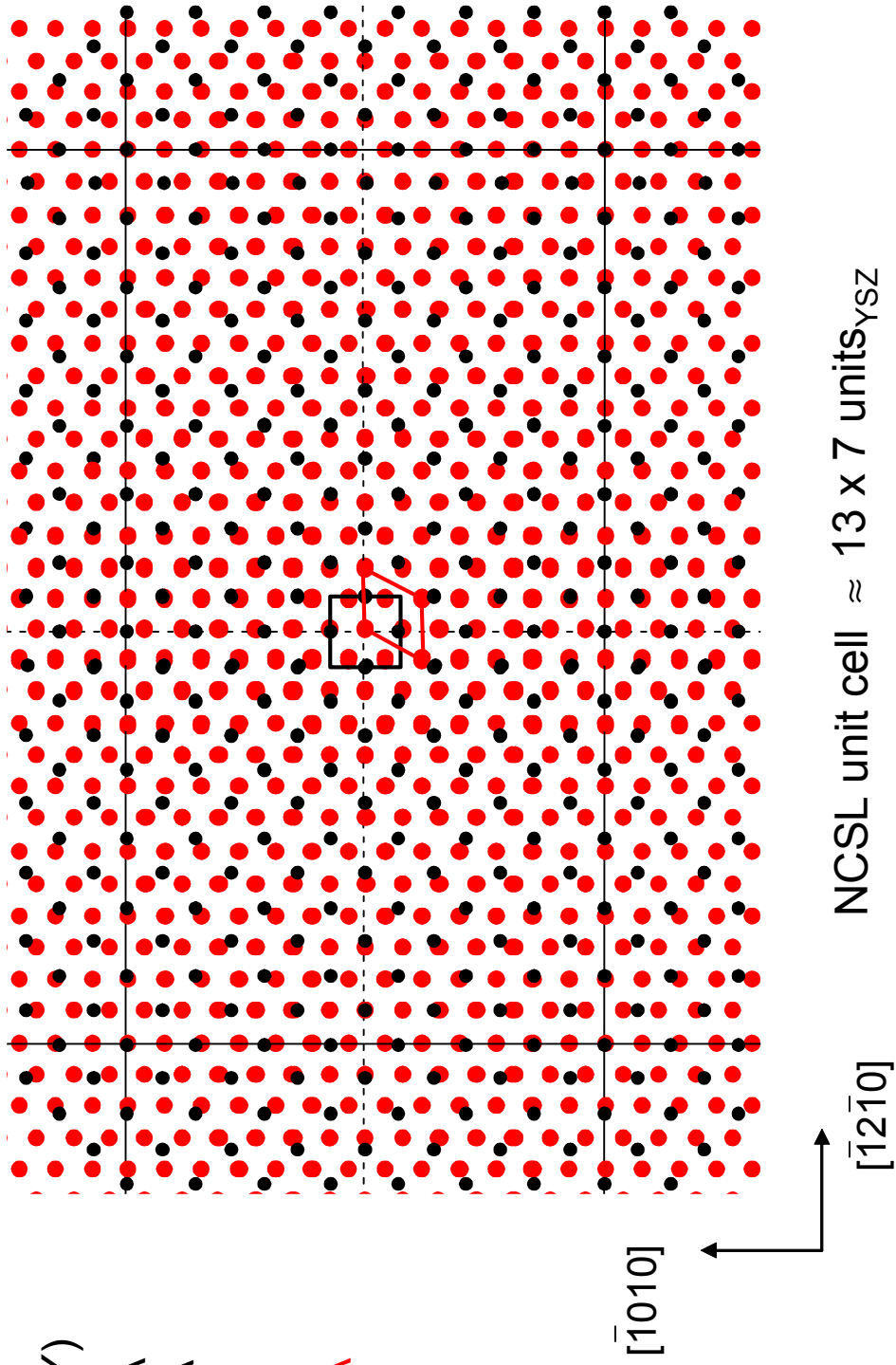


Fig. 6.8 Geometrical model of the interface between YSZ and sapphire. Alumina substrate is assumed to terminate with O ions (red circles) and the deposited films with Zr ions (black circles)

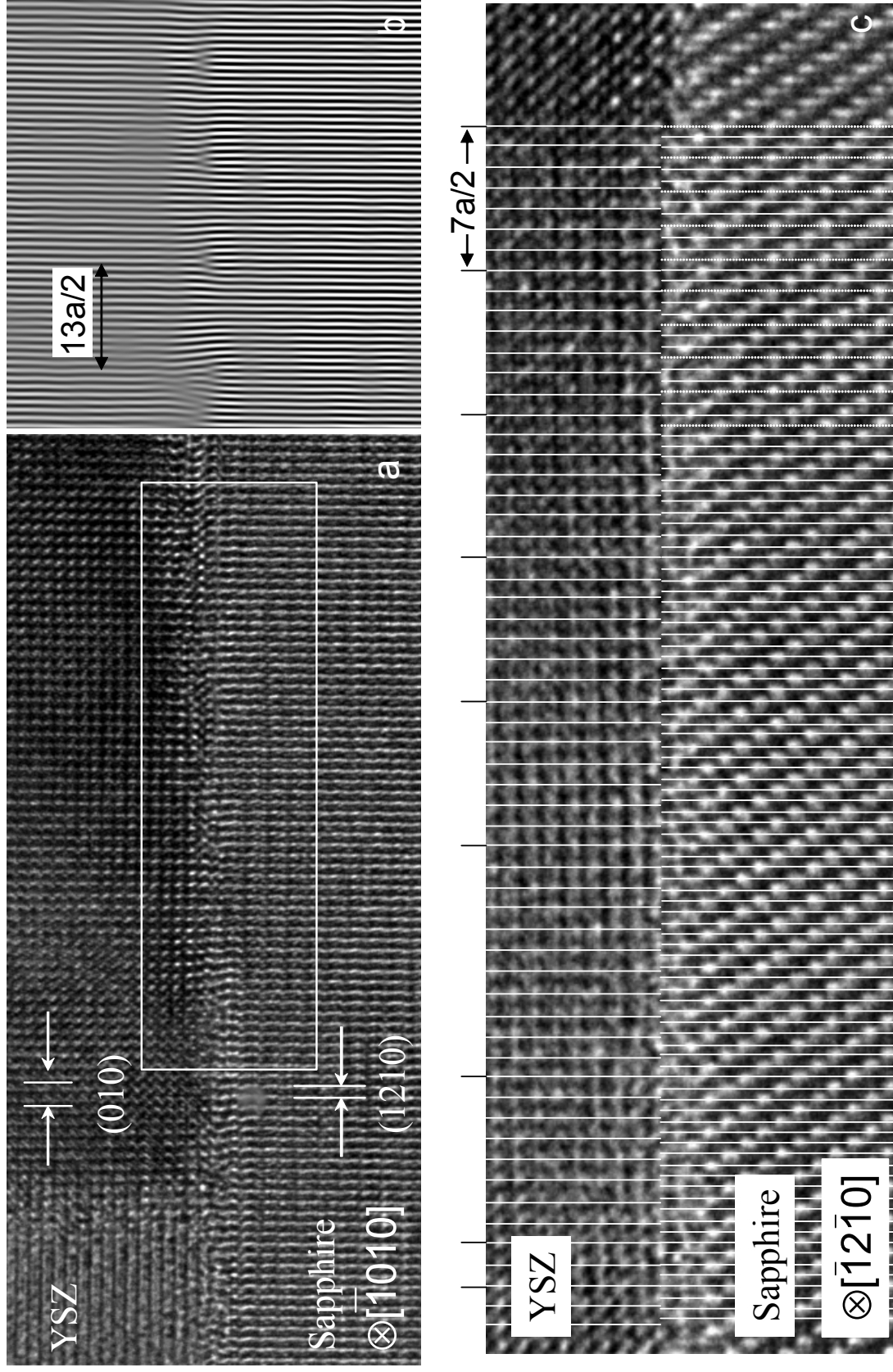


Fig. 6.9 a) HRTEM micrograph of the YSZ/Sapphire interface in $[10\bar{1}0]_{\text{sapphire}}$ zone-axis orientation; b) corresponding FFT filtered HRTEM image of the YSZ/Sapphire interface; c) HRTEM micrograph from the interface between YSZ and sapphire in $[1210]_{\text{sapphire}}$

7. Conclusions

The goal of this work was to characterize the interface microstructure between an YSZ film and an α -Al₂O₃ (sapphire) substrate, which is a model for the TGO/TBC interface in TBC systems. The work is focused on the characterization of the initial layer of YSZ and crystallographic orientation relationship between film and substrate to extend the current state of knowledge concerning the texture development. For this purpose YSZ TBCs were deposited on [0001] single crystal sapphire under stationary and rotating conditions. This model system was used for a fundamental study the microstructure of the YSZ/Sapphire interface.

YSZ TBCs deposited on stationary substrates resulted in a dense columnar microstructure with strong $\langle 100 \rangle$ fiber texture whose orientation is influenced by the sapphire substrate. This is at variance with YSZ films grown under similar (stationary) conditions on polycrystalline alumina thermally grown on bond coat alloys. This work demonstrated that the fiber texture developed from grains with preferred (100) out-of-plane orientation to the sapphire.

Periodically changing the material flux by rotating the substrate yields a less dense, porous microstructure with a larger column diameter than those coatings on stationary substrates. Moreover, in addition to the $\langle 100 \rangle$ out-of-plane texture, the coating also exhibit a preferred in-plane orientation parallel and perpendicular to the rotation axis. Since the growth of columnar grains with preferred (100) out-of plane orientation can be explained with the influence of the substrate, additional in-plane orientation (and thus column tip morphology) is interpreted through the evolutionary selection mechanism which is strongly correlated to the geometrical effect of rotation. The symmetry of the pattern of vapor incidence feed equally the four faces comprising the pyramidal tips, resulting in biaxially alignment columns.

For both, rotated and stationary samples a preferred orientation relationship with $(0001)_S \parallel (100)_{YSZ}$ was found at the interface. Many grains in the interfacial region possess a specific orientation relationship with $[10 \bar{1} 0]_S \parallel [001]_{YSZ}$ and mainly three in-plane orientations. In the case of the rotated sample the formation of three variants of in-plane orientation in the near interface region could be clearly demonstrated. The other 17% of the grains have intermediate orientations between these variants. In spite of the dissimilar structure of the two materials, a strong preferred orientation relationship for $(100)_{YSZ}$ on $(0001)_S$ is found. The fact that 83% of the columns are well oriented near the interface is remarkable since the YSZ film has in the first stage of deposition only 8 seconds (corresponds to the period of one revolution) time to achieve this preferred orientation state.

The above coatings represent special cases of the mechanism of evolutionary selection, in which columns do not evolve from a spatially random array of nuclei on the substrate, but rather from an initial population with a strong out-of-plane orientation. In the absence of rotation most of the grains are equally competitive and, after a short initial period where stray grains are eliminated, most of the columns propagate with little variation in the diameter and crystallographic orientation. Upon rotation, only the orientation that allows all facets of the column tip to receive equal amount of flux may survive the evolutionary selection mechanism. Hence, a much smaller fraction of columns is selected, and their diameter increases until a steady state condition corresponding to the bi-axially textured film is developed. Because growth under rotation occurs at a slower rate, the grain structure at the interface also evolves during deposition, promoting those orientations that reduce the interfacial energy with the substrate. This results in the development of preferred interfacial variants *after the nucleation stage*, with a mechanism largely independent from the evolutionary selection process occurring at the growth front. The HRTEM investigations confirm the epitaxy at the interface of that grains which are well oriented to the substrate. The two materials do not react to form a third phase and show an atomically abrupt interface. Along the $[10\bar{1}0]_S$ direction the lattice misfit was accommodated through misfit dislocations. A clear semi coherent structure is seen with a small core size of the misfit dislocations. Along $[1\bar{1}\bar{2}0]_S$ no misfit dislocation structure could be detected. But the clearly reduced strain contrast reveals a strain free quasi-coherent structure. As deduced from the geometrical model of the interface it could be argued that the small distance of oxygen ions in this direction might reduce the total amount of relaxation to achieve an energetically favorable ion position. In total the HRETm pictures reveal for this specific interface a strong amount of coherent atom positions, which might be the reason for the high degree of alignment of the YSZ near the sapphire interface.

TBCs deposited on seeded, rotating sapphire substrates show textures much less developed with some influence of the orientation of the seeds but with no evidence of epitaxial growth of the vapor deposited material on the seeds. The results reveal that the surface roughening resulting from the incorporation of seeds has a strong effect in delaying the evolution of the texture in spite of the presence of “favorable” sites. The texture in this case evolves in the more conventional manner, with rotation playing a predominant role over surface templating effects.

References

- 51 DBO P. Duwez, F.H. Brown Jr., and F. Odel, "The Zirconia-Yttria System", *J. Electrochem. Soc.*, 98(9) (1951), pp. 356
- 57 Kro M.L. Kronberg, "Plastic Deformation of Single Crystals of Sapphire: Basal Slip and Twinning", *Acta Mat.*, 5 (1957), pp. 508
- 59 McT J.D. McCullough and K.N. Trueblood, "The Crystal Structure of Baddeleyite (Monoclinic ZrO₂)", *Acta Cryst.*, 12, (1959), pp. 507
- 62 Teu G. Teufer, "The Crystal Structure of Tetragonal ZrO₂", *Acta Cryst.*, 15, (1962), pp. 1187
- 62 SmC D.K. Smith and C.F. Cline, "Verification of Existence of Cubic Zirconia at High Temperature", *J. Amer. Ceram. Soc.*, 45 (1962), pp. 249
- 64 Sha P.T. Shaffer, "No.1 - Materials Index" in Plenum Press Handbooks of High-Temperature Materials, Plenum Press, New York, 1964
- 64 Bau E. Bauer, "Fiber Texture", *Trans. 9th National Vac. Symp.*, 35 (1964), pp. 35
- 67 Van A. Van der Drift, "Evolutionary Selection, a Principle Governing Growth Orientation in Vapor-Deposited Layers", *Philips Res. Reports* 22, (1967), pp. 267
- 69 MoD B.A. Movchan and A.V. Demchishin, "Study of the Structure and Properties of thick Vacuum Condensates of Nickel, Titanium, Tungsten, Aluminum Oxide and Zirconium Oxide", *Fiz. Metal. Metalloved.*, 28, (4) (1969), pp. 83
- 73 BBG W.W. Barker, F.P. Bailey, and W. Garrett, "A High-Temperature Neutron Diffraction Study of Pure and Scandia-Stabilized Zirconia", *J. Solid State Chem.*, 7, (1973), pp. 448
- 74 Bun R.F. Bunshah, "Structure/Property Relationships in Evaporated Thick Films and Bulk Coatings", *J. Vac. Sci. Technol.*, Vol. 11, No 4, July/Aug. (1974), pp. 633
- 74 San J.V. Sanders, "Structure of Evaporated Metal Films", in: Chemisorptions and Reacting of Metallic Films: Vol. 1, J.R. Anderson, Ed., (1971), pp. 1-38
- 74 SPC K.K. Srivastava, R.N. Patil, C.B. Chaudhary, K.V. Gokhale, and E.C. Subbarao, "Revised Phase Diagram of the System ZrO₂-Y₂O₃", *Trans. J. Br. Ceram. Soc.*, 73(2) (1974), pp. 85
- 75 Mat J.W. Matthews, "Coherent Interfaces and Misfit Dislocations", pp. 559-609 in: *Epitaxial Growth*, Ed. By J.W. Matthews, Academic Press, 1975

- 75 Sco H.G. Scott, "Phase Relationships in the Zirconia-Yttria System", *J. Mater. Sci.*, 10(9) (1975), pp. 1527
- 77 Tho J.A. Thornton, "High Rate Thick Film Growth", *Ann. Rev. Mater. Sci.* 7, (1977), pp. 239
- 79 MCF M. Morinaga, J.B. Cohen, and J. Faber, "X-ray Diffraction Study of Zr(Ca, Y)O_{2-x} I. The Average Structure", *Acta Cryst. A* 35 (1979), pp. 789
- 81 Heu A.H. Heuer, "Alloy Design in Partially Stabilized Zirconia" in Advances in Ceramic, Vol. 3: Science and Technology of Zirconia III, S. Somiya, N. Yamamoto, and H. Yanagida. Eds., Westerville, OH: Am. Ceram. Soc., 1981, pp. 98
- 81 KFK W.M. Krievan, W.L. Fraser, and S.W. Kennedy, "The Martensite Crystallography of Tetragonal Zirconia", in Advances in Ceramic, Vol. 3: Science and Technology of Zirconia III, S. Somiya, N. Yamamoto, and H. Yanagida. Eds., Westerville, OH: Am. Ceram. Soc., 1981, pp. 82
- 81 MSG R.A. Miller, J.L. Smialek, and R.G. Garlick, "Phase Stability in Plasma-Spayed, Partially Stabilized Zirconia-Yttria", in Advances in Ceramic, Vol. 3: Science and Technology of Zirconia III, S. Somiya, N. Yamamoto, and H. Yanagida. Eds., Westerville, OH: Am. Ceram. Soc., 1981, pp. 241
- 81 SDS B.C. Steele, J. Drennan, R.K. Slowinski, N. Bonanos, and E.P. Butler, "Factors Influencing the Performance of Zirconia Based Oxygen Monitors", *Science and Technology of Ceramics*, Vol. 3 Advanced in Ceramics, A.H. Heuer and L.W. Hobbs, Ed., American Ceramic Society, (1981), pp. 286
- 82 BBK R.W. Balluffi, A. Brokman, and A.H. King, "CSL/DSC Lattice Model for General Crystal-Crystal Boundaries and Their Line Defects", *Acta Metall.* 30, (1982), pp. 1453
- 83 PJD C. Pascual, J.R. Jurado, P. Duran, "Electrical Behaviour of Doped-Yttria Stabilized Zirconia Ceramic Materials", *J. Mater. Sci.*, 18, (1983), pp. 1315
- 84 Mil R. Miller, "Oxidation behavior of thermal barrier coatings", *J. Amer. Cer. Soc.*, (1984), pp. 67
- 84 RMV R. Ruh, K.S. Mazdidasni, P.G. Valentine, and H.O. Bielstein, "Phase Relationship in the System ZrO₂-Y₂O₃ at Low Y₂O₃ Content", *J. Am. Ceram. Soc.*, 67 (9) (1984), C-190-C-192
- 84 RCH M. Rühle, N. Claussen, and A.H. Heuer, "Microstructural Studies of Y₂O₃-Containing Tetragonal ZrO₂ Polycrystals (Y-TZP), in Advances in Ceramic, Vol. 12, Science and Technology of Zirconia II, S. Somiya, N. Yamamoto, and H. Yanagida. Eds., Westerville, OH: Am. Ceram. Soc., (1984), pp. 352
- 84 StE R. Stevens and P.A. Evans, "Transformation Toughening by Dispersed Polycrystalline Zirconia" *Br. Ceram. Trans. J.*, Vol. 83, (1984), pp. 28

- 85 LeL W.E. Lee and K.P. Lagerlof, "Structural and Electron Diffraction Data for Sapphire (α -Al₂O₃)", *Journal of Electron Microscopy Technique* [2] (1985), pp. 247
- 85 Ste S. Stecura, "Optimization of the NiCrAlY/ZrO₂-Y₂O₃ Thermal Barrier System", NASA Tech. Memo. (1985), pp. 86905
- 85 Str T.E. Strangman, "Thermal Barrier Coating for Turbine Airfoils", *Thin Solid Films*, 127, (1985), pp. 93
- 86 Bev M.B. Bever, Editor-in-Chief: "Encyclopedia of Materials Science and Engineering", Vol. 7, T-Z, (1986), Pergamon Press & The Mit Press
- 86 MMP L. Mazerolles, D. Michel, and R. Portier, "Interfaces in Oriented Al₂O₃-ZrO₂ (Y₂O₃) Eutectics", *J. Am. Cer. Soc.* 69(3), (1966), pp. 252
- 86 Sch H. Schubert, "Anisotropic Thermal Expansion Coefficient of Y₂O₃-Stabilized Tetragonal Zirconia", *J. Am. Ceram. Soc.*, 69 [3] (1986), pp. 270
- 86 SNR A. Strecker, G. Necker, M. Rühle, „Concave Grinding Units (Dimplers) for Preparing Transmission Electron Microscope Specimens“, *Pract. Metallogr.* 23 (1986), pp. 417-429, Carl Hanser Verlag, München
- 86 SrS D.J. Srolovitz and S.A. Safran, "Capillary Instabilities in Thin Films. I. Energetics", *J. Appl. Phys.*, 60 (1) (1986), pp. 247
- 87 Sta P. Stadelmann, EMS: "A Software Package for Electron Diffraction analysis and HRTEM Image Simulation in Materials Science", *Ultramic.*, 21, (1987), pp. 131
- 88 HCL A.H. Heuer, R. Chaim and V. Lantery, "Review: Phase Transformations and Microstructural Characterization of alloys in the System ZrO₂-Y₂O₃", in: Advances in Ceramic, Vol. 24: Science and Technology of Zirconia III, S. Somiya, N. Yamamoto, and H. Yanagida. Eds., Westerville, OH: Am. Ceram. Soc., (1988), pp. 3
- 88 HHR C.J. Howard, R.J. Hill, and B.E. Reichert, "Structures of the ZrO₂ Polymorphs at Room Temperature by High-Resolution Neutron Powder Diffraction", *Acta. Cryst.* B44, (1988), pp. 116
- 88 Stu V.S. Stubican, "Phase Equilibria and Metastabilites in the Systems ZrO₂-MgO, ZrO₂-CaO, and ZrO₂-Y₂O₃", in: Advances in Ceramic, Vol. 24: Science and Technology of Zirconia III, S. Somiya, N. Yamamoto, and H. Yanagida. Eds., Westerville, OH: Am. Ceram. Soc., (1988), pp. 71
- 89 AgR D.C. Agrawal and R. Raj, "Autonucleation of Cavities in Thin Ceramic Films", *Acta Metall.*, Vol. 37, No 7, (1989), pp. 2035
- 89 LAD L. Lelait, S. Alperine, C. Diot, and M. Mévrel, "Thermal Barrier Coatings: Microstructure Investigation after Annealing", *Materials Science and Engineering*, A121 (1989), pp. 475

- 89 Mev R. Mévrel, "State of the Art on High-temperature Corrosion-resistant Coatings", *Materials Science and Engineering*, A120 (1989), pp. 13
- 90 MLM K.T. Miller, F.F. Lange and D.B. Marshall, "The Instability of Polycrystalline Thin Films: Experiment and Theory", *J. Mater. Res.*, Vol. 5, No. 1, (1990), pp. 151
- 90 TFS C.V. Thompson, J. Floro, and H.I. Smith, "Epitaxial Grain Growth in Thin Metal Films", *J. Appl. Phys.* 67(9), 1 May, (1990), pp. 151
- 90 Tho C.V. Thompson, "Grain Growth in Thin Films", *Annu. Rev. Mater. Sci.*, 20, (1990), pp. 245
- 91 DJH Y. Du, Z. Jin and P. Huang, "Thermodynamic Assessment of the $ZrO_2 - YO_{1.5}$ System", *J. Amer. Soc.*, 74 (7), (1991), pp. 1569
- 91 MLa K.T. Miller and F.F. Lange, "Highly Oriented Thin Films of Cubic Zirconia on Sapphire through Grain Growth Seeding", *J. Mater. Res.*, Vol. 6, (11), (1991), pp. 2387
- 93 LAD L. Lelait, S. Alperine, and C. Diot, "Microstructural Investigations of EB-PVD Thermal Barrier Coatings", *Journal de Physique IV*, Colloque C9, (1993), pp. 645
- 93 Lan F.F. Lange, "Epitaxial Grain Growth in Thin Films", *Materials Science Forum* Vol. 113-115 (1993), pp. 81
- 93 MBF U. Martin, H. Boysen and F. Frey, "Neutron Powder Investigation of Tetragonal and Cubic Stabilized Zirconia, TZP and CSZ, at Temperatures up to 1400 K", *Acta Cryst.*, B49, (1993), pp. 403
- 93 MCC K.T. Miller, C.J. Chan, M.G. Cain, and F.F. Lange, "Epitaxial Zirconia Thin Films from Aqueous Precursors", *J. Mater. Res.*, Vol. 8, No.1, 1993
- 93 SSM A. Strecker, U. Salzberger, J. Mayer, "Specimen Preparation of Transmission Electron Microscopy: Reliable Method for Cross-Sections and Brittle Materials", *Pract. Metallogr.*, 30 (1993), pp. 482, Carl Hanser Verlag, München
- 94 CaL M.G. Cain and F.F. Lange, "Heteroepitaxy of Cubic Zirconia on Basal and Prismatic Planes of Sapphire", *J. Mater. Res.*, Vol. 9, No. 3, Mar 1994
- 94 LeS E.Y. Lee and R.D. Sisson Jr., "The Effect of Bond Coat Oxidation on the Failure of Thermal Barrier Coatings", *Proceedings of the 7th National Thermal Spray Conference* 20-24 June 1994, Boston, Massachusetts
- 94 SBS Y.H. Sohn, R.R. Biederman and R.D. Sisson Jr., "Microstructural Development in Physical Vapor-Deposited Partially Stabilized Zirconia Thermal Barrier Coatings", *Thin Solid Films*, 250 (1994), pp.1

- 94 UMH O. Unal, T.E. Mitchell, and A.H. Heuer, "Microstructures of Y₂O₃-Stabilized ZrO₂ Electron Beam-Physical Vapor Deposition Coatings on Ni-Base Superalloys", *J. Am. Ceram. Soc.*, 77 [4] (1994), pp. 984
- 94 YSK M. Yashima, S. Sasaki and M. Kakihana, "Oxygen-Induced Structural Change of the Tetragonal Phase around the Tetragonal-Cubic Phase Boundary in Zirconia-Yttria Solid Solution", *Acta Cryst.*, B50, (1994), pp. 663
- 95 SFP U. Schulz, K. Fritscher, M. Peters, "EB-PVD Y₂O₃-and CeO₂/Y₂O₃-Stabilized Zirconia Thermal Barrier Coatings-Crystal Habit and Phase Composition", *Surface and Coatings Technology* 82 (1996), pp. 259
- 95 YMT M. Yashina, T. Mitsuhashi, H. Takashina, M. Kakihana and M. Yoshimura, "Tetragonal-Monoclinic Phase Transition Enthalpy and Temperature of ZrO₂-CeO₂ Solid Solutions", *J. Am. Ceram. Soc.* 78 (1995), pp. 22
- 96 CaH R.W. Cahn and P. Haasen, Eds. in "*Physical Metallurgy*"; fourth, revised and enhanced edition, Chapter II, "Transmission Electron Microscopy", M. Rühle and M. Wilkens, Elsevier Science BV, 1996
- 96 CHP H.C. Chen, J. Heberlein, E. Pfender, "TEM Characterization of Plasma – Spayed Thermal Barrier Coatings and Ceramic-Metal Interfaces after Hot Isostatic Pressing", *Thin Solid Films* 301 (1997), pp. 105
- 96 DBP R.B. Dinwiddie, S.C. Beecher, W.D. Porter, and B.A. Nagaraj, "The Effect of Thermal Aging on the Thermal Barrier Conductivity of Plasma Sprayed and EB-PVD Thermal Barrier Coatings", *ASME Report 96-GT-282* (1996)
- 96 Jon R.L. Jones, "Thermal Barrier Coating", *Metallurgical and Ceramic Protective Coatings*, pp. 194, Edited by K. Stern. Published by Chapman & Hall, London, 1996, ISBN 0 412 54440 7
- 96 LSB W.Y. Lee, D.P. Stinton, Ch.C. Berndt, F. Erdogan, Y.D. Lee and Z. Mutasim, "Concept of Functionally Graded Materials for Advanced Thermal Barrier Coating Applications", *J. Am. Ceram. Soc.*, 79 [12] (1996), pp. 3003
- 96 MBM J. Malek, L. Benes, T. Mitsuhashi, "Powder Diffraction Data and Rietveld Refinement of Metastable t-ZrO₂ at Low Temperature", *Powder Diffraction*, 12 (2), June (1997), pp. 96
- 96 MRS P.C. McLntyre, K.G. Ressler, N. Sonnenberg, and M.J. Cima, "Transmission Electron Microscopy Investigation of Biaxial Alignment Development in YSZ Films", *J. Vac. Sci. Technol.*, A 14(1), Jan/Feb (1996), pp. 210
- 96 RSC K.G. Ressler, N. Sonnenberg, and M.J. Cima, "The Development of Biaxial Alignment in Yttria-Stabilized Zirconia Films Fabricated by Ion Beam Assisted Deposition", *J. Elect. Mater.*, Vol. 25, No. 1, (1996), pp. 35
- 96 RuR L. Ruiz and M.J. Readey, "Effect of Heat Treatment on Grain Size, Phase Assemblage, and Mechanical Properties of 3 mol% Y-TZP", *J. Am. Ceram. Soc.*, 79 [9] (1996), pp. 2331

- 96 SFP U. Schulz, K. Fritscher, and M. Peters, „EB-PVD Y_2O_3 -and CeO_2/Y_2O_3 -Stabilized Zirconia Thermal Barrier Coatings-Crystal Habit and Phase Composition”, *Surface and Coatings Technology*, 82 (1996), pp. 259
- 96 SOB U. Schulz, H. Oettel, and W. Bunk, “Texture of EB-PVD Thermal Barrier Coatings under Variable Deposition Conditions”, *Z. Metallkd.*, 87 6 (1996), pp. 488
- 96YKY M. Yashima, M. Kakihana, M. Yoshimura, “Metastable-Stable Phase Diagrams in the Zirconia-Containing Systems Utilized in Solid-Oxide Fuel Cell Application”, *Solid State Ionics*, 86-88 (2), (1996) pp. 1131
- 96 WiC D.B. Williams and C. B. Carter, “*Transmission Electron Microscopy*”, Vol. 1-4, Plenum Press, New York (1996)
- 97 FSL K. Fritscher, M. Schmücker, C. Leyens and U. Schulz, “TEM Investigation on the Adhesion of YPSZ EB-PVD TBCs“, *Materials Science Forum*, Vol. 251-254 (1997), pp. 965
- 97 MRY Y.J. Mao, C.X. Ren, J. Yuan, F. Zhang, X.H. Liu, and S.C. Zou, “Study on the Growth of Biaxially Aligned Yttria-Stabilized Zirconia Films During Ion Beam Assisted Deposition”, *J. Vac. Sci. Technol.*, A. 15(5), Sep/Oct. (1997), pp. 2687
- 97 PWL B.A. Pint, I.G. Wright, W.Y. Lee, Y. Zhang, K. Prübner, K. B. Alexander, “Substrate and Bond Coat Compositions: Factors Affecting Alumina Scale Adhesion”, *Material Science and Engineering*, A 245, No 2, (1998), pp. 201
- 97 SFR U. Schulz, K. Fritscher, H.-J. Rätzer-Scheibe, W.A. Kaysser, and M. Peters, „Thermocyclic Behaviour of Microstructurally Modified EB-PVD Thermal Barrier Coating”, *Materials Science Forum*, Vol. 251-254, (1997), pp. 957
- 97 TKZ Y.A. Tamarin, E.B. Kachanov, and S.V. Zherzdev, ”Thermophysical Properties of Ceramic Layers in TBC-EB”, *Materials Science Forum*, Vol. 251-254, (1997), pp. 949
- 98 HHK C.J. Howard, B.A. Hunter, and D-J. Kim, “Oxygen Position and Bond Lengths from Lattice Parameters in Tetragonal Zirconias”, *J. Am. Ceram. Soc.*, 81 [1] (1998), pp. 241
- 98 JRB C.A. Johnson, J.A. Ruud, R. Bruce, and D. Wortman, “Relationships between Residual Stress, Microstructure, and Mechanical Properties of Electron Beam-Physical Vapor Deposition Thermal Barrier Coatings”, *Surface Coating and Technology*, 108-109, (1998), pp. 80
- 98 KIG P.G. Klemens, and M. Gell, “Thermal Conductivity of Thermal Barrier Coating”, *Materials Science and Engineering*, A 245, (1998), pp. 143
- 98 Lev C.G. Levi, “Metastability and Microstructure Evolution in the Synthesis of Inorganics from Precursors”, *Acta Mater.*, Vol. 46, No 3, 1998, pp. 787

- 98 MGT C. Mary, R. Guinebretiere, G. Trolliard, B. Soulstin, P.Villechaize, and A. Dager, "Epitaxial Zirconia Films on Sapphire Substrates", *Thin Solid Films* 336 (1998), pp. 156
- 99 BML W. Beele, G. Marijnissen, A. van Lieshout, „The Evolution of Thermal Barrier Coatings-Status and Upcoming Solutions for Today’s Key Issues”, *Surface and Coatings Technology*, 120-121 (1999), pp. 61
- 99 SYT M.J. Stiger, N.M. Yanar, M.G. Topping, F.S. Pettit, and G.H. Meier, "Thermal Barrier Coatings for the 21st Century", *Zeitschrift für Metallkunde*, 90(12), Dec.(1999), pp. 1069
- 99 TLL S.G. Terry, J. R. Litty, and C. G. Levi, "Evolution of Porosity and Texture in Thermal Barrier Coatings Grown by EB-PVD" In: *Elevated Temperature Coatings: Science and Technology III*, 13-25, The Minerals, Metals and Materials Society, 1999; Ed. by J.M. Hampikian and N.B. Dahorte
- 00 ScS U. Schulz, and M. Schmücker, "Microstructure of ZrO₂ Thermal Barrier Coating Applied by EB-PVD", *Materials Science and Engineering*, A 276 (2000), pp. 1
- 00 SFL U. Schulz, K. Fritscher, C. Leyens, "Two-Source Jumping Beam Evaporation for Advanced EB-PVD TBC Systems", *Surface and Coatings Technology*, 133-134 (2000), pp. 40
- 01 EMH A.G. Evans, D.R. Mumm, J.W. Hutchinson, G.H. Meier, and F.S. Pettit, "Mechanisms controlling the durability of Thermal Barrier Coatings", *Progress in Material Science*, 46 (2001), pp. 505
- 01 FuH B. Fultz and J.M. Howe, "Transmission Electron Microscopy", 4. Edition Springer, Berlin-Heidelberg-New York-Tokyo (2001)
- 01 HLC P. Heydt, C. Luo, and D. Clarke, "Crystallographic Texture and Thermal Conductivity of Zirconia Thermal Barrier Coatings Deposited on Different Substrates", *J. Am. Ceram. Soc.*, 84 [7] (2001), pp. 1539
- 01 PLS M. Peters, C. Leyens, U. Schulz, and W.A. Kaysser, "EB-PVD Thermal Barrier Coatings for Aero Engines and Gas Turbines," *Advanced Engineering Materials*, 3 (No.4), (2001), pp. 193
- 01 SLC P. Scardi, M. Leoni, F. Cernuschi, and A. Figari, "Microstructure and Heat Transfer Phenomena in Ceramic Thermal Barrier Coatings", *J. Am. Ceram. Soc.*, 84 [4] (2001), pp. 827
- 01 Ter S.G. Terry, "Evolution of Microstructure during the Growth of Thermal Barrier Coatings by Electron-Beam Physical Vapor Deposition", *Ph.D. Dissertation*, Materials Department, University of California, Santa Barbara, USA (2001)

- 01 ToC V.K. Tolpygo and D.R. Clarke, "Damage Induced by Thermal Cycling of Thermal Barrier Coatings", in: Elevated Temperature Coatings: Science and Technology IV, Ed. J.M. Hampikian et al., Warrendale, OH: TMS, 2001, pp. 93
- 02 NLJ J.R. Nicholls, K.J. Lawson, A. Johnstone, and D.S. Rickerby, "Methods to Reduce the Thermal Conductivity of EB-PVD TBCs", *Surface and Coating Technology*, 151-152 (2002), pp. 383
- 02 SRW J.H. Schneibel, C.J. Rawn, T.R. Watkins, and E.A. Payzant, "Thermal Expansion Anisotropy of Ternary Molybdenum Silicides Based on Mo_5Si_3 ", *Physical Review B*, Vol. 65 (2002), pp. 134112
- 03 FaA O. Fabrichnaya, and F. Aldinger, "Assessment of Thermodynamic Parameters in the System $\text{ZrO}_2\text{-Y}_2\text{O}_3\text{-Al}_2\text{O}_3$ ", *to be published*

Acknowledgements

The work on the thesis was carried out at the Max-Planck-Institut für Metallforschung Stuttgart, Germany, between December 1999 and September 2003. Particular financial support from the EC/NSF Project HIPERCOAT (GRD2-200-30 211) funded for the EC partners under the "Competitive and Sustainable Growth" Program (1998-2002) is gratefully acknowledged

I am especially grateful to my thesis advisor Prof. M. Rühle who gave me the opportunity to do the study in his group, for his constant support, stringent objectivity and interest in the different stages of realizing the project. I gained a model for a high standard of professionalism, integrity and sincerity that I hope to live up to.

I would like to thank Prof. F. Aldinger for agreeing to take over the *Mitbericht*.

My special thanks to Prof. C. Levi for the scientific discussions, for carefully reading the manuscript, for his insight and criticism.

I gratefully acknowledge St. Krämer for his invaluable help, patience and support during the past two years.

Many thanks to C. Scheu, W. Sigle, G. Richter and St. Fabris for the exchange of ideas, as well as to G. Richter for performing the HRTEM work.

S. Kühnemann is acknowledged for the excellent SEM images, as is J. Cho (UCSB) for his SEM, X-Ray analysis, and particularly for processing the sample (growing the coating) at UCSB. I thank a lot P. Kopold for introducing me to the TEM, as well as C. Hahn and J. Thomas for their help during the TEM and STEM work

My thanks also go to the TEM specimen preparation team, U. Salzberger, A. Strecker, M. Sycha, for their support and help without which no TEM images could be performed. Special thanks to U. Salzberger who worked hard on the stationary sample and did not give up.

U. Täfner is acknowledged for the metallographic sample preparation and for her contribution to the AFM work.

I would like to thank also C. Sussdorff, E. Pfeilmeier, and U. Salzberger for helping me to decode Rühle's write on the corrections.

I gratefully appreciate all members and international colleagues of Prof. M. Rühle's group for their help and for the excellent work conditions. The PhD students from my early years at MPI, my officemate Diana and Eric have since graduated but are still remembered for their help during the time I had no advisor and for the professional and personal discussions I had with them.

I was also very fortunate to meet and make friends with a number of researchers visiting MPI who encouraged and supported me in the hardest of times. I am thankful to all my friends who indirectly contributed to this work through their belief in me and who did not stop telling me “You will do it!”

My family has my deepest gratitude for all their encouragement. My parents, my brother, his family, and my aunt have been always supportive.

This thesis is dedicated to my parents. Without their encouragement, patience and love I might not be able to see the result of this long research effort.

Curriculum vitae

Name	Boryana Rashkova
Date of birth	October 8 th , 1970
Place of birth	Sofia, Bulgaria
Nationality	Bulgarian
Marital Status	Single
1976-1984	Grundschule, Sofia
1984-1988	Nationales Gymnasium für Naturwissenschaft
July 1988	Abitur
1989-1994	Technical University Sofia, Bulgaria
July 1994	Diploma Engineering Diploma Thesis: “Electrochemical Behaviors of Lead-Cobalt Anodes for Electroextraction of Zinc from Sulphate Electrolytes”
Since December 1998	PhD student at Max-Planck-Institut für Metallforschung Stuttgart, in the group of Prof. Dr. Dr. h.c. M. Rühle